Fluorescence microscopy for interference lithography: Set-up design and pattern characterization by fluorescence modulation

Von der Fakultät für Lebenswissenschaften

der Technischen Universität Carolo-Wilhelmina zu Braunschweig

zur Erlangung des Grades einer

Doktorin der Naturwissenschaften

(Dr. rer. nat.)

genehmigte

Dissertation

von Laura Shirin Jess geb. van den Heuvel
aus Heerhugowaard, Niederlande

1. Referent: Prof. Dr. Peter Jomo Walla
2. Referent: Privatdozent Dr. Christof Maul
eingereicht am: 30.01.2017
mündliche Prüfung (Disputation) am: 15.03.2017

Druckjahr 2017

Vorveröffentlichungen der Dissertation

Teilergebnisse aus dieser Arbeit wurden mit Genehmigung der Fakultät für Lebenswissenschaften, vertreten durch den Mentor der Arbeit, in folgenden Beiträgen vorab veröffentlicht:

Tagungsbeiträge

Jess, L. S., Pfennig, D., Grunwald, M., Albrecht, A., Hafi, N., Walla, P. J.: Obtaining resolution enhanced fluorescence images and 3D orientation information of single molecules by polarization modulation. Vortrag PHYS-490, Single-molecule Fluorescence Imaging (#208). International Chemical Congress of Pacific Basin Societies (Pacifichem 2015), Honolulu, Hawaii, USA (2015).

Posterbeiträge

Jess, L. S., Pfennig, D., Grunwald, M., Albrecht, A., Hafi, N., Walla, P. J.: Obtaining resolution enhanced fluorescence images and 3D orientation information of single molecules by polarization modulation. Poster 195, Single-molecule Fluorescence Imaging (#208). International Chemical Congress of Pacific Basin Societies (Pacifichem 2015), Honolulu, Hawaii, USA (2015).

Contents

1 Introduction

From a historical perspective, optical technologies can be traced back to the ancient world well before Christ. Among the first everyday items for use, the occurrence of very simple mirrors and lenses was described.[1] For thousands of years to come, many philosophers pondered about the nature of light, about the nature of optical phenomena like refraction and dispersion, and about ways to improve mirror and lens properties. In the seventeenth century, events and new optical findings started to pick up pace, leading to the first working telescopes and microscopes whose invention and development is nowadays credited to two Dutch eyeglass makers, Hans Lippershey (1587-1619) and Zacharias Janssen (1588-1632). At the same time, Johannes Kepler (1571-1630), Willebrord Snellius (1591-1626), and René Descartes (1596-1650) contributed fundamental findings in the mathematical description of reflection (Descartes) and refraction (Kepler, Willebrord) which can be considered a milestone in applied optics.[1] In this age also, first observations and assumptions were put in words concerning the phenomena of diffraction (Francesco Grimaldi (1618-1663)), interference (Robert Hooke (1635-1703)), the polarized nature of light (Christiaan Huygens (1629-1695)), and dispersion (Isaac Newton (1642-1727)). Thereafter, many scientists have devoted their research to optics which led to a continuous improvement of technologies and their applicability to address questions from many other fields of research. The invention of Lasers in the 1960s can be regarded as a second milestone in applied optics.[2] By means of this coherent light source further optical phenomena were unraveled and understood (e. g. frequency mixing) which led to a technical break-through in many optics related fields of research e. g. holography, military, and communication. Storage, transmission, and visualization of information by means of electric signals is on the verge of being overtaken by optical signals, a process which has already revolutionized and will continue to influence our every day life.

Many of the just mentioned basic terms of optics are reflected in the course of this thesis which was devoted to a study within the field of fluorescence microscopy. One goal of this thesis was the investigation of to what extent a wide-field epi fluorescence microscope is suitable for interference lithography i. e. recording an interference pattern into a photoresist. For example, by means of interference lithography it is possible to shape the photo-thermal or photo-chemical surface of a material with a regular, periodic pattern created by the interference of high-power laser beams (DLIP: direct laser interference patterning).[3][4][5] Periodic patterns in two- and three-dimensions from multi-beam interference are well understood, highly uniform, and cover spatially large areas which makes them suitable for creating surface patterns on fast time scales. The dimension of the periodic pattern depends on the wavelength of light used for interference, so that electron interference lithography has been reported to succeed in the fabrication of nanostructures.[6][7]

In the course of this thesis, a self-built fluorescence microscopy set-up was modified in order to investigate the simplest form of an interference pattern. Herein, two consecutive Wollaston prisms each installed in rotation mounts were inserted into the excitation light's beam path thus resulting in four separated beams. Two of the beams were reflected into the microscope's objective which interfered in the front focal plane to form a periodic illumination structure which was called fringe pattern. This fringe pattern consisted of evenly spaced lines with a certain periodicity p and a certain orientation β. One focus of this thesis resides with the thorough characterization of the fringe pattern parameters p and β with respect to the initial beam position at the back focal plane of the objective which in turn depends on the orientation of the Wollaston prisms used, as outlined in Chapter 3. Herein, a brief explanation of the theoretical background of two beam interference and beam separation by Wollaston prisms is given, along with a detailed description of the experimental set-up and measurement's procedure. The results section is arranged in a consecutive manner. Since the parameters beam position (X/Y), intensity (I), and polarization angle (θ) depend on the orientation of the Wollaston prism i. e. the angle of the rotation mount (ω) in which the Wollaston prism was installed, the investigation was divided into three steps. Exploring the named parameters were first conducted after single Wollaston prisms followed by an investigation for both stacked prisms in order to obtain an understanding of the beam separation by the Wollaston prisms. Then, the resulting fringe patterns were recorded with the fluorescence microscope for varying settings of the Wollaston prisms in order to gain insight into the relationship between the fringe pattern periodicity and the interfering beam's positions. Each stage was accommodated by deriving mathematical equations for describing the findings which were used in the final stage of that chapter to specifically predict fringe patterns.

The knowledge gained from being able to predict fringe patterns in the fluorescence microscope was then used to design a specific periodic line pattern with a periodicity of 1 µm which was used for fluorescence lithography. A densely packed layer of fluorescent dyes (ATTO 590) on glass substrate was used as a self-built photoresist in the focal plane of the objective. By using very high illumination intensities of the interfering laser beams, fluorophores experiencing intensities above a certain threshold limit are irreversibly photodestructed. Since the interference pattern also contains nodes i. e. areas of no intensity, fluorescent dyes within or very close to the nodes were expected to remain intact and would serve as the negative image after bleaching the fringe pattern into the photoresist.

One major goal of this thesis was the characterization of the resulting negative image with special emphasis on the final line width of the nodes. Since the nodes of the negative image contained fluorescent dyes, the evaluation of the line width became accessible by fluorescence microscopy imaging using fluorescence modulation.[8][9] By exploiting the photo-selective nature of excitation properties of individual dyes, it is possible to record modulated fluorescence data from immobilized samples, as described in Chapter 2. After briefly introducing fundamental principles of the absorption and emission of light, a technique is introduced by which the photo-selective nature of excitation is confined to a narrower range of angles (excitation polarization angle narrowing, ExPAN).[8][10] In the results section, the effect of ExPAN in comparison to regular fluorescence modulation was investigated on individual fluorescence emitters. The concept of fluorescence modulation was qualitatively illustrated using consecutive images from the recorded imaging video and quantified by showing time-dependent fluorescent intensity traces.

By means of fluorescence modulation alternating between excitation with and without ExPAN, the negative image of the bleached fringe pattern was characterized, as described in Chapter 4. The fluorescence data was investigated using an alternating-variable search method (AVM)[11] which was designed to localize a number of individual emitters within the lines containing fluorescent dyes. The goal of this investigation was to express the dimension of the line width in terms of a full-width at half-maximum (FWHM) value of the single molecule localization distribution. This investigation was set up in a consecutive manner. First, a non-modulated fitting version of AVM was conducted on fluorescence data sets at low dye densities in which the effect of fluorescence modulation was removed by averaging. This allowed introducing and explaining the concept of AVM in the single molecule regime by non-modulated fitting. Then, the AVM algorithm was extended to the use of modulated fluorescence data with and without ExPAN. This was first applied to the same data set (single molecule density) as for the non-modulated fitting procedure but without averaging the data prior to evaluation in order to establish the applicability of AVM with modulated data. Thereafter, the modulated version of the AVM algorithm was applied to individual fluorescence lines at higher dye densities. Each evaluation step was accommodated with an assessment of the distribution of the localized fluorescent dyes within the lines (FWHM) in order to gain an understanding of the dimensions on which fluorescence interference lithography can be used to create periodic patterns.

Concluding evaluations in this thesis addressed the investigation of selected examples of single molecule pairs or trios which were situated in very close proximity to one another i. e. on scales below the diffraction limit of light. The theoretical background of diffraction and its relationship to fluorescence microscopy is outlined in Chapter 2 while established methods and techniques that break or circumvent the diffraction barrier of light are introduced in Chapter 4. Due to the fact that fluorescence modulation with and without ExPAN is a direct consequence of the orientation of individual immobilized emitters, the separation of closely adjoined pairs of single molecules is accessible by fluorescence modulation under certain conditions. The investigations of this thesis contribute to an understanding of to what extent the molecular orientation of single emitters can be used to distinguish and separate fluorescence signal from pairs or trios below the diffraction limit of light.

All in all, this thesis focused on the characterization of the negative image obtained from interference lithography in a self-built fluorescent photoresist with special emphasis on the dimensions of the line width (FWHM), as outlined in Chapter 4. Herein, the evaluation of the line width was accomplished by means of an AVM algorithm which conducted a single molecule fitting procedure on fluorescence imaging data. The recorded data was obtained by fluorescence microscopy using modulation with and without ExPAN, whose principles are outlined of the initial chapter of this thesis (Chapter 2). The design and characterization of the self-built interference lithography set-up is addressed in Chapter 3.

2 Fluorescence modulation with and without ExPAN

Fluorescence spectroscopy techniques have gained in popularity over the past decades and are considered very essential for the investigation of biochemical and biophysical processes. Not only can fluorescence be widely used in medical diagnostics,[12][13] DNA sequencing,[14][15][16] and analytical chemistry,[17] it is also regarded a useful instrument for cellular and molecular imaging by fluorescence microscopy since intracellular molecules can be traced and localized down to very high resolution (super-resolution microscopy)[18] at high sensitivity (single-molecule detection).[19] Intracellular labeling of individual biomolecules and subsequent single molecule localization techniques have unraveled many interesting intracellular biochemical processes or structures. As an example, Yildiz *et al.*[20] were able to investigate the molecular motility of myosin V on actin by single fluorescence molecule localization. The results strongly indicated that the molecular motor myosin V walks hand-over-hand on actin. Especially the discovery of the green fluorescent protein (GFP) by O. Shimomura[21] in the 1960s led to a breakthrough in intracellular labelling. Subsequent isolation[22] and modification of the GFP genes led to a wide range of fluorescence proteins covering close to the entire visible spectrum[23][24][25] while simultaneously suitable to selectively tag proteins in vivo.[26][27] Due to the large impact of this discovery Osamu Shimomura, Martin Chalfie, and Roger Y. Tsien were jointly awarded the nobel prize in chemistry in 2008 "for the discovery and development of the green fluorescent protein, GFP."[28] The importance of fluorescence based technologies continues to grow so that fluorescence microscopes can be found in many biochemical and biophysical labs. The following sections give a basic insight into the interaction of light with fluorescence dyes with special focus on absorption and emission processes. Furthermore, the concept of fluorescence modulation and excitation polarization angle narrowing (ExPAN) is introduced. After giving a short overview of state-of-the-art fluorescence microscopy techniques along with their underlying concepts and principles, experimental details of the self-built fluorescence microscopy set-up using fluorescence modulation are explained. The results section focuses on the analysis of fluorescence imaging data of single ATTO 590 dyes recorded with and without ExPAN.

2.1 Theoretical background

2.1.1 The absorption of light

Light can be regarded as a combination of magnetic ($\vec{B}$) and electric ($\vec{E}$) field components oscillating in phase and perpendicular towards each other, and perpendicular to the propagation direction z.[1] The so-called electromagnetic wave possesses a frequency ν and carries energy in form of photons which can be referred to as a single quantum of light whose energy E depends on its frequency ν:

$$E = h\nu = \frac{hc}{\lambda} \tag{2.1}$$

Herein, h equals Planck's constant, c the speed of light, and λ the wavelength of light. While E and ν are linearly proportional towards one another, E is inversely proportional to the wavelength λ. The spectrum of visible light ranges from approximately 400 to 750 nm. Towards higher energies, ultra-violet (UV) waves (200-400 nm) and X-rays (<200 nm) occur. Toward lower energies, the infra-red region (IR) and micro-waves can be found. What kind of interaction occurs between the light and the matter depends, among other things, on the light's energy E and the molecular structure of the matter's molecules.[29] At very high intensities in the X-ray region, for example, photo-ionization may occur if the photons exceed the atom's or molecule's ionization energy. Furthermore, microwaves are often found to induce molecular rotation or torsion, IR radiation may excite molecular vibrations. Getting oneself sunburned is primarily an effect of UV irradiation. Reflection, refraction, and scattering are further examples of the interaction of light with matter.

In the course of this thesis, the interaction of light from the visible spectrum with molecules was used. Light from the visible spectrum can cause molecules to be excited from an electronic ground state to an electronically excited state. This process is referred to as absorption and is followed by various molecular processes releasing the excess energy when returning to the ground state.[19] Electronic states are referred to as S_n if its electronic nature is singlet, i. e. all electron pairs possess opposite spin. Transitions between the electronic ground state, S_0, and electronically excited states, S_1 or S_2, or vice versa, are therefore spin-allowed. Due to the wave-like nature of electrons, electronic states are best described by three dimensional wave functions ($\Psi(x,y,z) = \Psi(\vec{r}) = \Psi$). Each state possesses distinct energies and a transition between two different energy levels therefore requires the absorbed photon energy E to match the energy difference between both electronic states. However, matching photon energy is not the only prerequisite for an absorbing transition to occur. Absorption causes the electronic nature of a molecule to change from an initial wave function ($\Psi_0(\vec{r})$) to a final wave function ($\Psi_\mathrm{f}(\vec{r})$) and not all states can be arbitrarily transfered into others. In order to determine whether a certain transition is allowed, the transition dipole moment, $\vec{\mu}$, is calculated according to equation 2.2.[29]

$$\vec{\mu} = \int \Psi_f^*(\vec{r}) \cdot e\vec{r} \cdot \Psi_0(\vec{r}) dV \tag{2.2}$$

Herein, $\vec{r} = (x, y, z)$ refers to origin coordinates in the center of the molecule's charge distribution, Ψ_f^* to the conjugate complex electronic wave function of the final state, Ψ_0 to the electronic wave function of the initial state, and e to the elementary charge of an electron. In cases in which the transition dipole moment $\vec{\mu}$ gets very small by having values close to zero, the electronic transition can be considered dipole forbidden and is not observed e. g. in an absorption spectrum. The transition dipole moment serves as a measure for the possible occurrence of transitions. The optically forbidden one-photon transition between the ground state S_0 and the first electronic excited state S_1 in carotenoids is a very prominent example for a forbidden transition.[30][31][32] In cases in which the transition dipole moment $\vec{\mu}$ becomes large, the electronic transition can be considered allowed. For centro-symmetric molecules i. e. molecules that possess an inversion symmetry center, selection rules facilitate the identification of forbidden and allowed transitions. According to Laporte's selection rules,[33] strong absorption takes place if the parity of the involved wave functions changes either from gerade (g) to ungerade (u) or vice versa.[29] Herein, orbitals with u symmetry do not have an inversion center[a] whereas orbitals of g symmetry do. Looking back at the forbidden carotenoid transition between the electronic ground state and the first electronically excited state, both levels possess g-symmetry, namely A_g which leaves the transition from g to g forbidden according to Laporte's selection rule. By means of the transition dipole moment, the probability P_abs for a certain transition to occur can be given. The larger the absolute value of the transition dipole moment vector $||\vec{\mu}||$ the larger the probability gets that a photon is absorbed. Equation 2.3 shows that the probability P_abs shows a quadratic dependence on the absolute value of $\vec{\mu}$.

$$P_\mathrm{abs} \propto ||\vec{\mu}||^2 \tag{2.3}$$

So far, it became clear that the process of absorption depends on the transition dipole moment which in turn relies on the molecular and electronic structure of the molecule. In addition to the probability for absorption, the photon energy required for the optical transition has to be provided by the light in order for excitation to take place. The molecular events following absorption are best explained by a Jablonski diagram, as seen in the

---

[a] The molecule is required to have an inversion center nonetheless in order to apply Laporte's selection rules. The molecule's center of inversion remains while the orbital is not inversion symmetric.

following section.

2.1.2 Jablonski diagram

A Jablonski diagram illustrates processes that follow upon excitation from an electronic ground state S_0 to an electronically excited state, for example S_1 or S_2.[34] Herein, each electronic energy level contains vibrational states which are labeled by their vibrational quantum number $v = 0, 1, 2, 3$. Absorption usually occurs from the vibrational ground state ($v = 0$) within the electronic ground state S_0 since excited vibrational states are not substantially populated at room temperature in many cases. In cases in which the equilibrium positions of the molecule's atoms differ between an excited state $S_{n>0}$ and the ground state S_0, the time scales of electronic transitions (10^{-15} s) are much shorter than for nuclei rearrangement to occur. As a consequence, the molecular geometry remains constant during absorption of a photon and so-called vertical transitions take place (see violet and blue arrows in figure 2.1). This observation is referred to as the Franck-Condon principle.[35] Accordingly, a fluorescence molecule is usually excited to a higher vibrational level within the excited electronic state, preferentially those vibrational states whose wave functions resemble the wave function from the vibrational ground state of the electronic ground state best.

A number of different pathways exist for the absorbed energy to be released when the molecule returns to its electronic ground state. Not all processes will be addressed here, but the focus will be on the events depicted in the Jablonski diagram in figure 2.1. Usually the first process to occur after absorption is fast vibrational relaxation to the vibrational ground state of the electronically excited state. The excess vibrational energy is released to surrounding solvent molecules on time-scales ranging from femto- to picoseconds ($10^{-15} - 10^{-12}$ s). This non-radiative process is depicted by dotted, curved arrows in grey and generally follows upon all events which caused excited vibrational levels to be populated (like fluorescence or phosphorescence).[36]

Higher electronically excited states, like S_2, usually release their excess energy by internal conversion (IC).[37] IC can occur when the energy difference between the higher and the lower electronic state is so small that the vibrational ground level of the higher electronic state ($S_2, v = 0$) can directly interact with a vibrational excited state of the lower electronic level ($S_1, v > 0$). This process can also occur between the first electronically excited state ($S_1, v = 0$) and the electronic ground state ($S_0, v > 0$) if the energy gap is appropriately small (see curved, grey arrows in figure 2.1). Due to the fact that the energy difference between electronic states decreases for higher levels and that IC occurs on time-scales of picoseconds (10^{-12} s), IC usually dominates the de-excitation of levels larger than S_1. While vibrational relaxation and IC lead to a fast population of the lowest vibrational

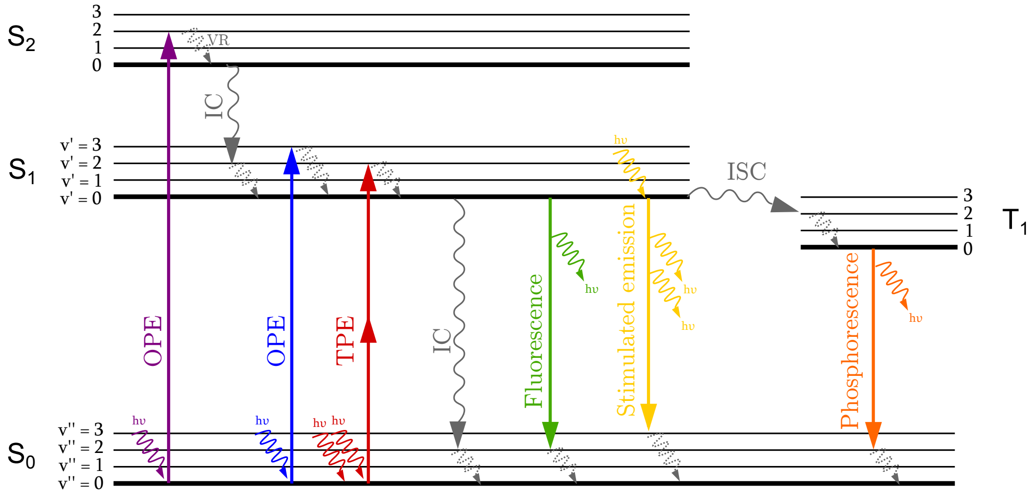

Figure 2.1: Jablonski diagram for transitions from the electronic ground state S_0 to electronically excited states S_1 and S_2 and subsequent relaxation processes. OPE: one-photon excitation; TPE: two-photon excitation; VR: vibrational relaxation (dotted curved arrows); IC: internal conversion; ISC: intersystem crossing; $h\nu$: radiative transitions.

state of $\mathrm{S}_1, \mathrm{v} = 0$, other processes than IC compete for the de-excitation of S_1.

Fluorescence emission can be regarded as the opposite process of absorption. Instead of absorbing energy in form of photons, excess energy is released by emitting photons of certain energy. Therefore, fluorescence is a radiative process that leads to the return to the electronic ground state as depicted by the green arrow in figure 2.1. In many ways, fluorescence follows the same rules as absorption. Again, the Franck-Condon principle applies and since the spacing of the vibrational levels as well as the vibrational wave functions of the excited states are quite similar to those of the ground state, fluorescence leads to the population of an excited vibrational level in the electronic ground state ($\mathrm{S}_0, \mathrm{v} > 0$). In fact, likely absorptions from $\mathrm{S}_0, \mathrm{v}'' = 0$ to $\mathrm{S}_1, \mathrm{v}' = 3$ are often found to be similarly likely as fluorescence $\mathrm{S}_1, \mathrm{v}' = 0$ to $\mathrm{S}_0, \mathrm{v}'' = 3$. Therefore, a fluorescence emission spectrum appears to be mirrored with respect to the absorption spectrum. Moreover, the probability of fluorescence P_{fl} is also depending quadratically on the absolute value of the transition dipole moment $\vec{\mu}$. The emitted photons often contain less energy than the absorbed photon which is why the fluorescence emission spectra appear red-shifted with respect to the absorption spectra. This effect is called Stokes-shift and implies that the emission light's wavelength is larger than the excitation light's.[37] This feature is quite beneficial when designing fluorescence microscopes. Due to the shift of wavelength, special optics provide the possibility to separate fluorescence light emitted by a sample of interest from the excitation light by using dichroic mirrors or optical filters.

Another de-excitation path of the vibrational ground state of the first electronically excited state is called intersystem crossing (ISC). So far, only transition between singlet states have been addressed in which all electron spins are paired. Even in excited singlet states, spins occupied in different orbitals are opposite to one another therefore resulting in a zero total magnetic momentum. In triplet states, spins occupied in different orbitals possess the same spin which is why triplet states show a total magnetic momentum other than zero. In order for ISC to occur, a good overlap between the interacting wave functions is required (figure 2.1)). Additionally, the system's overall angular momentum is required to remain constant which is why this transition is called spin-forbidden.[29] A spin flip can only occur when the change in spin momentum is compensated by other processes, for example spin-orbit coupling. This is rather improbable and seldom the case. The radiative de-excitation of the vibrational ground state of the triplet state is called phosphorescence (see orange arrow in figure 2.1). Returning to the singlet ground state again requires a spin flip which is why triplet states are usually much longer lived than singlet states.[37]

So far, it has been explained that in many cases instantaneous absorption is quickly followed by vibrational relaxation and IC to the vibrational ground level of the first electronically excited state. Spontaneous fluorescence emission, internal conversion, and intersystem crossing are processes competing for returning the excited molecule to the ground state. Each transition can be assigned a rate constant which is proportional to the probability per time unit that a specific transition occurs. Typical rate constants are $k_{\mathrm{IC}} \approx 1\,\mathrm{ns}^{-1}$ for internal conversion and $k_{\mathrm{fl}} \approx 0.1\,\mathrm{ns}^{-1}$ which indicates that the process of fluorescence is ten times less probable than releasing the energy by internal conversion.[29] Each process can also be assigned a specific quantum yield which is defined by the ratio of the rate constant for a given process and the sum of all rate constants depopulating the first excited state. As an example, the fluorescence quantum yield Φ_{fl} is defined in equation 2.4 only taking fluorescence, IC, and ISC into account. The inverse of the fluorescence rate constant is equal to the fluorescence lifetime ($\tau_{\mathrm{fl}} = 1/k_{\mathrm{fl}}$). Typical fluorescence lifetimes of dyes lie around 10 ns.[19]

$$\Phi_{\mathrm{fl}} = \frac{k_{\mathrm{fl}}}{k_{\mathrm{fl}} + k_{\mathrm{IC}} + k_{\mathrm{ISC}}} \tag{2.4}$$

Further interactions exist for releasing absorbed energy and returning to the electronic ground state, e. g. fluorescence quenching and energy transfer mechanisms like fluorescence resonance energy transfer (FRET). As a last de-excitation mechanism relevant for this thesis, stimulated emission is introduced, an effect that was first described by Albert Einstein.[38] Stimulated emission is depicted as a yellow arrow in the Jablonski diagram shown in figure 2.1. In contrast to spontaneous emission which is referred to as fluorescence, emission can also be stimulated by an additional light source. The stimulation of this transition requires the incoming photons to possess the specific amount of energy that equals the energy difference of the desired transition. The additional external photon inducing stimulated emission results in a second photon of identical properties with respect to phase, frequency, polarization, and direction. In other words, the externally applied electromagnetic field interacts with the molecule in its excited state and increases the probability for the corresponding transition to occur. Due to the fact that the resulting photon shares the same properties of the incident photon, it can also be spectrally separated from remaining fluorescence light since the wavelength of the stimulated emission beam is red-shifted with respect to the wavelength of fluorescence. Nowadays, stimulated emission is considered the core piece mechanism for building lasers[39][40] (LASER, light amplification by stimulated emission of radiation). Additionally, stimulated emission is part of the super-resolution technique "stimulated emission depletion" (STED) microscopy.[41][42] Stimulated emission is used in the course of this thesis in order to increase the photo-selectivity of excitation. The concept of photo-selection and exploiting this feature for a fluorescence microscopy technique will be introduced in the following sections.

2.1.3 The modulation of fluorescence signals from single molecules

Fluorescence dyes can be photo-selectively excited by using linearly polarized light for which the electric field component $\vec{E}$ oscillates in one specific plane, the so-called polarization plane of a light wave. If the polarization plane matches the orientation of the molecule's transition dipole moment $\vec{\mu}$, light can be absorbed.[43] The probability of absorption P_{abs} depends on the dot product between the electric field vector $\vec{E}$ and the transition dipole moment $\vec{\mu}$ as shown in equation 2.5. Solving the dot product reveals that P_{abs} depends quadratically on both the absolute magnitude of the transition dipole moment $||\vec{\mu}||$ and the absolute magnitude of the electric field vector $||\vec{E}||$.

$$P_{\text{abs}} \propto (\vec{E} \cdot \vec{\mu})^2 = ||\vec{E}||^2 ||\vec{\mu}||^2 \cos^2(\alpha) \tag{2.5}$$

P_{abs} is proportional to the squared cosine function of the angle α between $\vec{E}$ and $\vec{\mu}$ and yields a maximum when $\vec{E}$ is oriented exactly parallel to $\vec{\mu}$ ($\alpha = 0°$). This means that only a selected portion of fluorescence dyes in a sample of randomly oriented molecules is excited and emission can only be expected from this portion to occur. In cases in which rotational diffusion of the molecules is omitted, e. g. by immobilizing dyes onto a glass surface, the fluorescence response can be expected to be linearly polarized with a fluorescence probability P_{fl} which is also depending quadratically on the transition dipole moment's absolute value.[8][19]

Excitation does not only occur when the light's polarization plane is oriented exactly parallel towards the transition dipole moment. Even if the electric field component $\vec{E}$ is tilted away from $\vec{\mu}$ by an angle α, excitation may occur according to equation 2.5. Fluorophores oriented exactly perpendicular to $\vec{\mu}$ (α equals 90°) show no absorption. Fluorescence can be regarded as the reverse process to absorption, thus the fluorescence probability P_{fl} of single molecules is dependent in the same way on $\vec{\mu}$ and α as P_{abs}. The more photons are absorbed the more photons can eventually be emitted as fluorescence. Therefore, in linear optical systems it is assumed that the emitted fluorescence intensity I_{fl} is also dependent on the angle α[44] between the orientation of the light's polarization vector $\vec{E}$ and the molecule's transition dipole moment $\vec{\mu}$ which can be described by equation 2.6.

$$I_{\mathrm{fl}} \propto P_{\mathrm{abs}} \propto \cos^2(\alpha) \tag{2.6}$$

The molecule's transition dipole moment orientation within the chromophoric structure of the fluorescence dye usually remains constant as long as the solvent is not changed. If a fluorescence molecule is immobilized on a surface, the orientation of the chromophoric structure determines the orientation of $\vec{\mu}$. If the plane of $\vec{E}$ is rotated with a fixed angular velocity, the absorption response and thus the fluorescence response is modulated between a maximum and a minimum value depending on the orientation of the excitation light's polarization plane.[45] The resulting fluorescence signal reaches a maximum value if the angle α between $\vec{E}$ and $\vec{\mu}$ is zero (compare magenta arrow in figure 2.2). If the plane of $\vec{E}$ rotates further and the molecule remains fixed, the fluorescence intensity decreases until a minimum value is reached at $\alpha = 90°$. For intermediate cases as shown for the blue ($\alpha = 30°$) and yellow ($\alpha = 60°$) arrows in figure 2.2, the I_{fl} is given by equation 2.6. Due to symmetry of the squared cosine function, the orange ($\alpha = 120°$) and green ($\alpha = 150°$) arrows have the same lengths as yellow and blue, respectively. The final result is a periodic function which will often be referred to as fluorescence modulation. Since the rotation frequency of the light's polarization plane is experimentally controllable, fluorescence modulation can be easily adapted to the experimenter's needs. In figure 2.2, the fluorescence intensity I_{fl} is depicted in dependency of the angle α. Due to the direct

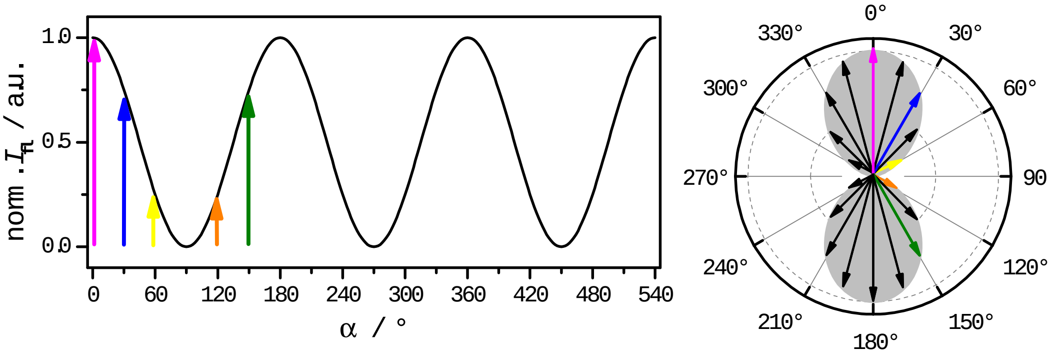

Figure 2.2: Plot of normalized fluorescence emission intensity (I_{fl}) depending on α (angle between $\vec{E}$ and $\vec{\mu}$) according to equation 2.6. Colored arrows show I_{fl} values corresponding to given α. $\alpha = 0°$, pink. $\alpha = 30°$, blue. $\alpha = 60°$, yellow. $\alpha = 120°$, orange. $\alpha = 150°$, green. Angular polar plot of I_{fl} to the right.

relationship between the angular velocity and time, it is also possible to express fluorescence modulation curves in time coordinates t which are then called time-dependent fluorescence traces. Differently oriented molecules will each show modulating fluorescence traces peaking at different times which can be described by the phase parameter φ of the underlying squared cosine function. It is also useful to express photo-selection in form of a polar plot in which the fluorescence intensities are plotted against α in angular coordinates, as shown in figure 2.2 to the right. A polar plot directly shows the excitation probability of a single dye by linearly polarized light for a certain angle between $\vec{\mu}$ and $\vec{E}$. The shape of the polar plot looks similar to a dumbbell which is why it will be referred to as the photo-selection or excitation probability dumbbell. Two differently oriented fluorescence dyes will show two excitation probability dumbbells which are rotated with respect to one another. By exploiting this orientation difference, controlled fluorescence modulation can be used to distinguish individual molecules by their phase even if their modulation signals overlap spatially.

The typical photo-selection distribution for one-photon excitation is described by the cosine-squared dependency given in equation 2.6.[19] One simple way of enhancing photo-selection or in other words reducing the excitation probability for increasing angle mismatch between $\vec{E}$ and $\vec{\mu}$, is multiphoton excitation. In two-photon excitation (TPE), as the name already suggests, two photons with much larger wavelengths are used to excite the molecule to its electronically excited states (see red arrow in figure 2.1). The selection rules for TPE differ substantially from the ones for one-photon excitation (OPE).[46] As an example, the transition from carotenoids from the ground state S_0 to the first electronic excited state S_1 is optically forbidden for OPE, whereas TPE can be used to directly populate S_1.[30] In order for multi-photon excitation to occur, two photons are required to interact with the molecule simultaneously[b] which is accomplished by using large laser intensity in spatially very confined excitation areas. The probability of this non-linear optical process to occur is quadratically dependent on the excitation energy. As a consequence, photo-selection for TPE depends on the cosine to the fourth power of the angle between $\vec{E}$ and $\vec{\mu}$ ($\cos^4(\alpha)$). Moreover, three photon excitation shows a $\cos^6(\alpha)$ dependency increasing photo-selection even further.[19] Another technique for improving photo-selection of excitation was recently introduced[8] and uses stimulated emission in order to selectively narrow the angle range for excitation. This technique named excitation polarization angle narrowing (ExPAN) is introduced in the following section.

---

[b] Sequential absorption may also be possible if a well defined intermediate state exists.

2.1.4 Excitation polarization angle narrowing (ExPAN)

Regular fluorescence modulation and photo-selection cause differently oriented dyes to be excited with differing probabilities. Assuming an angle of 45° between the electric field vector $\vec{E}$ and the molecule's transition dipole moment $\vec{\mu}$, the absorption probability can be approximated to be 0.5 relative to the maximum excitation if α were 0°. Photoselection can be considered rather unspecific with respect to the goal to distinguish the fluorescence contributions by their phase. If two dyes were to be positioned in close proximity towards each other with a difference in orientation of 45°, the fluorescence contribution from one dye would be maximum while the other dye would still contribute half as much fluorescence. Summing two squared cosine functions with different phases (assuming each squared cosine function to be the result from one molecule) results in yet another squared cosine function. Due to the fact that only the total fluorescence contribution is accessible via measurements, it becomes difficult to identify the individual signals without having prior knowledge of the system. Signal identification would greatly improve if the photo-selection would be enhanced, for example by narrowing the angle range for excitation. As previously mentioned, this can be obtained by multi-photon experiments.

Another way of improving photo-selection has recently been realized by the use of stimulated emission in addition to the regular excitation.[8][10] The technical clue herein is that the electric field vector $\vec{E}_{\mathrm{se}}$ of the linearly polarized stimulated emission beam is oriented exactly perpendicular to the electric field vector $\vec{E}_{\mathrm{abs}}$ of the linearly polarized excitation beam. The cosine-squared probability distribution also applies to stimulated emission which is why stimulated emission preferentially occurs when the molecule's transition dipole moment is oriented parallel to the stimulated emission beam's polarization plane. In this case, the absorption probability is at its minimum anyway which is why only a negligible number of fluorescence dyes would be in the excited state in the first place. On the other hand, molecules whose transition dipole moments are oriented along the excitation light's polarization plane do not experience substantial influence from stimulated emission since its corresponding de-excitation probability possesses a minimum. Fluorescence emission can occur almost unhindered for those molecules. For intermediate orientations, dyes are excited with a certain probability and de-excited at another probability. It can be regarded as a competition of the processes of stimulated emission and spontaneous emission for the transition from the excited state S_1 to the ground state S_0. Upon increasing the intensity of the stimulated emission (I_{se}) beam, the process of stimulated de-excitation is favored over spontaneous emission. As a consequence, the angle range for which fluorescence is detected is substantially narrowed. In other words, photo-selection is improved and leads to an adaption of the cosine-squared shaped function as seen in figure 2.3. The peaks appear at the same positions but are much narrower

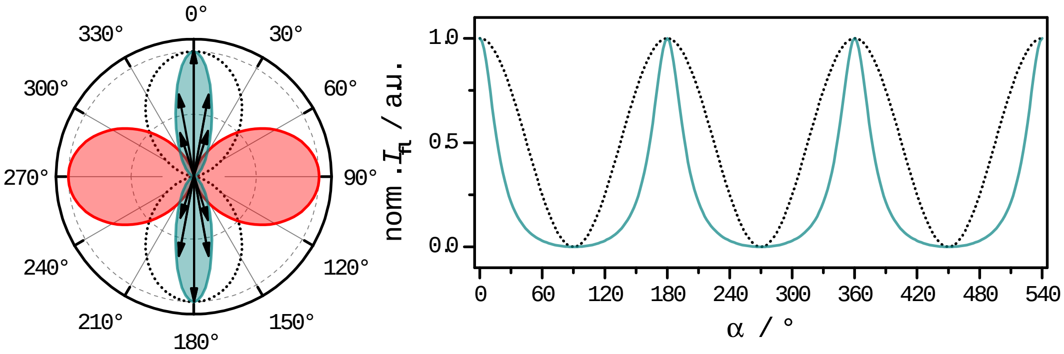

Figure 2.3: Principle of ExPAN to the left. Angular polar plot of the reduced excitation probability (blue) under the influence of a second, stimulated emission beam (red). To the right, the dotted curve shows the regular cosine squared fluorescence modulation plot ($I_{fl}(\alpha)$) according to equation 2.6 while the blueish curve shows $I_{fl}(\alpha)$ under ExPAN conditions according to the ExPAN equation 2.13.

in width. This effect was named excitation polarization angle narrowing (ExPAN).

In quantitative terms, the fluorescence intensity I_{fl} can be regarded proportional to the dye population in the first excited state N_1,[8][10] which in turn can be expressed in terms of rate constants[47] as shown in equation 2.7.

$$N_1 = \frac{k_{abs}}{k_{abs} + k_{fl} + k_{se}} \tag{2.7}$$

Herein, k_{abs}, k_{fl}, and k_{se} are rate constants for absorption, fluorescence emission, and stimulated emission, respectively. Other de-excitation processes have been neglected. The magnitude of rate constants is proportional to their transition probability and by taking equation 2.5 into account, their dependency on the angle α can be expressed as:

$$k_{abs}(\alpha) = k_{0,abs} \cdot P_{abs} = k_{0,abs} \cdot (\vec{E}_{abs} \cdot \vec{\mu}_{abs})^2 \tag{2.8}$$

and

$$k_{se}(\alpha) = k_{0,se} \cdot P_{se} = k_{0,se} \cdot (\vec{E}_{se} \cdot \vec{\mu}_{se})^2 \tag{2.9}$$

Herein, $k_{0,abs}$ and $k_{0,se}$ are the maximum rate constants for absorption and stimulated emission, respectively. For simplicity of calculation, $\vec{E}_{abs}$ and $\vec{E}_{se}$ are defined as two-dimensional unity vectors and $\vec{\mu}_{abs}$ and $\vec{\mu}_{se}$ are taken to be collinear, as shown in equation 2.10

$$\vec{E}_{abs} = \begin{pmatrix} 1 \\ 0 \end{pmatrix} \quad \text{and} \quad \vec{E}_{se} = \begin{pmatrix} 0 \\ 1 \end{pmatrix} \quad \text{and} \quad \vec{\mu}_{abs} = \vec{\mu}_{se} = \begin{pmatrix} \cos(\alpha) \\ \sin(\alpha) \end{pmatrix} \tag{2.10}$$

A closer look at the vector expressions for $\vec{\mu}_{\text{abs}}$ and $\vec{\mu}_{\text{se}}$ makes clear that they are unity vectors as well since their magnitude also equals one ($\|\vec{\mu}_{\text{abs}}\| = \sqrt{\cos^2(\alpha) + \sin^2(\alpha)} = 1$). By inserting all unity vectors in equation 2.10 into the given angle dependent rate constant functions (Eqs. 2.8 and 2.9), the population of the first excited state becomes

$$N_1 = \frac{k_{0,\text{abs}} \cos^2(\alpha)}{k_{0,\text{abs}} \cos^2(\alpha) + k_{\text{fl}} + k_{0,\text{se}} \sin^2(\alpha)} \tag{2.11}$$

This equation can be further simplified as follows. First, it can be assumed that the rate constant for fluorescence emission is much larger than the rate constant for absorption ($k_{0,\text{abs}} \ll k_{\text{fl}}$) because the intensities commonly used in wide-field fluorescence microscopy do not induce fluorescence saturation. In a saturated fluorescence system, the increase of excitation intensity is not followed by an increase of fluorescence emission due to the fact that the spontaneous emission transition is the limiting factor and nearly all dyes are in the excited state. Whether saturation occurs depends on the photo-physical properties of the dye and the excitation light source. A quantitative assessment of this relationship $k_{0,\text{abs}} \ll k_{\text{fl}}$ is given in section 2.1.5. Further simplification of equation 2.11 is achieved by introducing a quantification measure for the strength of the ExPAN effect. This factor f_s specifies the ratio between the maximum rate constant for stimulated emission and the rate constant for spontaneous fluorescence emission ($f_s = k_{0,\text{se}}/k_{\text{fl}}$). The population equation 2.11 can be rearranged to yield equation 2.12.

$$N_1 \approx \frac{k_{0,\text{abs}}}{k_{\text{fl}}} \frac{\cos^2(\alpha)}{1 + f_s \sin^2(\alpha)} \tag{2.12}$$

For large ExPAN factors, the stimulated emission dominates over spontaneous emission, thus causing the narrowing of the excitation range. Since the observed fluorescence intensity I_{fl} is proportional to the population of the first excited state N_1, I_{fl} can be expressed as angle dependent function given in equation 2.13.

$$I_{\text{fl}} \propto \frac{\cos^2(\alpha)}{1 + f_s \sin^2(\alpha)} \tag{2.13}$$

In the course of this thesis, equation 2.13 is often referred to as the fundamental ExPAN function.

2.1.5 Spectral properties of ATTO 590

The fluorescence dye used in all parts of this thesis is called ATTO 590. Its structure contains a xanthene backbone which is depicted by the orange color in figure 2.4. Typical xanthene dyes, like rhodamine B, rhodamine 6G, rhodamine 101, and rhodamine 630 usually exhibit high fluorescence quantum yields and small Stokes shifts of approximately 20 - 30 nm with emission maxima (λ_{fl}) around and below 600 nm in alcoholic solutions.[48] The distribution of π-electrons in the chromophore can be described by two mesomeric structures in which the positive charge is located with either nitrogen atom. Both mesomeric structures are therefore identical which is why xanthene dyes do show a static dipole moment parallel to the long axis of the molecule neither in the ground state nor in the excited state. The electronic rearrangement during absorption occurs along the long axis of the chromophore which is why the transition dipole moment is oriented parallel to it, as depicted by the arrow in figure 2.4.[49]

Compared to dyes only containing the xanthene backbone, the emission and absorption maxima of ATTO 590 are red-shifted. In ATTO 590, both nitrogen atoms are part of an additional ring structure including further carbon double bonds. The extended π-system requires slightly less energy for the transitions to occur, thus resulting in a red-shift of both spectra. ATTO 590 is provided as an isomeric mixture in which the second carboxy group is attached to the benzene ring either in para position with respect to the first carboxy group or in para position with respect to the xanthene backbone. In principle, both isomers show equal absorption and emission properties. The absorbance and fluorescence emission spectra recorded from a dilution of ATTO 590 in methanol are shown in figure 2.5. Maximum absorption was registered at 594 nm (Literature: 594 nm,[50] 593 nm[51]), while maximum fluorescence was detected at 624 nm (Literature: 622 nm,[51] 624 nm[52]). In biological systems, labelling with red-absorbing dyes is often favored over labelling with blue-absorbing dyes. Due to the fact that Rayleigh and Raman scattering scale with the inverse wavelength to the forth power, increased values of λ_{fl} lead to a significant reduction

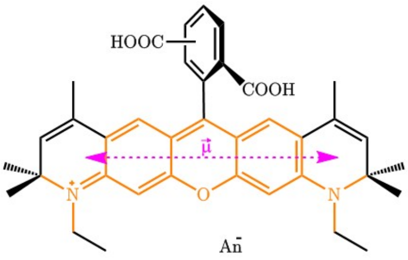

Figure 2.4: Molecular structure of ATTO 590 including the transition dipole moment's orientation.

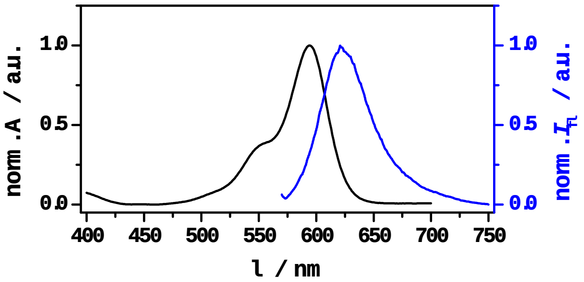

Figure 2.5: Normalized absorbance and normalized fluorescence emission spectra of ATTO 590 free carboxy acid in methanol.

of the background signal from the sample with in turn improves signal sensitivity.[48]

The fluorescence quantum yield of ATTO 590 is given to be $\Phi_{\text{fl}} = 80\%$ with a fluorescence lifetime of $\tau_{\text{fl}} = 3.7\,\text{ns}$.[50][53] Together with its thermal and photochemical stability this makes ATTO 590 excellently suitable for a wide range of fluorescence microscopy techniques especially with respect to high sensitivity measurements. To name a few examples, ATTO 590 is readily used for single molecule detection in high resolution microscopy,[54] like PALM, dSTORM, and STED, or distance quantification measurements using FRET.[55]

As previously stated, wide-field illumination intensities do not cause singlet state saturation for typical fluorescent dyes. The following mathematical assessment is based on the photo-physical properties of ATTO 590 and typical illumination intensities used throughout this thesis.[47][56] If a 1 mW light beam with a wavelength of 594 nm and a Gaussian profile is used to illuminate an area[c] of about $1000\,\mu\text{m}^2$, the average peak intensity is given by $I_p = 100\,\text{W/cm}^2$. This value can be expressed as a photon flux $J_p = I_p/E = (I_p\lambda)/(hc) \approx 3 \cdot 10^{20}\,\text{photons/(cm}^2\,\text{s)}$. The rate constant for absorption k_{abs} can be obtained by multiplying the fluorophore's optical cross section σ_{abs} with the photon flux J_p in which σ_{abs} can be derived from the decadic extinction coefficient ε of the dye.[57] For ATTO 590, this gives $\sigma_{abs} = \varepsilon \cdot \ln(10) \cdot 1/N_A \approx 4.6 \cdot 10^{-16}\,\text{cm}^2\text{/molecules}$ in which ε was taken to be $120\,000\ \text{L/(mol cm}^2)$[50][51] and N_A is Avogadro's constant, $N_A = 6.02 \cdot 10^{23}\,\text{mol}^{-1}$. The resulting rate constant for absorption under the named conditions is then $k_{\text{abs}} = \sigma_{\text{abs}} J_p \approx 1.4 \cdot 10^5\,\text{s}^{-1}$. This value can be compared to the rate constant for fluorescence which can be obtained from the fluorescence lifetime τ_{fl} as $k_{\text{fl}} = 1/\tau_{\text{fl}} \approx 2.7 \cdot 10^8\,\text{s}^{-1}$. Even if the illumination intensity would be increased to approximately 20 mW, k_{fl} would still exceed k_{abs} by a factor of 100 which supports the assumption that fluorescence saturation does not play a role in typical wide-field illumination set-ups.

2.1.6 Fluorescence microscopy

So far, the general concept of fluorescence has been outlined along with exploiting the feature of photoselectivity with respect to fluorescence modulation and excitation polarization angle narrowing (ExPAN). Throughout this thesis, these techniques were applied in fluorescence microscopy set-ups whose fundamental characteristics are addressed in this section. In fluorescence microscopy, a sample is illuminated using monochromatic excitation light which is absorbed by the fluorescent dyes. The successive release of

---

[c] The illumination area is circular and sligthly exceeding the edges of the rectangular field of view of the EMCCD (electron-multiplying charge-coupled device) camera used. It is assumed that the diagonal of the circular illumination area ($\sim$ 35.7 µm) exceeds the diagonal of the field of view ($\sim$ 32 µm) by no more 10%.

the excess energy in form of photons is detected, for example by avalanche photodiodes (APD)[58] or charge-coupled devices (CCD).[59] Due to the Stokes-shift (red-shift of emission spectrum), the excitation light's wavelength differs from the emission light's wavelength which is why the latter can be experimentally separated from the former by the use of appropriate dichroic beamsplitters and filters. The spectral separation is especially beneficial since the same objective can be used for sample excitation as well as fluorescence emission collection which facilitates the overall set-up design. This configuration is named epifluorescence microscopy[19] and is widely used for fluorescence imaging purposes.

The fluorescence microscopy set-ups designed and built in the course of this thesis were used mostly in wide-field epifluorescence configuration. Wide-field illumination is obtained by focusing a collimated beam onto the center of the back focal plane of the objective by using a lens, thus causing a large area of interest to be illuminated.[29] The alternatives to wide-field illumination rely on point based scanning techniques, like confocal laser scanning microscopy (CLSM)[60] for example. Point illumination is achieved when the collimated excitation light is focused into the sample by the objective lens itself (no focusing prior to the objective occurs). In order to obtain a full image, the illumination point is scanned through the sample and the results are put together to a final image afterwards. Despite the fact that point-based scanning techniques put less strain on the sample since the illumination volume is confined to a diffraction-limited spot in x, y, and z, wide-field techniques were preferentially used in this thesis due to set-up simplicity. Even though wide-field illumination causes much more out of focus excitation which leads to higher background signals and decreased signal-to-noise ratios, the feature of fluorescence modulation already requires additional measuring time which is why wide-field was preferred over point-based illumination in this work.

Fluorescent dyes commonly used in fluorescence microscopy are sized on sub-nanometer scales for dye molecules (xanthene, cyanine, rhodamine), while the beta-barrel structure of fluorescent proteins is approximately 2-4 nm high and wide.[61] Even if one individual dye or fluorescent protein is imaged with a fluorescence microscope, the final signal response will be magnitudes larger in diameter than the size of the fluorescence dye itself. This rather unfortunate feature is due to diffraction by the circular aperture of the objective. In more general terms, the diffraction from a circular aperture creates a bright center with concentric rings, called Airy pattern[62] as shown in figure 2.6. The Airy pattern can be easily visualized in the lab by passing a laser beam through a continuously variable iris. By slowly closing the iris diaphragm, it starts acting as a pinhole and reveals the Airy diffraction pattern at some distance behind the iris.

The intensity distribution $I(\gamma)$ of the Airy diffraction pattern can be mathematically calculated from the Fraunhofer diffraction equation[1][2] for circular apertures in the far field[d] as shown in equation 2.14.

$$I(\gamma) = I_0 \left(\frac{2J_1(\rho)}{\rho} \right)^2 \quad \text{with} \quad \rho = \frac{2\pi r \sin(\gamma)}{\lambda} = kr\sin(\gamma) \tag{2.14}$$

Herein, I_0 is the maximum intensity in the center of the Airy distribution, $J_1(\rho)$ the Bessel function of the first order, $k = 2\pi/\lambda$ the magnitude of the wave vector, r the radius of the circular aperture, and γ the maximal half-angle of the cone of light entering or exiting the objective's lens. The radius of the first dark ring in which $I(\gamma) = 0$ can be derived from the first value for which the Bessel function $J_1(\rho)$ becomes zero which is the case at $\rho \approx 3.8317$.[63] Rearranging equation 2.14 yields equation 2.15 which relates the angle at which the first minimum of the Airy function occurs to the wavelength and the aperture's diameter D.

$$\sin(\gamma) = \frac{\rho\lambda}{2\pi r} = \frac{3.8317 \cdot \lambda}{\pi D} \approx 1.22\frac{\lambda}{D} \tag{2.15}$$

The importance of this equation becomes apparent when thinking about resolving two point sources in close proximity to one another. If the center of the first molecule's Airy pattern lies within the angle of the first Airy pattern minimum of the second molecule, both signals cannot be resolved anymore in a conventional fluorescence microscope. According to the Rayleigh criterion,[64] the resolution limit is just met if the minimum of one Airy function coincides with the maximum of the other. Equation 2.15 then translates into the angular resolution limit in equation 2.16 for very small angles which depends only on the wavelength of light and the optical parameters of the objective.

$$\gamma \approx 1.22\frac{\lambda}{D} \tag{2.16}$$

All in all, it is neither possible to focus a laser beam onto an infinitely small spot nor imaging a point source as such. When considering a sample of many fluorescent dyes, regular fluorescence imaging can be regarded as diffraction limited with respect to resolution if the optical set-up is optimized to yield the angular resolution given in equation 2.16. Each point source in a diffraction limited system responds to the illumination with a distribution of the size of the diameter of the Airy disk pattern to the first minimum (D). The recorded image is consequently also limited to diffraction. While the Airy function is free from aberration, the fluorescence response is sensitive to many factors, like chromatic aberration from further optics in the detection path, beam alignment and the correct positioning

---

[d] In this case, the distance from the aperture to the observed pattern (L) is larger than the ratio between the square of the apertures size (D) and the wavelength of light ($D^2/\lambda \ll L$).

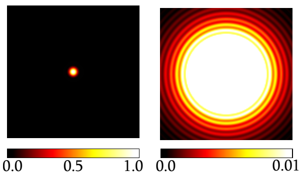

Figure 2.6: Airy diffraction pattern.

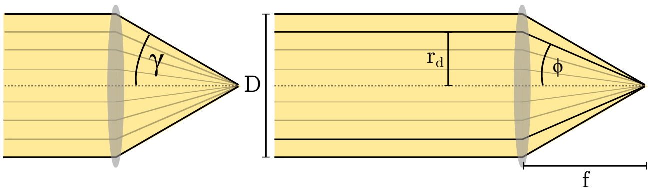

Figure 2.7: Numerical aperture and Abbe's sine condition.

of the detector with respect to focal plane. Experimental factors influence the distribution which is why the fluorescence distribution from a single emitter in a microscope is called point-spread-function (PSF). In many cases, the PSF can be approximated by an Airy pattern function according to equation 2.14, especially if the emitting dyes are recorded in focus and optics are very well aligned. However, in defocused systems, the PSF changes significantly from the Airy distribution which is why other functions are required to characterize the image.[65][66][67] Usually, the best way to find the true PSF is by measuring it experimentally by point emitting sources like bright quantum dots. The characteristic changes of the PSF's shape depending on the distance towards the focal plane gave rise to techniques in which the position of individual emitters became accessible in the third dimension.[65][68][69][70]

The image formation can be considered as a convolution of all individual single dye emitters with the corresponding PSF. The resolution limit is characterized by Abbe's law[71] in equation 2.17.

$$d = \frac{\lambda}{2n_r \sin(\gamma)} = \frac{\lambda}{2\mathrm{NA}} \tag{2.17}$$

Herein, the resolution limit d refers to the smallest distance between two point sources that are resolved. The distance d scales linearly with the wavelength so that better resolution capability is possible for smaller wavelengths. Additionally, d is inversely proportional to the numerical aperture of the objective (NA). NA is given by the product of the objective's index of refraction (n_r) and the sine of the half cone angle (γ) of the objective's lens (see equation 2.17 and figure 2.7). It can be considered as a measure for the size of the fluorescence collection cone. Due to the fact that the sample irradiates fluorescence into all directions, the objective's collection cone determines how many of the emitted photons are collected and directed to the detection unit. The more photons are collected the better is the signal to noise ratio and the sensitivity of the measurements improves.[29] Large numerical apertures (typically around 1.4) are nowadays frequently used in microscopy techniques that desire high resolution. A brief overview of super-resolution techniques is given in the theoretical section of Chapter 4.

One important consequence of Abbe's law is illustrated in figure 2.7. For an infinity corrected lens, the ratio between the off-axis distance r_d of a beam and the sine of the angle between the corresponding ray and the optical axis ($\sin(\phi)$) is constant.[71][72] For an infinity corrected microscope objective which consists of many lenses in row the constant is given by the effective focal length f of the system. This means that the angle at which the beam exits the objective toward the focal point depends on the lateral position on the back focal plane of the objective. By increasing the off-axis distance r_d, the angle ϕ also increases ($r_d = f \sin(\phi)$). This relationship will be of great use in Chapter 3, in which interference between two plane waves is accomplished in the focal plane of the microscope's objective.

2.2 Experimental section - Material and methods

The following experimental sections will provide a detailed set-up description of the self-built fluorescence microscopy set-up using fluorescence modulation and excitation polarization angle narrowing (ExPAN). In contrast to the ExPAN technique in the literature,[8] continuous wave (CW) excitation was replaced by pulsed excitation. The sample preparation method is given along with a description of the measurement's procedure.

2.2.1 Set-up details

A schematic design of the ExPAN set-up is shown in figure 2.8. The optical parametric oscillator unit (OPO, APE) was synchronously pumped by a modelocked Titan:Sapphire (Ti:Sa) ultra-fast laser head unit (Chameleon Ultra II, 680-1080 nm, 140 fs at peak, 80 MHz, >3.5 W, Coherent) which itself was pumped by a neodymium vanadate (Nd:YVO_4) laser (Verdi laser head unit in Chameleon Ultra II). The Chameleon output wavelength of 800 nm passed a half wave plate (WP1: AHWP05M-980, 690-1200 nm, Thorlabs) and a high energy broadband polarizing beam splitter (PBS1: PBS1005-SBB, 400-1100 nm, Precision Photonics), the combination of which was used to tune the laser power before it was reflected into the OPO. The ring version of the OPO first transformed the Ti:Sapphire output wavelength by a quasi phase matched interaction in the periodically poled crystal to an infrared (IR) Signal and an IR Idler wavelength. Then, the IR Signal wavelength was intracavity frequency doubled by a second harmonic generation (SHG) crystal made from lithium triborate (LiB_3O_5, LBO). The accessible output wavelength in the visible range ranged from 505 nm to 750 nm and was tuned to 568 nm for ExPAN measurements by optimizing the phase matching temperature of the SHG crystal and by adjusting the cavity length. The linearly polarized, pulsed excitation beam passed a filter (F1: Multiphoton emitter HC 770/SP, AHF) in order to separate the desired 568 nm wavelength from IR components. A pair of achromatic lenses (L1: AC254-075-A-ML, f = 75 mm, Thorlabs, L2: AC254-300-A-ML, f = 300 mm, Thorlabs) was used to expand the beam to a diameter of 6 mm. Mirrors and a dichroic beamsplitter[e] (D1: Laser beamsplitter z568sprdc, AHF) reflected the excitation beam into a polarizing beam splitter (PBS2: PTW 20, 440-650 nm, B. Halle Nachfl. GmbH) which was used on the one hand to improve the quality of the linear polarization of light and on the other hand to couple the excitation light with the perpendicular oriented de-excitation ExPAN beam. The ExPAN beam possessed a wavelength of 715 nm and was generated in a second Ti:Sa laser (Chameleon XR, 705-980 nm, >1.5 W, Coherent) operated in CW mode. The de-

---

[e] The dichroic beamsplitter D1 was used instead of a regular mirror because it allowed another beam to be coupled into the excitation beam path which was also regularly used but not for measurements presented in this thesis.

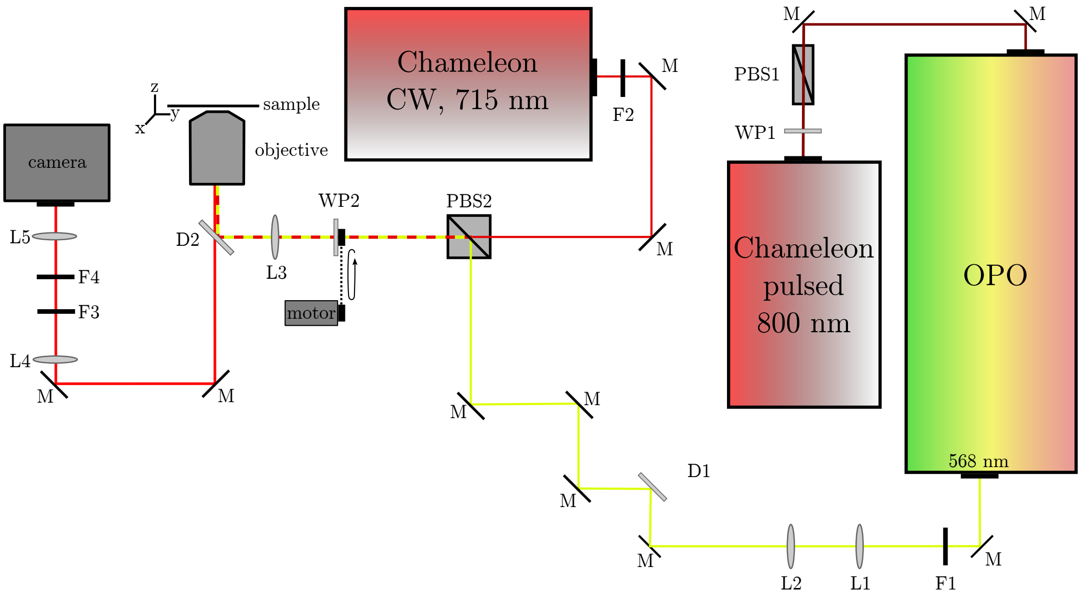

Figure 2.8: Schematic design of the ExPAN set-up showing set-up components and beam paths of the excitation beam (568 nm), the de-excitation beam (715 nm) and the emission light beam (650 nm). Optical parts are labelled as follows: D dichroic mirror, F filter, L lens, M mirror, OPO optical parametric oscillator, PBS polarizing beam splitter, WP wave plate.

excitation beam passed a longpass filter (F2: FEL0700, Thorlabs) in order to remove any IR or SHG components from the light before it was coupled with the excitation light in the polarizing beam splitter by the use of two mirrors. Behind the polarizing beam splitter, both beams passed an achromatic half wave plate (WP2, AHWP05M-600, 400-800 nm, Thorlabs) which was mounted into a chopper wheel (MC1F2, Thorlabs) and attached to a ball bearing. Using a rubber belt and an electric motor which was controlled by an optical chopper system (OCS: MC2000-FW-SP, Thorlabs), the chopper wheel and consequently the wave plate were constantly rotated during the measurements. An achromatic lens (L3: AC254-400-A-ML, f = 400 mm, Thorlabs) and a dichroic beamsplitter (D2: XF2045, Omega Optical) were used to focus and reflect the excitation beam onto the back aperture of the microscope objective (UPlanSApo 60XO, 60x, NA = 1.35, oil immersion, Olympus) which was mounted in an inverted microscope body (IX 71, Olympus). The sample was placed in a sample chamber on a motorized stage (Scan IM, Märzhäuser Wetzlar) that allowed sample scanning in the two lateral dimensions x and y. Fluorescence light was collected by the same objective and passed the dichroic mirror into a lightproof detection unit. Two mirrors and another pair of achromatic lenses (L4: AC254-040-A-ML, f = 40 mm, Thorlabs, L5: AC254-250-A-ML, f = 250 mm, Thorlabs) were used to further enlarge and direct the image onto the electron-multiplying charge-coupled device camera (EMCCD, iXonEM+897 back-illuminated, Andor Technology). As a result, the final image magnification was increased from 60-fold to 375-fold. Two filters (F3: long pass filter, FEL0600, Thorlabs, F4: band pass filter, 620/60 ET, AHF) were used to separate the fluorescence light wavelength from remaining excitation light or scattered light.

2.2.2 EMCCD Camera calibration

The EMCCD camera used possessed a detection unit consisting of 512 by 512 pixels, each of 16 x 16 µm^2 real size. Due to the fact that the overall magnification of the image was defined by the microscope objective's magnification in combination with the image enlargement resulting from the detection path lenses, a calibration of the effective pixel size was required. This was realized by using a scale micrometer in which a two-millimeter scale was divided into 200 parts, two consecutive lines thus referring to a spacing of 0.01 mm or 10 µm. For mapping the calibration pattern of the glass substrate to the EMCCD camera, the room light in the laser lab was turned on completely. A a consequence, the microscope objective collected parts of the surrounding illumination causing a large background signal on the EMCCD camera. After inserting the calibration slide into the motorized stage and bringing the scale into the focal plane of the microscope's objective, dark lines appeared in the field of view. 200 frames were recorded and used for calculating the effective pixel size and the overall magnification. By fitting a double Gaussian function to the plot profile of the cross section of the averaged image of transmitted intensity, center to center distances of (235.3 ± 0.4) pixel for x-direction and (235.5 ± 0.4) pixel for y-direction were determined. From these values, an effective pixel size of (42.5 ± 0.1) x (42.5 ± 0.1) nm^2 was calculated, resulting in an overall magnification factor of (376 ± 1).

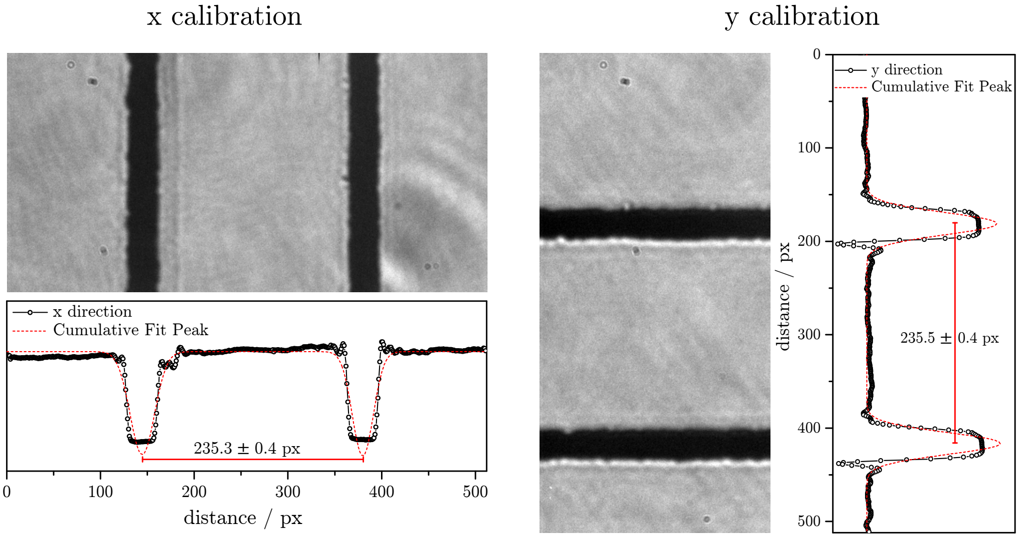

Figure 2.9: EMCCD camera calibration in x- and y-direction for single molecule measurement (2.2.1) and fringe pattern bleaching set-up (3.2.1). Transmission intensity images show an average from 200 individual frames in which the calibration lines were 10 µm apart.

2.2.3 Sample preparation

Microscopy cover slips made from borosilicate glass (hydrolytic class number 1, 0.13 - 0.16 mm thickness, Roth) were cleaned by ultra-sonication in methanol for 30 minutes. After blow-drying the glass surface with nitrogen gas, a droplet of 10 µL ATTO 590 free acid solution (Atto-Tec, dilution 10 nM in methanol) was placed in the center of the cover slip. After 10 minutes at room temperature, the solvent had completely evaporated and the sample was placed into a stage sample holder that was inserted into the motorized stage.

2.2.4 Measurement procedure

The free µManager software[73] was used to control the EMCCD camera, which was operated in frame transfer mode at 33.33 ms exposure time and an electron multiplying gain (EMG) of 300. As in most applications that rely on repetitive measuring cycles, it was crucial to map a full rotation of the polarization orientation of light (180°) to an integer number of imaging frames (e. g. 15 frames). In this manner, frames 1, 16, 31, and so on always related to the same orientation of the polarization. The synchronization of the polarization orientation to the imaging speed was accomplished by using an optical chopper system (OCS). Here, the external trigger signal from the camera was transmitted to the OCS controller which controlled the rotating motor speed. An optical switch was attached to the outer rim of the chopper wheel, which was fixed to the half wave plate, thereby directly controlling the rotation speed of the polarization orientation. The chopper blade interrupted the low-intensity LED light from the switch which was consequently able to monitor the chopping speed as the reference signal. By multiplying the external trigger signal (imaging speed: 30 frames per second) with a fixed factor of 5/3, the resulting reference signal corresponded to one full rotation of the polarization orientation of light (180°) per 15 frames or in other words 15 frames per period (fpp). The factor 5/3 can be explained as follows: The imaging speed equaled 30 frames per second (30 Hz). Desiring one full rotation of the polarization orientation of light (180°) per 15 frames meant that the two full rotations ($2\cdot 180° = 360°$) per 30 frames i. e. per second were required. Two full rotations of the polarization orientation of light (360°) corresponded to 180° rotation of the wave plate i. e. chopper blade per second. The chopper blade used contained 100 holes, so 180° rotation per second meant 50 chops per second (50 Hz). The internal multiplication factor was a direct consequence of this consideration ($50\,\text{Hz}/30\,\text{Hz} = 5/3$). Imaging one full period to 15 frames meant that one frame corresponded to an angle range of 12°. By increasing or decreasing the rotation speed of the OCS it was possible to map smaller or larger angle ranges to one frame, respectively.

During the measurements, 400 frames were recorded in total using rotation of the polarization orientation. The excitation light's illumination power was set to approximately 100 W/cm^2. Due to the fact that the OCS controller accelerated the rotating motor at the beginning of the measurements too fast and constant rotation was only achieved after approximately 50 frames, the high-intensity de-excitation beam path (between 1-3 MW/cm^2) was initially opened after 100 frames. This large power density was achieved by constricting the illumination size to a circular area of roughly 30 µm^2.

2.2.5 Absorbance and fluorescence spectra of ATTO 590

The absorbance and fluorescence emission spectra of ATTO 590 in methanol given in the theoretical section 2.1.5 were measured as follows: 1 mg ATTO 590 free carboxy acid were solved in 1 mL methanol solution. A 1:10 dilution thereof using methanol was inserted into the sample chamber of a quartz glass cuvette (SUPRASIL®, Hellma Analytics®). Absorbance spectra were recorded at 22 °C using a UV/VIS spectrophotometer (Lambda 25, Perkin Elmer®). The spectra recording speed was set to 2 nm per second for the wavelength range from 400 to 700 nm. Fluorescence emission and excitation spectra were recorded at 22 °C using a fluorescence spectrophotometer (Cary Eclipse, Varian®). For the emission spectrum, the excitation wavelength was set to 568 nm, scanning the fluorescence range from 570 to 750 nm with a resolution of 2 nm per second. The excitation slit was chosen to be 5 mm wide, the emission slit 2.5 mm. For the excitation spectrum, the detected emission wavelength was set to 624 nm while scanning the excitation from 400 to 700 nm with a resolution of 2 nm per second. Here, the opening widths for the excitation and emission slits were also set to 5 and 2.5 mm, respectively.

2.3 Results and discussion

In the first part of the evaluation, a qualitative presentation and discussion of regular fluorescence modulation in the single molecule regime are given. After explaining basic concepts of this technique for several chosen single molecule examples, fluorescence modulation with and without the influence of ExPAN are addressed from a quantitative perspective in which the enhancement factor (f_s) of ExPAN is determined. First qualitative hints for the separability of single molecule pairs at short distances according to their phase information are presented. In this section, resolution remains treated from a qualitative view since resolution quantification remains a central part in the discussion in the last chapter of this thesis (cf. Chapter 4).

2.3.1 Averaged fluorescence intensity images

Absorption and emission spectra of bulk solutions of fluorescence dyes contain much interesting information about the sample as a collective of many individuals. Measurements are usually carried out in the millimolar concentration range which is far above the single molecule regime. In order to observe the fluorescence response from individual fluorescence dyes, Avogadro's number had to be bypassed by distributing tiny volumes of an extremely diluted sample on a broad glass substrate. The fluorescence intensity image averaged over 60 individual frames showing the fluorescence response from single ATTO 590 molecules on glass substrate is presented in figure 2.10. During the measurement, the light's polarization plane was constantly rotated, which means that calculating the average intensity over a number of frames resembled the case of using unpolarized excitation light. Figure 2.10 revealed that some hundred fluorescence spots were heterogeneously distributed on the surface. It became evident that the brightness of individual spots differed from one to another. There are several explanations why the brightness might differ in the average intensity image. When looking at the molecular orientation of the fluorescent dye, molecules that were not lying exactly flat on the glass surface contributed less fluorescence intensity to the average due to the fact that their transition dipole moment was tilted away from the plane of the glass surface. Keeping in mind that the excitation's light polarization vector was in plane with the glass surface, tilting the molecule away from the glass meant an increase of the angle between the interacting vectors. Consequently, according to equation 2.5 the excitation's probability was diminished and less fluorescence was recorded. Additionally, the detection efficiency of the microscope's objective is decreased for photons emitted from a tilted molecule. Another explanation might be that fluorescent dyes photo-bleached during the measurement, thus contributing less intensity to the averaged image. The brightness inhomogeneity can also be caused by collisional quenching with molecular oxygen[74] since the dyes attached to

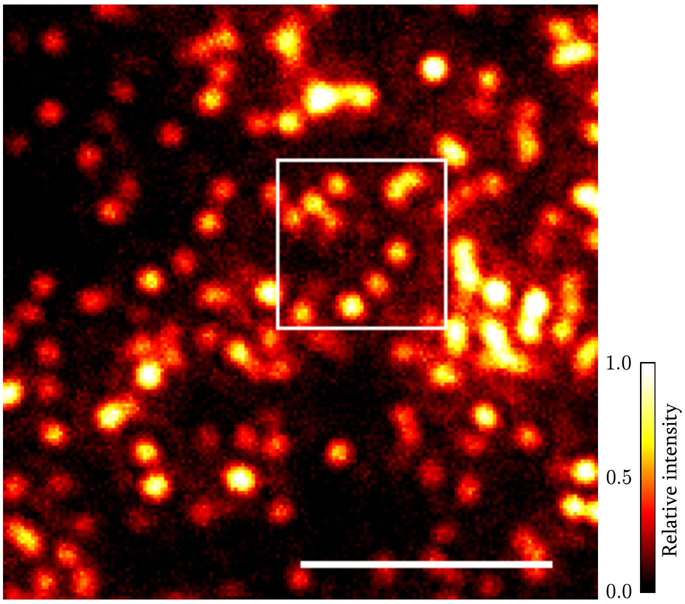

Figure 2.10: Fluorescence intensity image averaged over 60 individual frames showing single ATTO 590 molecules. (Scalebar 3 µm)

the surface are also in contact with air. Molecular oxygen in a triplet state is assumed to induce intersystem crossing of the fluorophore to the triplet state thus reducing the detected fluorescence. Even without the influence of triplet oxygen, discrete jumps in fluorescence intensity due to quantum jumps between electronic states have been shown to occur.[75][76][77]

Even though the real size of the radiating fluorescence source was on the nanometer scale, the distribution of observed fluorescence from a single dye was much larger due to diffraction. In theory, the signal distribution can be described by the Airy-disc function, whereas in experiments spots are frequently approximated by a two-dimensional Gaussian function. Based on these functions, single molecule localization techniques localize centers of fluorescence distributions assuming that the center of localized spots refer to the true position of the fluorescence dye. Many individual circular fluorescence spots can be identified within the average intensity image in figure 2.10 for which the position of the underlying dye could be evaluated by finding the spots center. Localization problems can arise when two or more molecules are in close proximity to one another i. e. when they meet the Rayleigh criterion (cf. Section 2.1.6) as some larger or elongated fluorescence spots in figure 2.10 indicate. In those cases, the fluorescence spots cannot be separated from one another unless additional tools or techniques are applied that help identifying the individual spots. As outlined in Chapter 4, super-resolution techniques based on localization succeed by controlling the population within fluorescent states of the molecules, thus temporally separating and individually localizing the signals. STED based techniques alter the PSF by using stimulated emission patterns. In the last part of this thesis (Chapter 4) it will also be assessed to what extent controlled fluorescence modulation can be used to distinguish and separate fluorescence signals beyond the diffraction limit of light.

2.3.2 Fluorescence modulation without ExPAN

The square-sized region of interest (ROI) in figure 2.10 is used to explain the effects of fluorescence modulation of single emitting dyes. Figure 2.11 shows 15 individual images each corresponding to a different orientation of the excitation light's polarization. Each image was assigned an angle α in which frame one was arbitrarily set to $\alpha = 0°$. As a consequence, given angles do not refer to absolute orientations of fluorescence dipole moments but are used qualitatively as a reference tool instead. Focusing on the circular ROI in figure 2.11, the fluorescence behavior of single fluorescence dyes became evident. Large amounts of fluorescence signal intensity were detected when the interaction of $\vec{E}$ and $\vec{\mu}$ allowed large excitation probability which was the case when the angle α between $\vec{E}$ and $\vec{\mu}$ was close to zero degrees (see image at angle 0°, figure 2.11). Almost no fluorescence was detected when the orientations were perpendicular to one another (see image at angle 96°, figure 2.11). On the basis that the excitation light's polarization plane was constantly rotated, the fluorescence signal from the single molecule was modulated with a fixed frequency which was defined by the experimental rotation speed of the excitation light's polarization.

The rectangular ROI in figure 2.11 illustrates an interesting pair of fluorescence spots. In

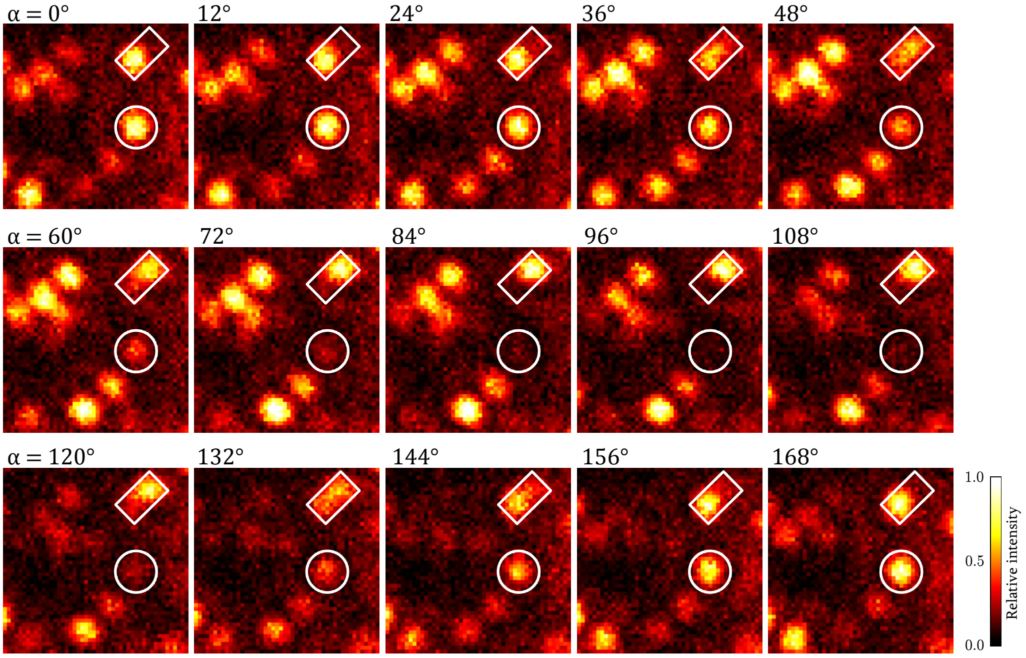

Figure 2.11: Orientation dependent fluorescence intensity images from the selected ROI in figure 2.10. One image corresponds to the average over four images with the same excitation polarization. The circular ROI emphasizes a single molecule of interest. The rectangular ROI sets a pair of molecules apart by their time delayed signal appearance.

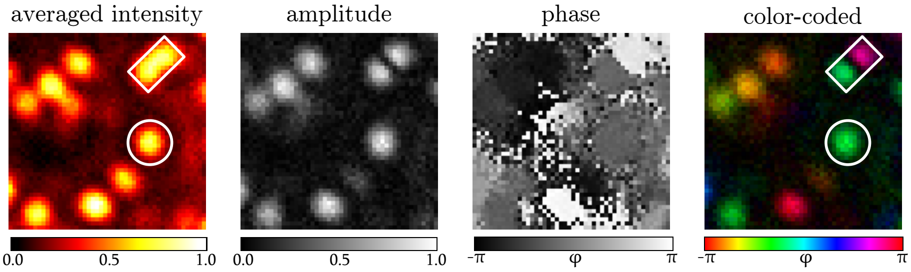

Figure 2.12: FFT output of periodic fluorescence modulated signals from the selected ROI in figure 2.10. From left to right: Averaged fluorescence intensity image, amplitude image, phase image, color-coded image in which phase and amplitude are depicted by color and intensity, respectively.

the average image, that intensity spot was rather shaped rod-like instead of circular thereby suggesting that the underlying fluorescence source can possibly be the result from more than one single emitting dye. By using modulation of the excitation light's polarization plane and looking at the angle dependent individual images, the origin of the rod-shaped average spot was explained. In this special example, two molecules in close proximity to one another clearly appeared separate from each other within different images i. e. their maximum fluorescence contribution appeared at distinct angles. The fluorescence spot on the bottom left of the rectangular ROI approximately peaked in image one ($\alpha = 0°$) while simultaneously the other spot was close to non-detectable. Vice versa, the second spot to the top right of the ROI showed its maximum signal contribution at $\alpha = 96°$. These values in relative terms meant that the molecules' transition dipole moments were approximately arranged perpendicular with respect to one another. In the average intensity image in figure 2.10, a cumulation of the separate fluorescence spots is visible only as a rod-shaped spot. Due to the fact that fluorescence signals were orientation dependent, generating fluorescence modulation proved to be a useful tool for separating signals. A periodic fluorescence signal can be characterized by its signal amplitude and the signal's phase which can be obtain by fast Fourier transform (FFT) methods. In every detection pixel, additional information besides fluorescence intensity is contained due the modulation of the fluorescence signal. Figure 2.12 shows the amplitude and phase for the same square excerpt from figures 2.10 and 2.11. The color-coded visualization combined the phase and amplitude information through color (phase) and brightness (amplitude). High-intensity spots in the amplitude or color-coded images referred to periodic fluorescence signals with large amplitudes, as was observed in the circular ROI. Small amplitudes indicate that the underlying periodic signal might be influenced or less pronounced. Some reasons that have been previously discussed, like photo-bleaching, collisional quenching,[74] a tilt of the molecular orientation, and quantum jumps between electronic states,[75][76][77] can be named as potential reasons why amplitudes differ from spot to spot.

One beneficial aspect of inducing fluorescence modulation was the possibility to enhance the amplitude value by recording an increasing number of signal periods. Similar as in lock-in-amplification approaches, signals of a known frequency or periodicity even with small amplitudes were successfully isolated from noise and enhanced. By looking at the signal amplitude, the interesting pair of fluorescence spots in the rectangular ROI in figure 2.12 was separated. In the center of the rod-shaped averaged intensity spot, a node appeared. As previously assumed, the rod-shape resulted from two individual dyes in close proximity to one another. Each emitters would show a squared cosine fluorescence traces with a corresponding phase φ. If the phases of the individual signals were equal, they would sum up to a periodic trace with increased amplitude and equal color in both spots in the color-coded image. If the difference in phase exactly correlated with one half of the period length, the periodic signal in the center of the rod-shape would show an amplitude of zero and both spots would show different colors in the color-coded image. It became evident that the latter case applied to the assumed molecule pair in figure 2.12 with an estimated phase difference of $\Delta\varphi \approx 90°$. A prerequisite for signal separation was of course the existence of sufficient difference in orientation. For regular modulated signals with cosine-squared based function, summing always resulted in cosine-squared signals for which only one phase and one amplitude coefficient was obtained. With increasing numbers of single emitters or lack of sufficient difference in orientation, identification of individual fluorescence sources becomes more and more complicated.

2.3.3 Time-dependent fluorescent traces with and without ExPAN

Up to this point, qualitative statements about fluorescence modulation from single molecule emitters have been presented by looking at average intensity or orientation dependent images. Focusing on the circular ROI in figure 2.11, a quantitative time-dependent fluorescence trace was derived by averaging the signal intensities of pixels within the ROI. By plotting these average intensity values against frame number, a periodic fluorescence modulation curve was obtained as shown in figure 2.13. The signal intensity alternated between a maximum intensity level (~ 200 a.u.) and no fluorescence ($\sim$ 120 a.u.) with a signal period of 15 frames. Fitting a squared cosine function from equation 2.18 to the data points revealed a good accordance with the experimental data trace.

$$I_{\text{fl}}(o) = A_1 + A_2 \cos^2(A_3(o - A_4)) \tag{2.18}$$

Herein, A_1, A_2, A_3, and A_4 are constants describing the offset, amplitude, periodicity, and phase delay of the squared cosine function. The variable o is the general expression for the chosen abscissa which can be the time t, the frame number F, or the angle

α. By averaging values from frames that belong to the same net polarization orientations (e. g. $1, 16, 31, 46, ...$), the signal-to-noise ratio (SNR) was increased. Normalizing the phase averaged data and plotting the values against angular coordinates resulted in a polar plot that represented a two-dimensional cross-section of the three-dimensional excited-state photo-selection dumbbell. Again, angles were arbitrarily related to frame numbers. The polar plot neatly illustrated that the transition dipole moment of a single fluorescence dye did not need to be oriented exactly parallel to the excitation light's polarization vector in order to obtain excitation and consequently fluorescence. As expected from equation 2.6 in section 2.1.3, even at 45° deviation from the perfect alignment the excitation's probability was still present half as much with respect to the maximum value. Looking back at the pair of fluorescence dyes in close proximity to one another with an orientation difference of roughly 90°, this broad range of excitation would impede signal separation in cases in which the difference of orientation would not suffice in separating the individual signals from the cumulative count. This hindrance was addressed by making the photo-selection more specific by narrowing the angle range for excitation (ExPAN).

A second, de-excitation beam, whose linear polarization plane was oriented perpendicular to the excitation's light polarization, was applied to the sample inducing stimulated emission. On the one hand, the maximum photo-selection of stimulated emission appeared parallel to the illumination's light minimum excitation which meant that stimulated emission barely occurred due to the fact that only a small number of photons populated the first electronically excited state in the first place. On the other hand, the minimum photo-selection of stimulated emission appeared parallel to the illumination's light maximum excitation which meant that the maximum fluorescence remained close to unharmed. However, the true power of this approach became clear when looking at intermediate angles i. e. between maximum excitation and maximum stimulated emission. By

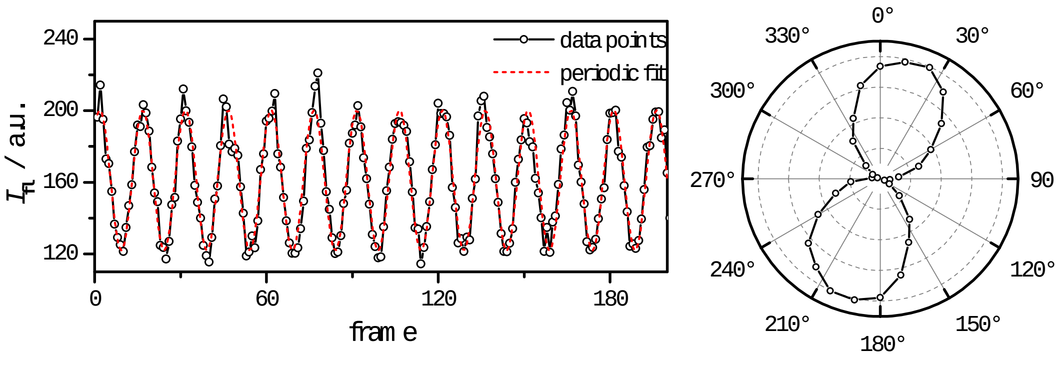

Figure 2.13: The fluorescence trace to the left corresponds to the averaged fluorescence intensity from the circular ROI in figure 2.11 plotted against the frame number. The corresponding representation in polar coordinates is given to the right. In this case, the first frame was arbitrarily set to $\alpha = 0°$.

neglecting all effects that lead to a depopulation of the first excited state (e. g. intersystem crossing and internal conversion among others) except fluorescence and stimulated emission, transition probabilities and the orientations of the photo-selection dumbbell determine whether photons return to the electronical ground state by the processes mentioned. Due to the fact that transition probabilities are proportional to the dot product of the polarization's vector and the transition dipole moment's vector, by increasing the intensity of the stimulated emission beam only and by assuming the transition dipole moment vectors of stimulated and spontaneous emission to be collinear, the probability for stimulated emission was increased. Since the orientations of photo-selection dumbbells were 90° apart, the process of fluorescence was increasingly replaced by stimulated emission with increasing mismatch between the transition dipole moment's vector and the excitation light's polarization plane. Figure 2.14 shows a time-dependent fluorescence trace from a single ATTO 590 dye on glass while the second de-excitation beam was applied. It became clear that the signal maxima appeared with a periodicity of 15 frames and that each peak width was substantially narrowed in comparision to regular fluorescence trace data without ExPAN (cf. figure 2.13). Fitting a ExPAN based function on basis of equation 2.13 to the data points revealed a good accordance with the experimental data trace.

$$I_{\mathrm{fl}}(o) = A_1 + A_2 \frac{\cos^2(A_3(o - A_4))}{1 + f_s \sin^2(A_3(o - A_4))} \tag{2.19}$$

Herein, A_1, A_2, A_3, and A_4 are constants describing the offset, amplitude, periodicity, and phase delay of the ExPAN function while the f_s equals the ExPAN factor. Again, the variable o is the general expression for the chosen abscissa which can be the time t, the frame number F, or the angle α. By using equation 2.19 for nonlinear curve fitting, an ExPAN factor of $f_s = (11 \pm 2)$ was obtained which characterized the ratio between the rate constants of stimulated and spontaneous emission (cf. section 2.1.4).

In order to compare the effect of ExPAN with regular fluorescence modulation, the ExPAN based modulation data was plotted against angular coordinates in the photo-selection dumbbells with ExPAN. Again, angles were arbitrarily related to frame numbers and SNR was increased by averaging values from frames that belonged to the same net polarization orientations (e. g. $1, 16, 31, 46, ...$). The resulting polar plot in figure 2.14 represent the two-dimensional cross-section of the three-dimensional excited-state photo-selection dumbbell under the influence of the stimulated emission beam. Black dots and lines refer to data points, red-dashed lines represents the nonlinear curve fit according to equation 2.19 and blue-dashed lines stand for the theoretical cosine-squared distribution without stimulated emission according to equation 2.18. The polar plot convincingly illustrates that the photo-selection dumbbell was substantially narrowed when ExPAN was applied. At $\alpha = 45°$ fluorescence dropped from a value of 0.5 a.u. for excitation without stimulated emission to below 0.1 a.u. for excitation with stimulated emission. Figure 2.15 shows a fluorescence intensity image averaging 350 individual frames while ExPAN was being applied, along with its corresponding color-coded phase image. The circular ROIs emphasize three interesting fluorescence spots whose time-dependent fluorescence intensity traces are shown to the right. ROIs 1 and 3 exhibited periodic peaks that were substantially narrowed during the entire range of measurement of approximately 12 s. The ExPAN factors obtained from nonlinear curve fitting for these two traces were $f_s = (4.8 \pm 0.5)$ and $f_s = (4.0 \pm 0.4)$ for ROIs 1 and 3, respectively. The difference between the values can be a consequence of the beam profile of the stimulated emission beam within the focal plane. The effective size of the ExPAN beam within the sample had a diameter of approximately 6 µm whose intensity distribution is best assumed to be a Gaussian profile. This means that single emitters which are located exactly in the center of the ExPAN area are exposed to slightly more stimulated emission intensity (I_{se}) than compared to molecules at the outer rim of the effective ExPAN beam. The larger I_{se}, the larger f_s gets, the narrower the peaks become. ROI 2 also revealed an interesting ExPAN fluorescence trace since it was interrupted between frames 150 and 225. During this period of time, the single emitter populated a non-fluorescent, dark state.[45] As a consequence, in addition to the reduced brightness in the fluorescence intensity average image, the amplitude depicted by brightness in the color-coded phase image was likewise lessened. Comparably to the pair of single molecules separated by phase and amplitude information in figure 2.12, the arrow in figure 2.15 points at a similar interesting area. In the averaged fluorescence intensity image, a rod-shaped spot was identified alike. Only the color-coded phase image revealed the underlying individual signals by the phase difference of approximately 72° in combination with the characteristic node in-between. This further indicates that differences in molecular orientation of individual emitters can be

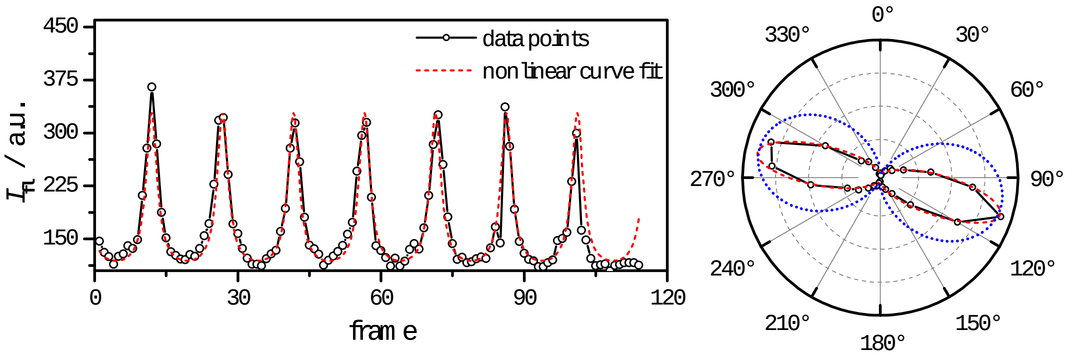

Figure 2.14: The fluorescence trace to the left corresponds to the average fluorescence intensity from a single ATTO 590 molecule while ExPAN was being applied. The corresponding representation in polar coordinates is given to the right. In this case, the first frame was arbitrarily set to be $\alpha = 0°$. Equation 2.19 was used for nonlinear curve fitting (red curves) and equation 2.18 was used to calculate the theoretical cosine squared-distribution (blue curve).

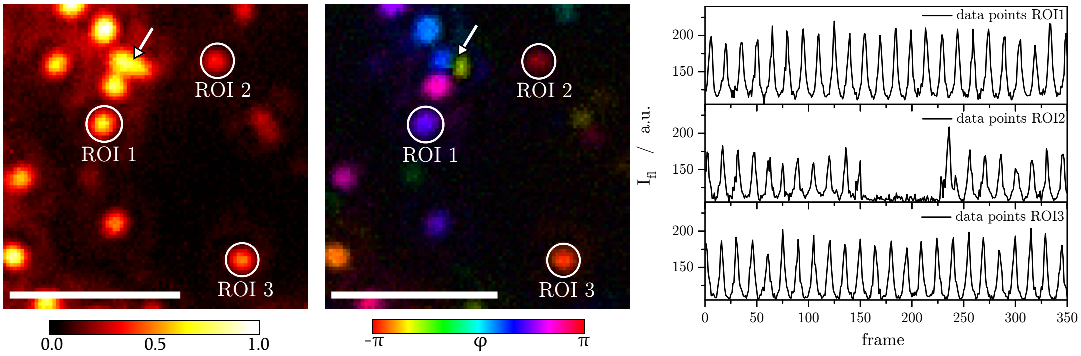

Figure 2.15: The fluorescence image to the left corresponds to the average over 350 individual frames. The color-coded phase image represents phase and amplitude as color and intensity, respectively as obtained from FFT. Fluorescence signal traces to the right were derived from the circular ROIs. The arrow points at a pair of dyes which are only separated in the phase-amplitude image. (Scale bar 2 µm)

exploited under ExPAN conditions as well as without in order to temporally separate individual signals from each other.

In theory, the ExPAN factor can be increased infinitely resulting in infinitesimal narrow peaks with very precise and definite signal phases. However, experimental limits stem on the one hand from set-up parameters e. g. maximum laser output power. On the other hand, certain effects of photo-physics were preferably induced by increasing power density. Reversibly entering dark states or irreversible photo-bleaching were regularly observed during measurements, which stood in direct relation to the stimulated emission beam power used. Even though ExPAN was achieved by using stimulated emission its underlying physical principle can be considered more general. It is expected that other controllable de-excitation paths could potentially lead to similar narrowing of the polarization angle range of excitation. Photo-switchable or photo-activatable fluorophores may be named among the most promising dyes for inducing ExPAN by processes other than stimulated emission.

3 Interference lithography set-up design and characterization

Introducing a spatial modification to the illumination pattern in the focal plane of the objective has been achieved by various methods for different applications. Among the first applications with respect to fluorescence microscopy (1978), a periodic pattern of parallel stripes[78] in the focal plane was used to determine diffusion coefficients of fluorescent phospholipid probes in membrane like structures by observing fluorescence recovery after photobleaching (FRAP).[79][80][81] Herein, the periodic pattern was obtained by inserting a Ronchi ruling into the excitation path. Only a few years later (1982), the sinusoidal intensity profile in the focal plane was created by using two beam interference which is then called fringe pattern.[82] Even though fringe patterned bleaching was mainly used for cell surface investigation by FRAP for many years to come,[83][84] the importance of creating illumination patterns quickly grew when structured illumination was shown to improve the axial resolution of fluorescence microscopes in the 1990s.[85][86][87] Soon, lateral resolution improvement was also demonstrated by using structured illumination.[88][89][90][91][92][93] From these developments it was not far until simultaneous resolution improvement in axial and lateral direction was obtained by means of structured illumination resulting in enhancement in three-dimensions.[94][95]

In the course of this thesis, a set-up was developed creating a fringe pattern in the focal plane of a regular wide-field fluorescence microscope in epi configuration. This set-up is intended to be used for the purpose of interference lithography by bleaching a fringe pattern into a self-built fluorescent photoresist. In contrast to any other interference technique implemented in a fluorescence microscope known so far, beam separation was accomplished by the use of two Wollaston prisms inserted in the excitation light's beam path. Two beams were reflected into the microscope's objective and interfered in the front focal plane. First, this chapter provides a short summary of common techniques used for creating fringe patterns in microscopy set-ups. Then, the theoretical background of two beam interference and Wollaston prisms is briefly outlined. The focus of the results section rests upon the characterization of the designed lithography set-up with respect to the resulting fringe pattern observed in the fluorescence intensity image. Herein, the distance d_{obj} between the separated beams and the position expressed in angular units β_{obj} at the back focal plane are monitored in dependency of both rotation mounts' orientations (ω_1, ω_2) which contain one Wollaston prism each. This information is furthermore related to the orientation of the final fringe pattern β and the fringe periodicity p. In the final stage of this chapter, the knowledge gained by set-up characterization is used to find settings for the interference lithography measurements. Herein, the fringe pattern is applied to a self-built photoresist which consists of a densely packed layer of fluorescence molecules on glass substrate. Due to the very high illumination intensities, all dyes that are not located in or very close to the nodal lines subsequently photo-bleach. The negative image composed of the remaining lines of fluorescent dyes are subject to characterization by fluorescence modulation with and without ExPAN in the last chapter of this thesis (Chapter 4).

3.1 Theoretical background

3.1.1 Methods for creating structured illumination

Influencing the illumination pattern within a fluorescence microscope has been achieved in confocal systems[96][97][98] as well as in wide-field set-ups. Confocal systems are characterized by spatially filtering the fluorescence light prior to detection e. g. by inserting a pinhole confocal to the excitation focus.[99] For wide-field set-ups, two fundamentally different approaches to creating structured illumination have been reported in literature. The first group of techniques relies on inserting an illumination mask into the excitation light's beam path which defines the illumination pattern that is projected onto the sample plane. Diffraction gratings,[89][90][91] digital mirrors,[100][101][102] spatial light modulators,[103][104][105] and liquid crystal on silicon reflectors[106][107] have successfully introduced spatial modulation in wide-field set-ups. The second group of techniques generates structured illumination patterns by beam interference in which the coherent light source is separated by means of beam splitters.

An axially structured illumination pattern can be obtained by interference from two opposing objectives[85][86][108] or by back reflecting the light coming from the objective by a mirror.[85][109][110] A laterally structured illumination pattern is accessible by letting the beams interfere through the same objective or by causing beam intersection in the focal plane without the objective e. g. by a prism.[92] Beam separation for the second category type structured illumination has been accomplished by single polarizing beam splitters[111] and by an interferometer type set-up e. g. in Mach-Zehnder configuration.[112][113][114] Diffraction elements of the first category also introduce interference but they use higher diffraction orders and avoid the zero order diffraction beam which stems from non-diffracted light. The latter is most often blocked by a beam stop in the excitation light path.[115]

In many structured illumination techniques, different orientations of the fringe pattern needs to be applied to the sample in order to extend the resolution of the image.[116] This can either be accomplished by rotating and translating the illumination mask in well-defined intervals,[89][116] by translating the sample in a fixed pattern,[90] or by changing the relative phases of the interfering beam paths.[92][109][111] The challenge of the latter case is to design beam paths whose relative lengths are stable to sub-wavelength precision. The element causing structured illumination in the front focal plane of the objective is required to be easily capable of providing these different orientations of the fringe pattern.

In the course of this thesis, the challenge of beam separation was addressed by means of inserting two Wollaston prisms whose operation principle is outlined in section 3.1.3. Wollaston prisms have been successfully implemented in birefringent Fourier transform spectroscopy set-ups[117] and are considered advantageous with respect to stability because of the common path geometry.[118] A stack of two Wollaston prisms is intended to separate an initial beam into four beams from which two beams are reflected into the microscope objective where they can interfere in the focal plane. The following section will outline the general fundamentals of two beam interference and its applicability in microscopy.

3.1.2 Two beam interference

In the first chapter of this thesis, the concept of diffraction has been introduced for circular apertures. Diffraction can also be observed when a plane wave passes a very small single slit.[1] The initially planar wavefront is diffracted into a radial wavefront, thus when observing the intensity profile some distance away from the slit, the distribution is much broader than expected. If a planar wavefront passes a double slit (two slits which are separated by a distance l) at each slit the wavefront is diffracted.[2] The final intensity pattern shows a pattern of regularly distributed maxima and minima. This phenomenon is called interference which means that waves can either interfere constructively (maxima) or destructively (minima). Double-slit experiments have been successfully demonstrated using light waves but have also been repeated for electrons, protons, neutrons, atoms, and fullerene.[119] These findings corroborated the wave-particle duality which states that matter behaves as waves while waves also possess features usually assigned to particles.

Interference also occurs when two plane waves intersect at an angle.[120][121] A straightforward way of describing two beam interference is by considering the definition of a single wave which is given in equation 3.1 and can be expressed as a trigonometric function as well as in complex expression.

$$\vec{E}(\vec{r},t) = \vec{A}\cos(\omega t - \vec{k}\cdot\vec{r}) = \vec{A}\exp[i(\omega t - \vec{k}\cdot\vec{r})] \tag{3.1}$$

Herein, the electric field component of the linearly polarized light $\vec{E}(\vec{r},t)$ propagates with an amplitude component $\vec{A}$ at an angular frequency $\omega = 2\pi\nu$ in the direction of propagation. The wave vector $\vec{k}$ points into the propagation direction and its magnitude is the wave number $k = 2\pi/\lambda$. $\vec{A}$ is composed of an amplitude value E_0 in the direction of the unity vector $\vec{e}$ for linearly polarized light. The interference between two plane waves is best considered under conditions in which both beams possess equal intensities, polarization, and frequency. The wave vectors $\vec{k}_1$ and $\vec{k}_2$ are contained in the x,z-plane with angles ϕ_1 and ϕ_2 with respect to the z-axis as shown in figure 3.1. By expressing the wave vector $\vec{k}_1$ for the first wave in three dimensions and calculating the dot product $\vec{k}_1 \cdot \vec{r}$ as shown in equation 3.2, the wave can be expressed in Cartesian coordinates.

$$\vec{k}_1 \cdot \vec{r} = \begin{pmatrix} k\sin(\phi_1) \\ 0 \\ k\cos(\phi_1) \end{pmatrix} \cdot \begin{pmatrix} x \\ y \\ z \end{pmatrix} = k(x\sin(\phi_1) + z\cos(\phi_1)) \tag{3.2}$$

Likewise, the dot product of the second wave can be calculated. In summary, equation 3.1 can be rewritten as equation 3.3 which accounts for the complex expression of each plane wave in Cartesian coordinates.

$$\vec{E}_n(x,y,z,t) = \vec{A}\exp[i(\omega t - kz\cos(\phi_n) - kx\sin(\phi_n)] \tag{3.3}$$

The general field intensity of interference is equal to the time average of the modulus squared of the sum of all field components, as seen in equation 3.4 for two given waves.

$$I(x,y,z,t) = \langle|\vec{E}_1(x,y,z,t) + \vec{E}_2(x,y,z,t)|^2\rangle \tag{3.4}$$

Herein, $\langle\ \rangle$ refers to the time average which is required to be much longer than the wavelength since the magnitude of $\vec{E}$ alternates in length.[120] If it is considered that the point of intersection is at $z = 0$, the resulting intensity will be given in equation 3.5.

$$I(x,y) = I_0\,(1 + \cos\left[kx(\sin(\phi_1) - \sin(\phi_2)\right]) \tag{3.5}$$

Herein, I_0 equals twice the intensity of each individual wave ($I_0 = 2I_1 = 2I_2$) which can also be expressed by the magnitude of the amplitude vector ($I_0 = 2|\vec{A}_1|^2 = 2|\vec{A}_2|^2$). From equation 3.5 is becomes apparent that the intensity pattern extends into x-direction with the periodicity p given in equation 3.6.

$$p = \frac{2\pi}{k(\sin(\phi_1) - \sin(\phi_2)} = \frac{\lambda}{\sin(\phi_1) - \sin(\phi_2)} \tag{3.6}$$

A very simple case can be constructed from this equation. If the Cartesian coordinate system is rotated such that the z-direction forms the bisecting line between $\vec{k}_1$ and $\vec{k}_2$ being the propagation directions of the two interfering waves, the angles ϕ_1 and ϕ_2 can be expressed as the same angle with opposite signs ($\phi_1 = \phi$, $\phi_2 = -\phi$). The periodicity is then given as:

$$p = \frac{\lambda}{\sin(\phi) - \sin(-\phi)} = \frac{\lambda}{2\sin(\phi)} \tag{3.7}$$

It becomes apparent that the periodicity scales linearly with the wavelength λ and that for increasing angles ϕ in the range from 0° to <90° smaller periodicities result.

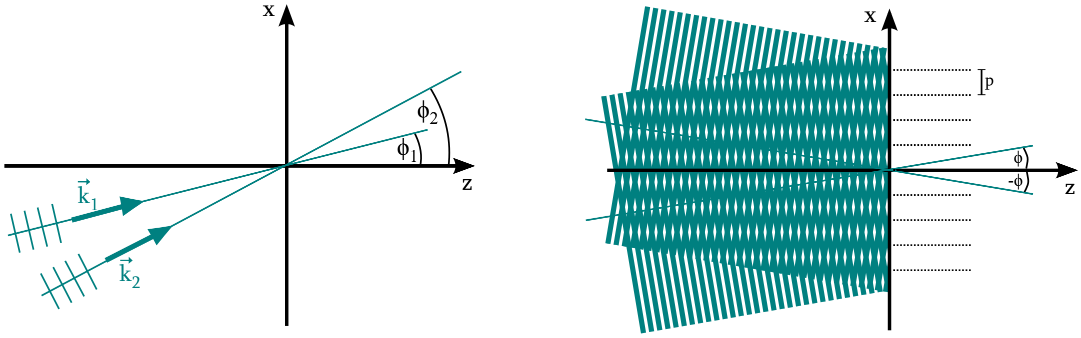

Figure 3.1: Schematic fringe pattern creation by beam interference of two monochromatic plane waves with propagation vectors $\vec{k}_1$ and $\vec{k}_2$ contained in the x,z plane intersecting at $z = 0$. The Cartesian coordinate system to the left is used to derive the general field intensity of the interference pattern (equation 3.5). The Cartesian coordinate system to the right is used to derive the general expression for fringe periodicity (equation 3.7).

According to Abbe's sine condition (cf. section 2.1.6), if an incoming beam enters the microscope's objective parallel to its optical axis but off-axis i. e. a certain distance r_d away from the center of the aperture, the out-coming beam will propagate with a certain angle ϕ with respect to the optical axis. Abbe's considerations stated that the sine of that angle is proportional to the radial distance ($\sin(\phi) \propto r_d$). For a simple lens, the proportionality factor is given by the focal length. For a microscope objective, the exact description of the beam path is much more complicated but high-numerical aperture objectives have been shown fulfill Abbe's sine condition by the considering the effective focal length.[122][123] If two beams are used to enter the objective at a certain distance to each other (d_{obj}), the beam paths will interfere in the focal plane of the objective. Due to the fact that the fringe periodicity as given by equation 3.7 depends on the angle between the interfering beams which in turn depends on the lateral displacement at the back focal plane of the objective, the fringe periodicity can be expressed as equation 3.8.

$$p \propto \frac{\lambda}{2r_d} = \frac{\lambda}{d_{\text{obj}}} \tag{3.8}$$

Herein, r_d is the off-axis distance to the center of the objective's axis and d_{obj} is taken to be twice the radial distance for the general case that both beams enter the objective symmetrically around its center. The fringe periodicity is expected to be proportional to the inverse of the spot distance. Now that the fundamentals of two-beam interference have been explained along with the intention to apply it in a fluorescence imaging microscope, the following section will explain how the excitation light is separated by means of a Wollaston prism.

3.1.3 Wollaston prims

A Wollaston prism is composed of two triangular birefringent wedges of quartz or calcite. Both wedges are cemented together so that their optical axes are oriented perpendicular with respect to one another.[124] A schematic picture of a Wollaston prism is given in figure 3.2. As can be seen, a beam of light is split into two components diverging at equal opposite angles with respect to the normal of the exiting plane possessing opposite polarization planes. Birefringent material possess a refractive index (n_r) that depends on the initial polarization plane and the propagation direction of light.[1][120] This means that different polarization orientations pass a birefringent medium at different phase velocities ($\upsilon = c/n_r$). After entering the first wedge normal to the surface, the beam continues along its initial propagation direction while different polarization components travel at different phase velocities. At the intersection with the second wedge, the slow component now turns into the fast component due to the fact that the optical axis of the second wedges is oriented perpendicular to the first. Whenever a difference in phase velocity exists between two media or in other words different effective refractive indices occur, light is refracted[125] at the surface according to Snell's law.

$$\frac{\sin(\phi_1)}{\sin(\phi_2)} = \frac{n_{r,2}}{n_{r,1}} = \frac{\upsilon_1}{\upsilon_2} \tag{3.9}$$

Herein, ϕ is the angle of the beam towards the normal of the interface plane, n_r is the refractive index, and υ is the phase velocity in the equivalent media 1 or 2. In the example illustrated in figure 3.2, the refractive index of the second medium is larger than the refractive index of the first ($n_{r,2} > n_{r,1}$). According to Snell's law, the phase velocity is larger in the first media compared to the second ($\upsilon_1 > \upsilon_2$). In one case of the Wollaston prism, the beam refracts away from the normal of the intersecting plane for the slow component (larger n_r) turning into the faster component (smaller n_r). In the other case, turning from

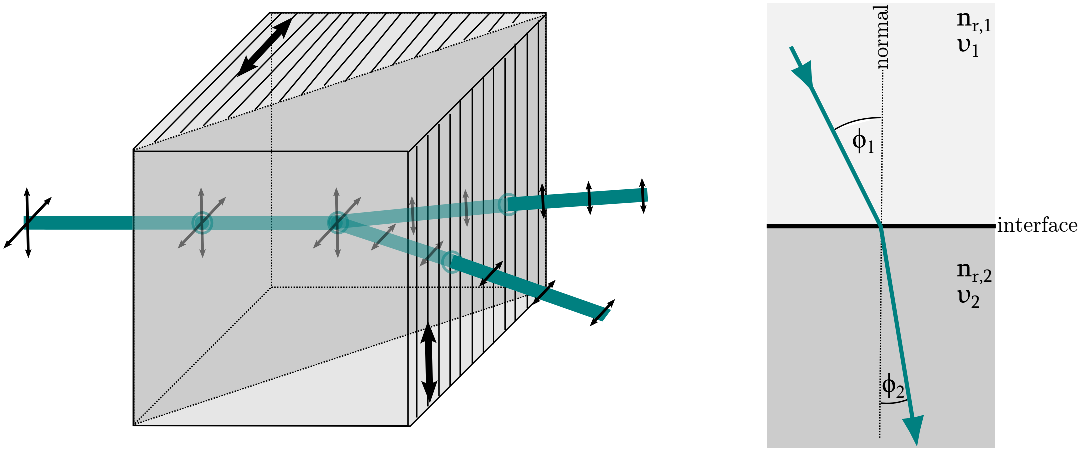

Figure 3.2: To the left, beam separation in a Wollaston prism is illustrated. Bold arrows indicate the fast axes of each triangular wegde. For details, see text. To the right, an incoming beam with an angle ϕ_1 towards the normal of the interface is refracted towards the interface's normal if the index of refraction of the second medium is larger than the first's ($n_{r,2} > n_{r,1}$, cf. equation 3.9).

fast to slow (small n_r to large n_r) causes the beam to refract towards the normal of the intersecting plane. Thus, both beams are spatially separated and exit the second wedge with a certain beam separation angle.[1]

3.2 Experimental section - Material and methods

The following experimental section will provide a detailed set-up description of the self-built fluorescence microscope set-up for interference lithography. In contrast to other techniques for creating a structured illumination pattern, the fringe pattern was obtained by beam separation using two Wollaston prisms. The sample preparation method is given along with a description of the measurement's procedure. The bleaching procedure is described for obtaining individual lines of fluorescence dyes by applying the fringe pattern with high-intensities on a densely packed layer of fluorescent dyes on glass substrate.

3.2.1 Set-up details

A schematic design of the fringe pattern set-up is shown in figure 3.3. As one can see, the beam paths of the excitation beam and the emission beam were quite similar to the ones presented in section 2.2.1. Only four changes need explanation and attention, one very important one and three of minor importance. The minor modifications addressed the de-excitation path, the excitation wavelength, and the detection path. Concerning the first, no ExPAN based de-excitation was used for creating the fringe pattern, consequently this beam path was left out of consideration. Concerning the excitation wavelength, the laser pulses from the Ti:Sa laser were likewise coupled into the OPO. In contrast to the previous use however, the ring version of the OPO was tuned to 594 nm output wavelength. This excitation light closely coincided with the maximum absorption wavelength of ATTO 590 and was used to create the fringe pattern in the focal plane of the objective using moderate illumination intensities. Concerning the detection path, the filter set of that day (F2: FEL0600, Thorlabs, F3: BP 650/40, Thorlabs, F4: BP 600/40, Thorlabs) and the dichroic beamsplitter in use (D2: dualband beamsplitter zt488/594 rpc, AHF) were not changed to the best filter set possible, as used in section 2.2.1 and figure 2.8. Even though it is expected that more leakage might occur onto the EMCCD camera using this set of filters with the excitation wavelength of 594 nm, it will not have an effect on the desired characteristics of interest, namely the fringe periodicity p and the fringe line orientation β.

The crutial set-up modification is emphasized by the rectangular box in figure 3.3 along with its enlarged inset, that offers the corresponding three dimensional view of the beam path. In front of the polarizing beam splitter, two Wollaston prisms (W1, W2: SiO_2, 1° beam separation angle, Linos Photonics) were inserted into the path of the excitation light beam. Both prisms were mounted into separate rotation mounts which allowed 360° continuous rotation by hand. The first Wollaston prism split the incoming vertically polarized light into two beams whose intensity, position, and polarization depended on the orien-

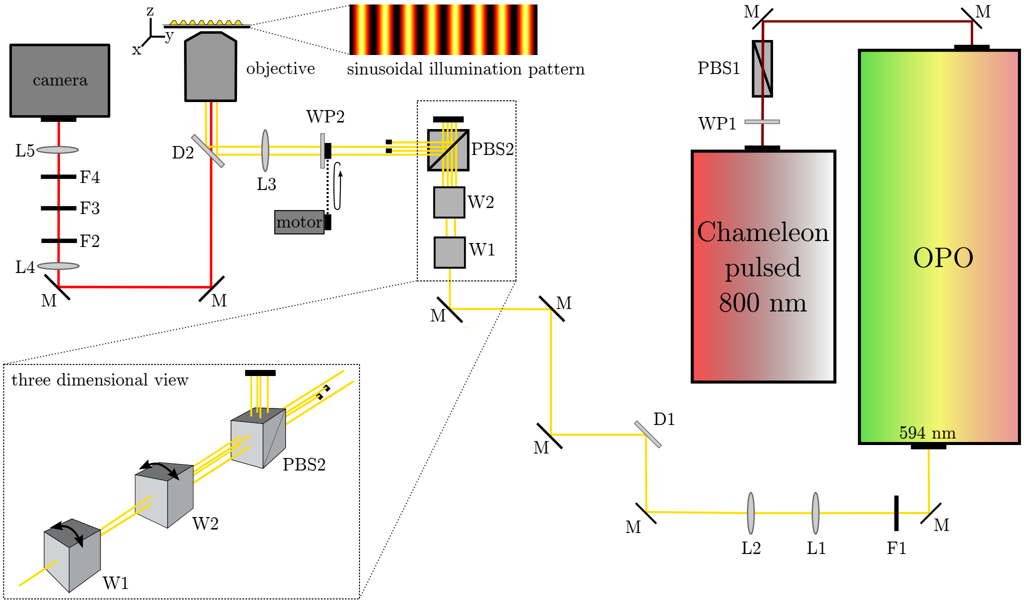

Figure 3.3: Schematic design of the fringe pattern bleaching set-up showing set-up components and beam paths of the excitation beam (594 nm) and the emission light beam (650 nm). Optical parts are labelled as follows: D dichroic mirror, F filter, L lens, M mirror, OPO optical parametric oscillator, PBS polarizing beam splitter, W wollaston prism, WP wave plate.

tation of the mount. The second Wollaston prism split each of the two incoming beams into two thus resulting in a total of four beams whose intensity, position, and polarization depended on the orientation of both mounts. Due to the beam separation angles of the Wollaston prisms, the beam propagation vectors diverged slightly and all succeeding optics were hit centrally symmetric. All four beams entered the polarizing beam splitter and are separated according to their parallel and vertical components of linearly polarized light. While parallel components are transmitted onto a beam block, vertical components are reflected into the orientation of the objective. Due to the fact that beam interference in the front focal plane was only conducted with two beams, two of the four beams are blocked after the polarizing beam splitter while both unblocked beams passed an achromatic half wave plate which was constantly rotated in the same manner as described in section 2.2.1. Since both beams possessed identical polarization orientation, the interference with the same half wave plate resulted in a synchronous rotation of the polarization planes of both excitation light beams. A lens was used to focus the beams onto the back focal plane of the objective with a final estimated distance of approximately 2.1 mm. The beams interfered in the front focal plane of the objective resulting in a sinusoidal illumination pattern when using moderate light intensities. Lines of maximum intensity result from constructive interference between the two beams. Lines of destructive interference possessed minimum intensity close to zero and are referred to as nodal lines throughout this thesis.

3.2.2 Sample preparation

Microscopy cover slips made from borosilicate glass (hydrolytic class number 1, 0.13 - 0.16 mm thickness, Roth) were cleaned by ultra-sonication in methanol (methanol) for 10 minutes. After blow-drying the glass surface with nitrogen gas, a droplet of 10 µL ATTO 590 free acid solution (Atto-Tec, dilution 10 µM in methanol) was placed in the center of the cover slip. The concentration was thousandfold larger than in comparison to the single molecule surface preparation procedure in order to create a completely packed fluorescent dye layer at the glass surface. After solvent evaporation, the sample was placed in the focal plane of the fringe pattern bleaching set-up (figure 3.3, sec. 3.2.1) via a stage sample holder in the motorized stage.

3.2.3 Measuring procedure

In order to measure the dependency of beam position, beam polarization, and beam intensity on the orientation of two Wollaston prisms each installed into a rotation mount, measurements were first conducted using the single Wollaston prisms. After inserting the first Wollaston prism into its rotation mount and into the beam path with vertically polarized light, the separated beams were visualized by diaphragm in front of the polarizing beam splitter. The Wollaston prism was rotated incrementally and put to hold at angles of orientation (ω) in which one of the peaks disappeared (no intensity) and in which both peaks were of equal intensities. For the first Wollaston prism this was the case at $\omega_1 = 44°, 89°, 134°, 179°, 224°, 269°, 314°$, and $359°$. For each ω_1, the polarization orientation (θ) was measured using a polarizing filter. The characterization was rounded up by drawing the position (X/Y) of the separated beams into a Cartesian coordinate system. These measurements were repeated for the second Wollaston prism in the same manner. For the second Wollaston prism the characteristic positions were found at $\omega_2 = 33.5°$, 78.5°, 123.5°, 168.5°, 213.5°, 258.5°, 303.5°, and 348.5°. Then, both prisms were inserted into the beam path at the position as illustrated in figure 3.3 with a distance of 10 cm towards each other. The first Wollaston prism was set to $\omega_1 = 179°$ and the second Wollaston prism was rotated to the characteristic positions previously obtained ($\omega_2 = 33.5°$, 78.5°, 123.5°, 168.5°, 213.5°, 258.5°, 303.5°, and 348.5°). The diaphragm at the position of the objective's back focal plane was used to draw the position (X/Y) of each separated spot into a Cartesian coordinate system.

For recording the imaging data for characterization of the fringe pattern, a densely packed layer of fluorescent dyes on glass substrate was placed in the sample holder of the microscope. The free µManager software[73] was used to control the EMCCD camera, which was operated in frame transfer mode at 33.33 ms exposure time and an electron multiplying gain (EMG) of 300. The optical chopper system was used to constantly rotate both light beams' polarization planes at the same speed as previously used (camera: 30 Hz, WP2: 50 Hz, polarization plane: 15 fpp; for details see section 2.2.1). The rotation of the polarization plane was necessary in order to avoid selected excitation only. The fluorescence modulation disappears in the fluorescence intensity average image of the fringe pattern used for characterization but guarantees at the same time that all dyes have been included.[a] The rotation mount including the first Wollaston prism was set to $\omega_1 = 179°$. The rotation mount including the second Wollaston prism was consecutively changed from $\omega_2 = 167.5°$ to $\omega_2 = 260°$ in steps of 2.5° and an additional value at $\omega_2 = 213.5°$. For each ω_2, 100 frames were recorded by the EMCCD camera using rotation of the polarization orientation. The excitation light's illumination power was set to approximately 100 W/cm^2 in the peak maxima.

Experimental spot distances (d_{obj}) at the position of the back aperture of the objective were visualized by a diaphragm and recorded by using a caliper. Spot intensities (I) of the separated beams were recorded before entering the microscope's objective. The power meter was operated in TREND mode usually sampling 5 data points per second and averaging over 5 seconds, unless otherwise mentioned.

3.2.4 Bleaching procedure for interference lithography

For bleaching the interference pattern into a layer of densely packed fluorescent dyes on glass substrate, the EMCCD camera was controlled by µManager software[73] and operated in frame transfer mode at 33.33 ms exposure time and an EMG of 10. Even though no measurements were recorded, the EMCCD camera was of great use to bringing the layer of densely packed fluorescence dyes into the focal plane. The half wave plate was set to constant rotation in the same manner as described in section 2.2.1 in order to constantly rotate the excitation light's polarization orientation, thereby avoiding bleaching of selected orientations only. The principle bleaching procedure is illustrated in figure 3.4. Using moderate illumination intensities (100 W/cm^2), the sample was moved in x and y-direction by the motorized stage in order to apply the structured excitation light's illumination pattern to the homogeneous dye layer. After re-adjusting the focus, the excitation light's beam power was increased 25 fold and applied to the sample for about 10 seconds. All single fluorescence dyes that were exposed to light above a certain intensity were quickly photo-destructed. The only molecules spared from bleaching were the ones that were located within or very close to the nodal lines of the excitation light's illumination pattern. The bleaching procedure was aborted and repeated 24 times at other sample positions in order to obtain a five by five array of bleached positions. The lines

---

[a] It would have been possible to execute the measurements with larger exposure times and circularly polarized light. However, this little work-around was preferred since it did not require set-up modifications.

were to be investigated using fluorescence modulation with alternating excitation with and without ExPAN at another set-up. The array facilitated retrieval of the fringe lines upon switching set-ups.

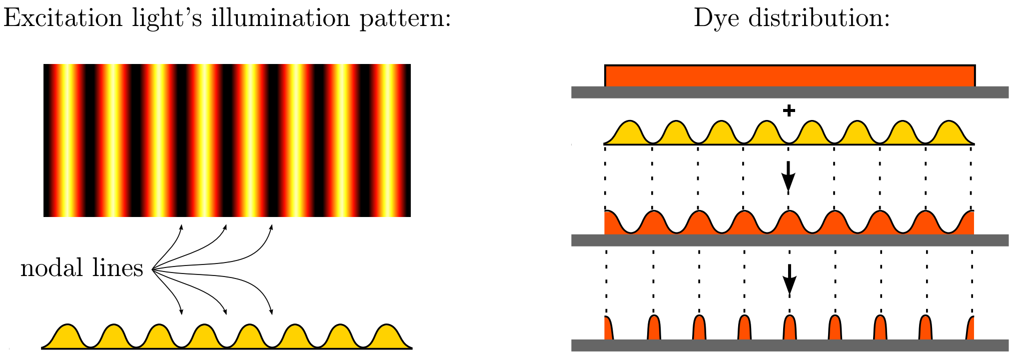

Figure 3.4: Schematic representation of the interference lithography procedure. The excitation light's illumination pattern to the left was shaped sinusoidal with equally distanced nodal lines. Applying this illumination pattern to a self-build photoresist composed of a layer of densely packed fluorescence dyes (orange) on glass substrate (gray), resulted in selective photo-bleaching of those molecules that were not located in the nodal lines. The dye distribution eventually became narrower than sub-diffractional dimensions when using increased excitation light power.

3.3 Results and discussion

As laid out in the theoretical section 3.1.1, several procedures have been reported that achieve interference patterns in the focal plane of the objective. During this thesis, two Wollaston prisms were used for that purpose. In order to obtain a nice interference pattern and being able to control and tune the structures, it was necessary to acquire a thorough understanding of the effects of the Wollaston prisms with respect to the beam's position, intensity, and polarization. For example, by controlling the beam position at the back aperture of the objective, the angle of the interfering beams is altered which changes the fringe periodicity p. First, this section examines the dependency of the beam's position, intensity, and polarization on the angles of the rotation mounts containing the Wollaston prisms (ω_1, ω_2). This is done by first looking at the individual Wollaston prisms one by one (section 3.3.1), followed by investigation of the combination of Wollaston prisms (section 3.3.2). Thereafter, the relationship between the fringe pattern periodicity p and the beams' positions at the back focal plane is examined.

3.3.1 Investigation of spot position, intensity, and polarization after single Wollaston prisms

It is commonly known that one Wollaston prism separates unpolarized light into two orthogonally polarized beam outputs with a certain separation angle. If the orientation of the prism within a set-up is fixed, the positions and the intensities of the individual beams remain constant. During this thesis however, each Wollaston prism was installed into rotation mounts and by changing the prism's orientation, both separated beams rotated point-symmetrically around its point of origin. By inserting a diaphragm into the beam path a certain distance away from the Wollaston prism, the positions in X- and Y-direction of each beam's spot could be described using trigonometric functions. Due to the fact that the input light was vertically polarized, the intensities of the separated beams became functions of the orientation angle of the Wollaston prisms i. e. the angle of the rotation mount.

In a first step, both Wollaston prisms were investigated individually with regard to beam position in X- and Y-direction, beam intensity and beam polarization. Figures 3.5 A and B give an overview of the beam positions of both separated spots for the two Wollaston prisms W1 and W2 (cf. figure 3.3) with corresponding beam intensities which are represented in rainbow-color-coded relative units. The first topic addressed is beam position. For the first Wollaston prism eight characteristic orientations of W1 are shown. The separated spots were labeled 1 and 2 and rotated counter-clockwise around its point of origin. Spot 1 reached maximum intensity at 44° and 224° being at position $(X/0)$ and

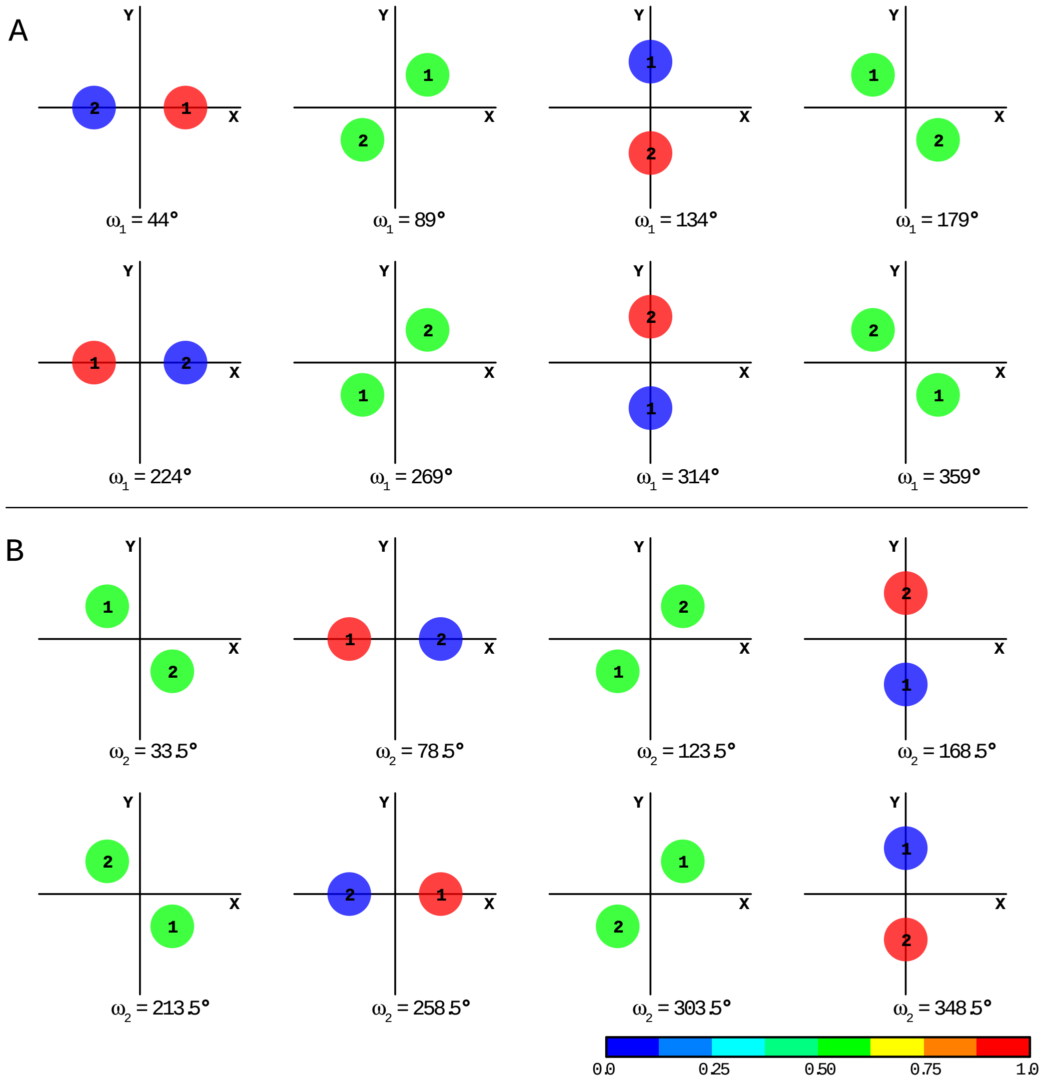

Figure 3.5: Spot position and intensity investigation for W1 (A) and W2 (B). X- and Y-positions in arbitrary units were calculated using equation 3.10 and 3.11 for W1, and using equation 3.12 and 3.13 for W2. Spot intensities were obtained from equation 3.16 for W1, and from equation 3.17 for W2 and are represented in rainbow-coded colors.

(-$X/0$), respectively. These points of interest were used to derive the trigonometric functions in equation 3.10 in order to describe the X- and Y-positions of spot 1 for intermediate angles.

$$X_1(\omega_1) = \cos(\omega_1 - 44^\circ) \qquad Y_1(\omega_1) = \sin(\omega_1 - 44^\circ) \tag{3.10}$$

Herein, ω_1 refers to the rotation mount's angle in angular units of the first Wollaston prism. The phase delay of the trigonometric functions, in this case 44°, did not correspond to a universal constant but rather coincided with the user dependent orientation of the Wollaston prism within the rotation mount. This value will change whenever the Wollaston prism is removed from its mount and readjusted. Table 3.1 summarizes X and Y coordinates obtained from this calculation. The values were in good agreement with experimental observations.

Equivalent treatment of spot 2 whose maximum intensity was reached at 134° and 314° at positions $(0/\text{-}Y)$ and $(0/Y)$, respectively led to the functions in equation 3.11.

$$X_2(\omega_1) = \cos(\omega_1 + 136^\circ) \quad Y_2(\omega_1) = \sin(\omega_1 + 136^\circ) \tag{3.11}$$

Herein, a phase delay of -136° was evaluated in order to describe the X- and Y-positions of spot 2 correctly. Taking both delays of phase into account, the relative delay of phase from spot 1 to spot 2 was obtained to be $44^\circ - (-136^\circ) = 180^\circ$, i. e. half a period length. In the same manner, eight representative orientations of the second Wollaston prism were recorded. In contrast to W1, W2 was fixed in a rotation mount with fine scaling. Spot 1 reached maximum intensity at 78.5° and 258.5° for $(\text{-}X/0)$ and $(X/0)$, respectively leading to the trigonometric functions in equation 3.12.

$$X_1(\omega_2) = \cos(\omega_2 + 101.5^\circ) \qquad Y_1(\omega_2) = \sin(\omega_2 + 101.5^\circ) \tag{3.12}$$

Herein, ω_2 referred to the rotation mount's angle in angular units of the second Wollaston prism. Taking the maximum intensities of spot 2 at 168.5° and 348.5° at positions $(0/Y)$ and $(0/\text{-}Y)$, respectively, into account, the X- and Y-positions of spot 2 were described by equation 3.13.

$$X_2(\omega_2) = \cos(\omega_2 + 281.5^\circ) \qquad Y_2(\omega_2) = \sin(\omega_2 + 281.5^\circ) \tag{3.13}$$

After successfully calculating the X- and Y-positions for the Wollaston prisms used, the next interesting and relevant aspects were beam intensity and beam polarization. By using linearly polarized light, beam intensities of the separated spots depended on the rotation angle of the mount. A Wollaston prism consists of two triangle prisms with perpendicular optical axes (cf. section 3.1.3). In cases, in which the orientation of the polarization plane of the light agrees with the optical axis of one of the two triangle prisms, the intensity is almost completely transfered within this polarization maintaining beam, whereas close to zero intensity can be recognized for the beam with orthogonal orientation. Examples of such cases are shown in figures 3.5 A and B, in which beam intensity is indicated by a rainbow-color-coded scale in relative units. Herein, the blue border of the spectrum refers to small intensities, whereas red colors point out spots of intensities close to maximum. Measuring the polarization orientation of the separated beams led to the observation, that the color red went along with vertically polarized light, i. e. the same polarization as the input light's and that the color blue identified close to non-existent

Table 3.1: Theoretical spot positions of spot 1 (X_1/Y_1) and spot 2 (X_2/Y_2) after the first Wollaston prism for different angles of rotation (ω_1). Theoretical values were calculated according to equations 3.10 and 3.11.

ω_1	X_1	Y_1	X_2	Y_2
44°	1	0	-1	0
89°	$\frac{\sqrt{2}}{2}$	$\frac{\sqrt{2}}{2}$	$-\frac{\sqrt{2}}{2}$	$-\frac{\sqrt{2}}{2}$
134°	0	1	0	-1
179°	$-\frac{\sqrt{2}}{2}$	$\frac{\sqrt{2}}{2}$	$\frac{\sqrt{2}}{2}$	$-\frac{\sqrt{2}}{2}$
224°	-1	0	1	0
269°	$-\frac{\sqrt{2}}{2}$	$-\frac{\sqrt{2}}{2}$	$\frac{\sqrt{2}}{2}$	$\frac{\sqrt{2}}{2}$
314°	0	-1	0	1
359°	$\frac{\sqrt{2}}{2}$	$-\frac{\sqrt{2}}{2}$	$-\frac{\sqrt{2}}{2}$	$\frac{\sqrt{2}}{2}$

low-intense horizontal polarization components. It has to be kept in mind, that the rainbow color-code which actually indicates intensity can only be related to polarization as well in case of single Wollaston prisms used with vertically polarized light. In cases in which the input light's polarization is changed, the color-code scale only applies to intensities. For input light polarizations other than vertical and horizontal, the polarization vector does not agree with neither of the optical axes of the Wollaston prism. As a consequence, the initial polarization vector will be separated into orthogonal components along the optical axes of the Wollaston prism in such a way that its recombination by vector addition would yield the initial polarization vector. Examples of these cases are indicated in figures 3.5 A and B by graphs with light green spots. For example, entering the first Wollaston prism with vertically polarized light at an angle of $\omega_1 = 89°$ resulted in two equally intense spots in the first and third quadrant. The polarization of spot 1 was determined to be $\theta_1 = 45° \pm n \cdot 180°, n \in \mathbb{N}$. Consistently, the second spot showed perpendicular polarization with respect to the first spot with $\theta_2 = 135° \pm n \cdot 180°, n \in \mathbb{N}$. What can be learned from these values is that the final polarization orientation is solely dependent on the orientation of the optical axes of the triangle prisms within the Wollaston prism. In mathematical terms, a linear dependency between the rotation angle of the Wollaston prism and the polarization orientation exists as depicted by equation 3.14 for the first Wollaston prism.

$$\theta_1(\omega_1) = \omega_1 - 44° \qquad \theta_2(\omega_1) = \omega_1 + 46° \tag{3.14}$$

Herein, $\theta_1(\omega_1)$ and $\theta_2(\omega_1)$ refer to the polarization angles of spots 1 and 2, respectively. The orientation of the polarization for the second Wollaston prism were developed similarly, as shown in equation 3.15.

$$\theta_1(\omega_2) = \omega_2 + 101.5^\circ \qquad \theta_2(\omega_2) = \omega_2 + 191.5^\circ \tag{3.15}$$

Several aspects need to be kept in mind whenever angles are mentioned. First, when talking about the polarization's orientation, the angle referred to is given in absolute units that can be directly related to the orientation with respect to the table surface. Vertically polarized light was assigned an angle of $\theta_v = 0^\circ$, 180°, 360°, whereas horizontally polarized light provided angles of $\theta_h = 90^\circ$, 270°, 450°. It became evident that polarization angles repeat after 180°, so that any polarization angle given can be related to angles that match an integer addition or subtraction of 180° ($\theta_v = 0^\circ + n \cdot 180^\circ, n \in \mathbb{Z}$ and $\theta_h = 90^\circ + n \cdot 180^\circ, n \in \mathbb{Z}$). Second, when mentioning angles that refer to the orientation of the rotation mounts of the Wollaston prism one has to consider that these values are of experimental nature and subject to defining a true zero. It makes sense to define the origin along one of the optical axes within the Wollaston prism, so in this case 44° for the first Wollaston prism and likewise 258.5° for the second prism were chosen to be assigned the true zeros. These numbers indicate the phase delay of the cosine-function and depend on the initial polarization orientation. So far, each individual Wollaston prism has been used with vertically polarized light. In cases in which the input polarization is changed the delay of phase is changed accordingly. In other words, the true zero needs correction if polarizations other than vertical are used. For example, when entering with 45° polarization instead of 0° polarized light, the cosine function is shifted by 45° which means that the phase delay changes by 45°. This needs to be kept in mind for later applications. In contrast to polarization angles (θ), mounting angles of the Wollaston prisms repeat after 360°, so any Wollaston angle given can be related to angles that match an integer addition or subtraction of 360° ($\omega_1 = 0^\circ + n \cdot 360^\circ, n \in \mathbb{Z}$).

In order to theoretically calculate the intensity distribution for the separated spots, Malus' law for perfect polarizers was used. In contrast to a single polarizer with a single optical axis, the triangle prisms of the Wollaston prism with perpendicular optical axes were considered to individually operate as a polarizer. Equations 3.16 represent the intensity calculation for the separated spots of the first Wollaston prism.

$$\begin{aligned} I_1(\omega_1) &= I_0 \cdot \cos^2(\omega_1 - 44^\circ) \\ I_2(\omega_1) &= I_0 \cdot \cos^2(\omega_1 + 46^\circ) \end{aligned} \tag{3.16}$$

Herein, I_0, $I_1(\omega_1)$, and $I_2(\omega_1)$ referred to the initial light intensity, the transmitted intensity of spot 1, and the transmitted intensity of spot 2, respectively. In theoretical calculations, I_0 was set to one in arbitrary units. In order to compare theoretical predictions of intensities for the separated spots, experimental values were recorded using a power meter which are given in table 3.2 for the first Wollaston prism. Maximum intensity values of 1 a.u. can be directly related to experimental values around 4.6 mW, whereas minimum values of 0 a.u. matched very low intensities in the µW range. In analogy to the first Wollaston prism evaluations, similar intensity distribution laws were developed for the second prism, as shown in equations 3.17.

$$\begin{aligned} I_1(\omega_2) &= I_0 \cdot \cos^2(\omega_2 + 101.5^\circ) \\ I_2(\omega_2) &= I_0 \cdot \cos^2(\omega_2 + 191.5^\circ) \end{aligned} \tag{3.17}$$

From figure 3.5, one important conclusion can be drawn. The investigations of the spot position (X/Y) show that the distance between both spots remained constant upon rotation of a single Wollaston prism. Since the distance of the beams at the back focal plane of the objective directly determines the fringe pattern periodicity (cf. equation 3.8) and since it is desired to create a set-up in which the periodicity is easily tunable for measurements, achieving beam separation by only one Wollaston prism is quite disadvantageous. In order to change the distance between the spots, a single Wollaston prism would have to be moved within the set-up towards or further away from the objective in order to diminish or enlarge spot distance, respectively. Due to the fact that this is rather impractical, using a single Wollaston prism for beam separation and introducing the interference pattern on the sample is not a method of choice. One way to address this problem is to introduce a stack of two Wollaston prisms into the excitation beam path. How spot position, intensity, and polarization were affected for the Wollaston prisms used will be explained in the following sections.

Table 3.2: Theoretical and experimental spot intensities after the first Wollaston prism for different angles of rotation (ω_1). Theoretical values were calculated according to equations 3.16. Experimental values were sampled over 10 s using a sampling rate of 5 values per second.

ω_1	$I_1(\omega_1)$ / a.u.	$I_1(\omega_1)_{exp.}$ / mW	$I_2(\omega_1)$ / a.u.	$I_2(\omega_1)_{exp.}$
44°	1	4.59±0.04	0	0.032±0.001
89°	0.5	2.23± 0.02	0.5	2.16± 0.02
134°	0	0.038±0.001	1	4.51±0.04
179°	0.5	2.23± 0.02	0.5	2.24± 0.02
224°	1	4.59±0.06	0	0.037±0.001
269°	0.5	2.19± 0.02	0.5	2.23± 0.02
314°	0	0.033±0.001	1	4.59±0.04
359°	0.5	2.22± 0.02	0.5	2.26± 0.02

3.3.2 Investigation of spot position, intensity, and polarization after two consecutive Wollaston prisms

Having developed trigonometric functions for the prediction of the X- and Y-positions of the separated spots for the individual Wollaston prisms, the combination of two Wollaston prisms became mathematically accessible by simple linear combination. As an example, the first Wollaston prism at 179° was combined with eight different positions for the second prism as shown in figure 3.6 A. As a result, each spot after the first Wollaston prism was additionally split up into two spots by the second Wollaston prism, giving a total number of four spots. In order to being able to distinguish the spots when referring to spot position, spot intensity, and spot polarization, they were labeled 1-1, 1-2, 2-1, and 2-2. Herein, the first number was related to the spot number after the first Wollaston prism while the second number referred to the spot number after the second prism. Mathematically, spots 1 and 2 exiting the first Wollaston prism were split up by the second Wollaston prism according to the same equations for spot position as already presented in equation 3.12. The only difference was that the spots 1-1 and 1-2 would not rotate around the point of origin, but rather around the position of spot 1. This meant that in order to describe the position of the newly found spot 1-1, addition of the position laws for the first and second Wollaston prisms (summation of equation 3.10 and equation 3.12) yielded equation 3.18.

$$\begin{aligned} X_{1\text{-}1}(\omega_1,\omega_2) &= \cos(\omega_1 - 44^\circ) + \cos(\omega_2 + 101.5^\circ) \\ Y_{1\text{-}1}(\omega_1,\omega_2) &= \sin(\omega_1 - 44^\circ) + \sin(\omega_2 + 101.5^\circ) \end{aligned} \tag{3.18}$$

The theoretical predictions were verified by calculating the $X_{1\text{-}1}$- and $Y_{1\text{-}1}$-coordinates and comparing them to the experimental positions shown in figure 3.6 A. The position analysis was likewise performed for the other spots by simple addition of the individual laws as summarized in the Appendix (equations 6.1). A summary over all X- and Y-positions is given in table 3.3. By comparing the calculated values in arbitrary unit to the spot positions shown in figure 3.6, it becomes apparent that the agreement is good. What can be learned from the values in table 3.3 is that spots 1-1 and 1-2 rotated around $(\text{-}\sqrt{2}/2/\sqrt{2}/2)$, while spots 2-1 and 2-2 rotated around $(\sqrt{2}/2/\text{-}\sqrt{2}/2)$which were the beam positions after the first Wollaston prism for an angle of $\omega_1 = 179^\circ$ (cf. table 3.1). These results show that beam position after two stacked Wollaston prism can be described by summing the individual position laws.

A major benefit from using two Wollaston prisms is that the distance between the spots is variable, depending only on the angles of the rotation mounts of the Wollaston prisms. This provides evidence that two stacked Wollaston prisms are capable of separating the

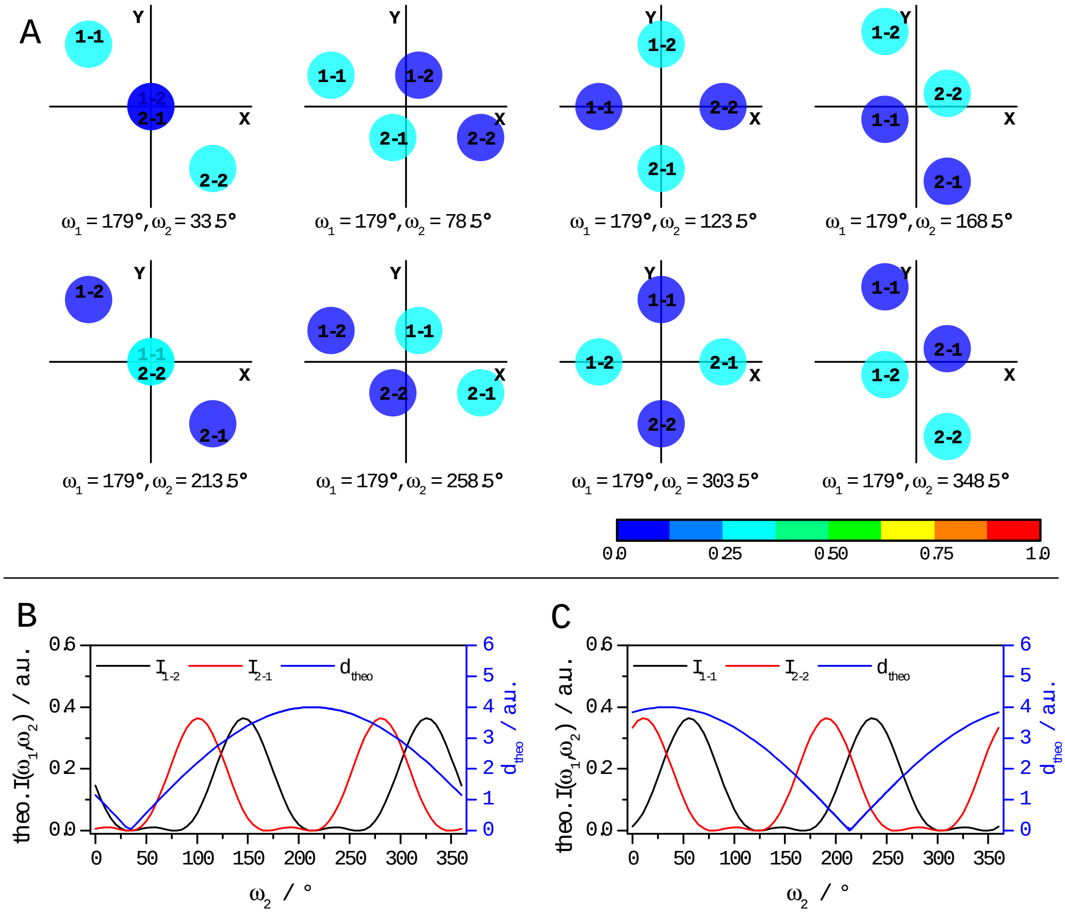

Figure 3.6: Spot position and intensity investigation for two consecutive Wollaston prisms W1 and W2. A) X- and Y-positions in arbitrary units were calculated using equation 3.18 and 6.1. Spot intensities were obtained from equation 3.19 and 6.2 are represented in rainbow-coded colors. B) Plot of spot intensities and spot distance for spots 1-2 and 2-1. C) Plot of spot intensities and spot distance for spots 1-1 and 2-2.

beams such that the distance at the back focal plane of two beams is adjustable thus being able to tune the interference pattern. Even though two Wollaston prisms split one initially coherent wavefront into four beams and only two beams are required for obtaining interference, two beams can simply be blocked in the following beam path toward the objective (cf. figure 3.3). Since the beam's position is not substantially affected by any other set-up parts, the theoretical analysis of beam position is hereby completed.

Looking back at the set-up description in section 3.2.1, the consecutive Wollaston prisms were inserted right before a polarizing beam splitter (PBS2). The reason why the combined Wollaston prisms were not incorporated into the set-up after PBS2 was the insufficient distance to the back aperture of the objective since the angle of divergence of the Wollaston prisms was only 1°. The distance was chosen such that all four spots were to enter the objective in case if the spots spanned a square (e. g. $\omega_1 = 179^\circ$ and $\omega_2 = 123.5^\circ$, or $\omega_1 = 179^\circ$ and $\omega_2 = 303.5^\circ$). In this configuration, the spots were very close to the outer rim of the back aperture of the objective and by switching to another Wollaston

Table 3.3: Theoretical spot positions of spots 1-1, 1-2, 2-1, and 2-2 after two consecutive Wollaston prism (W_1, W_2) for different angles of rotation (ω_1, ω_2). Theoretical values were calculated according to equations 3.18 and 6.1 in the Appendix.

ω_1	ω_2	$\left(X_{1\text{-}1}\middle/Y_{1\text{-}1}\right)$	$\left(X_{1\text{-}2}\middle/Y_{1\text{-}2}\right)$	$\left(X_{2\text{-}1}\middle/Y_{2\text{-}1}\right)$	$\left(X_{2\text{-}2}\middle/Y_{2\text{-}2}\right)$
179°	33.5°	$\left(-\sqrt{2}\middle/\sqrt{2}\right)$	$\left(0\middle/0\right)$	$\left(0\middle/0\right)$	$\left(\sqrt{2}\middle/-\sqrt{2}\right)$
179°	78.5°	$\left(-1-\frac{\sqrt{2}}{2}\middle/\frac{\sqrt{2}}{2}\right)$	$\left(1-\frac{\sqrt{2}}{2}\middle/\frac{\sqrt{2}}{2}\right)$	$\left(-1+\frac{\sqrt{2}}{2}\middle/-\frac{\sqrt{2}}{2}\right)$	$\left(1+\frac{\sqrt{2}}{2}\middle/-\frac{\sqrt{2}}{2}\right)$
179°	123.5°	$\left(-\sqrt{2}\middle/0\right)$	$\left(0\middle/\sqrt{2}\right)$	$\left(0\middle/-\sqrt{2}\right)$	$\left(\sqrt{2}\middle/0\right)$
179°	168.5°	$\left(-\frac{\sqrt{2}}{2}\middle/-1+\frac{\sqrt{2}}{2}\right)$	$\left(-\frac{\sqrt{2}}{2}\middle/1+\frac{\sqrt{2}}{2}\right)$	$\left(\frac{\sqrt{2}}{2}\middle/-1-\frac{\sqrt{2}}{2}\right)$	$\left(\frac{\sqrt{2}}{2}\middle/1-\frac{\sqrt{2}}{2}\right)$
179°	213.5°	$\left(0\middle/0\right)$	$\left(-\sqrt{2}\middle/\sqrt{2}\right)$	$\left(\sqrt{2}\middle/-\sqrt{2}\right)$	$\left(0\middle/0\right)$
179°	258.5°	$\left(1-\frac{\sqrt{2}}{2}\middle/\frac{\sqrt{2}}{2}\right)$	$\left(-1-\frac{\sqrt{2}}{2}\middle/\frac{\sqrt{2}}{2}\right)$	$\left(1+\frac{\sqrt{2}}{2}\middle/-\frac{\sqrt{2}}{2}\right)$	$\left(-1+\frac{\sqrt{2}}{2}\middle/-\frac{\sqrt{2}}{2}\right)$
179°	303.5°	$\left(0\middle/\sqrt{2}\right)$	$\left(-\sqrt{2}\middle/0\right)$	$\left(\sqrt{2}\middle/0\right)$	$\left(0\middle/-\sqrt{2}\right)$
179°	348.5°	$\left(-\frac{\sqrt{2}}{2}\middle/1+\frac{\sqrt{2}}{2}\right)$	$\left(-\frac{\sqrt{2}}{2}\middle/-1+\frac{\sqrt{2}}{2}\right)$	$\left(\frac{\sqrt{2}}{2}\middle/1-\frac{\sqrt{2}}{2}\right)$	$\left(\frac{\sqrt{2}}{2}\middle/-1-\frac{\sqrt{2}}{2}\right)$

angle setting, two of the four spots would be automatically prevented from entering the objective because of hitting the objective's holder.

Due to the fact that the individual spots contain a certain polarization, the effective spot polarization and spot intensity reaching the back aperture of the objective strongly depended on the polarization cube. In order to theoretically describe the spot polarization and spot intensity reaching the back focal plane, the polarizing beam splitter has to be taken into account. A polarizing beam splitter operates as an ideal polarizer and transmits or reflects incoming light depending on the light's polarization orientation according to Malus' law[2] in equation 3.19 as shown for spot 1-1.

$$I_{1\text{-}1} = I_0^* \cdot \cos^2\left(\theta_{1\text{-}1}(\omega_2)\right) \tag{3.19}$$

Herein, $\theta_{1\text{-}1}(\omega_2)$ refers to the polarization angle of the spot 1-1 after the second Wollaston prism and I_0^* to the intensity that enters the polarizing beam splitter, i. e. the light's intensity that remained after both Wollaston prisms. Due to the fact that the angle of polarization is solely dependent on the orientation of the second Wollaston prism, all spots' polarization orientations can be described by equation 3.15. As a consequence, spots 1-1 and 2-1 possess equal polarization, as well as spots 2-1 and 2-2[b], as shown in equa-

---

[b] As a reminder: 1-1 is the short version for spot 1 from W1 and spot 1 from W2

tions 3.20.

$$\theta_{1\text{-}1}(\omega_2) = \theta_{2\text{-}1}(\omega_2) = \omega_2 + 101.5^\circ \quad \theta_{1\text{-}2}(\omega_2) = \theta_{2\text{-}2}(\omega_2) = \omega_2 + 191.5^\circ \tag{3.20}$$

Concerning I_0^*, it is not possible to simply multiply the individual intensity laws from equations 3.16 and 3.17 in order to obtain I_0^* since both laws were developed for vertically polarized input light. However, the first Wollaston prism operating with vertical polarization affected the light's polarization so that the intensity law of the second Wollaston prism could not be used as given but needed adaption. I_0^* can be expressed as the corrected intensity law for the second Wollaston prism i. e. the intensity that remains after the second Wollaston prism. The explanation of obtaining I_0^* is as follows. Since the first Wollaston prism was set to 179°, the light's polarization angle of spot 1 after the first prism was determined to be 135°, whereas spot 2 showed a polarization orientation of 225°, each spot possessing half the input's intensity ($I_0/2$). In general, the input intensity is given by the intensity laws after the first prism ($I_1(\omega_1)$, as shown in equation 3.16. Looking back at figure 3.5 B, for the second Wollaston prism and for vertically polarized light, the true zero for spots 1 and 2 were defined to be -101.5°[c] and -191.5°, respectively. As an example, the corrected true zero after entering the Wollaston prism using light whose polarization was rotated 135° with respect to 0° of the vertically polarized light can be re-obtained by rotating the Wollaston prism by 135° itself. In other words, the initial correction number 101.5° was enhanced by the value of the polarization orientation. The intensity of spot 1-1 after the second Wollaston prism corrected for the variable input polarization from the first prism is shown in equation 3.21.

$$I_0^* = I_1(\omega_1) \cdot \cos^2(\omega_2 + 101.5^\circ - \theta_1(\omega_1)) \tag{3.21}$$

By combining equations 3.16, 3.19, and 3.21 a finalized version for the intensity description of spot 1-1 was obtained taking all set-up effects into account. The corresponding intensity equations for the other spots 1-2, 2-1, and 2-2 can be found in equation 6.2 in the Appendix.

$$I_{1\text{-}1} = I_0 \cdot \cos^2(\omega_1 - 44^\circ) \cdot \cos^2(\omega_2 + 101.5^\circ - \theta_1(\omega_1)) \cdot \cos^2(\theta_{1\text{-}1}(\omega_2)) \tag{3.22}$$

Figure 3.6 A summarizes the spot intensity and spot position information for the eight chosen examples. These images corresponded to the effective intensity arriving at the back aperture of the objective. Herein, in the range between $\omega_2 = 348.5^\circ$ and $\omega_2 = 78.5^\circ$,

---

[c] -101.5° equaled the position given at 258.5° in figure 3.5 B, since $-101.5^\circ + 360^\circ = 258.5^\circ$.

spots 1-2 and 2-1 are close to one another, whereas in the range between $\omega_2 = 168.5°$ and $\omega_2 = 258.5°$ the spots 1-1 and 2-2 would be close enough to be the interfering beams. By using the Pythagorean theorem, the theoretical distances between the interfering spots 1-2 and 2-1, as well as 1-1 and 2-2 were calculated separately. The final distance curves are given in figures 3.6 B and C, respectively in arbitrary units on the right axes. On the left axes, the corresponding spot intensities are shown. As can be seen for spots 1-2 and 2-1 in figure 3.6 B, when the distance d_{theo} between spots 1-2 and 2-1 turns small, the intensities become little as well. In contrast to this case, spots 1-1 and 2-2 in figure 3.6 C possessed large intensity peaks within the range of small spot distances. This range between $\omega_2 = 168.5°$ and $\omega_2 = 258.5°$ was considered well suited for a closer investigation on the final interference pattern within the focal plane of the objective as outlined in the next section.

3.3.3 Fringe pattern characterization

An understanding of the developed equations in the previous sections is especially helpful if other settings are desired. The functions are of a basic nature so that they can be easily adapted to scenarios that differ from the one presented here. This section will bring the considerations to the next level by looking at the resulting interference pattern in the focal plane of the fluorescence imaging microscope and by characterizing the fringe pattern with respect to fringe periodicity p and orientation β. The first Wollaston prism was set to $\omega_1 = 179°$, and the angle of the second Wollaston prism was changed in the range between $\omega_2 = 167.5°$ and $\omega_2 = 258.5°$ in steps of 2.5°, with one additional value at $\omega_2 = 213.5°$. Microscopy cover slips with a very dense layer of ATTO 590 molecules on the surface were brought into the focal plane of the objective so that the fringe pattern became visible. Using µManager software[73] operating at 33 ms exposure time at 300 EMG, 100 frames were recorded, as described in section 3.2.3. The image processing tool Fiji[126] was used to average the intensity values for each pixel for the 100 frames. Twelve exemplary average intensity images for different angles of the second Wollaston prism are shown in figure 3.7 and were used to characterize the fringe pattern.

The characterization was based on the evaluation of the parameters fringe pattern orientation β and fringe periodicity p and relating them to the spot position, spot distance, and spot intensity at the back aperture of the objective. Concerning the latter, a power meter was used to measure the experimental spot intensities independently from one another by blocking one beam at a time. Concerning the spot distance, a caliper was used to obtain experimental values. Distance and intensity measurements were obtained for the same angle range of the second Wollaston prism as given for the imaging data. All experimental values are summarized in separate graphs in figure 3.8 along with a comparison to theoretical values if applicable.

The first parameter of interest was the orientation of the fringe pattern (β) with respect to the bottom border of the recorded image. The angle was obtained by the white angle calibration lines below the insets in figure 3.7. The fringe pattern orientation (β) was a direct consequence of the interference of two beams, whose experimental spot position was to be best described at the back aperture of the objective. Having a look at the orientation of the fringe pattern in figure 3.8 A, it became evident that the angle β increased almost steadily with a large jump at $\omega_2 = 213.5°$. In other terms, the orientation of the fringe pattern rotated counter-clockwise. Due to the fact that both spots 2-2 and 1-1 also rotated counter clock wise, it was attempted to relate the angle of orientation in the fringe pattern to the angle of the spot position at the back aperture of the objective (β_{obj}). In the region from $\omega_2 = 168.5°$ to $\omega_2 = 213.5°$, spot 2-2 rotated within the first quadrant of a Cartesian coordinate system.. By using the X- and Y-positions at the back aperture, the angle β_{obj} became accessible by simple trigonometric calculations, as shown in equation 3.23.

$$\beta_{\text{obj}} = \frac{180°}{\pi} \cdot \arctan\left(\frac{Y_{2\text{-}2}}{X_{2\text{-}2}}\right) \tag{3.23}$$

Herein, β_{obj} describes the angle of spot 2-2 within the first quadrant at the back aperture of the objective. In the region from $\omega_2 = 213.5°$ to $\omega_2 = 258.5°$, spot 2-2 rotated within the third quadrant which meant that in order to obtain the correct angle a fixed number of 180° needed to be added to the same calculation in equation 3.24.

$$\beta_{\text{obj}} = 180° + \frac{180°}{\pi} \cdot \arctan\left(\frac{Y_{2\text{-}2}}{X_{2\text{-}2}}\right) \tag{3.24}$$

The evaluated angle β obtained from the experimental fringe patterns and the corresponding calculated angle at the objective β_{obj} were plotted within the same graph in figure 3.8 A and showed good results concerning the course of the function. The experimental β values were shifted upwards by 90° with respect to theoretical calculations of β_{obj}. This met the expectations since the orientation of the fringe lines was required to appear perpendicular with respect to the connecting line between the interfering spots (cf. figure 3.1). Deviations between the theoretical calculations and the experimental values occurred around 213.5°. In theoretical terms, there should be a singularity at this point because the position of spot 2-2 was predicted to be (0/0), thus leaving the solution to equations 3.23 and 3.24 undefined. Under experimental conditions, an interference pattern was seen at this point even though both interfering spots would be on the same position, namely the center of the back aperture of the objective. Due to the fact that Wollaston prisms introduced beam separation at a small angle of 1°, the beams of spots

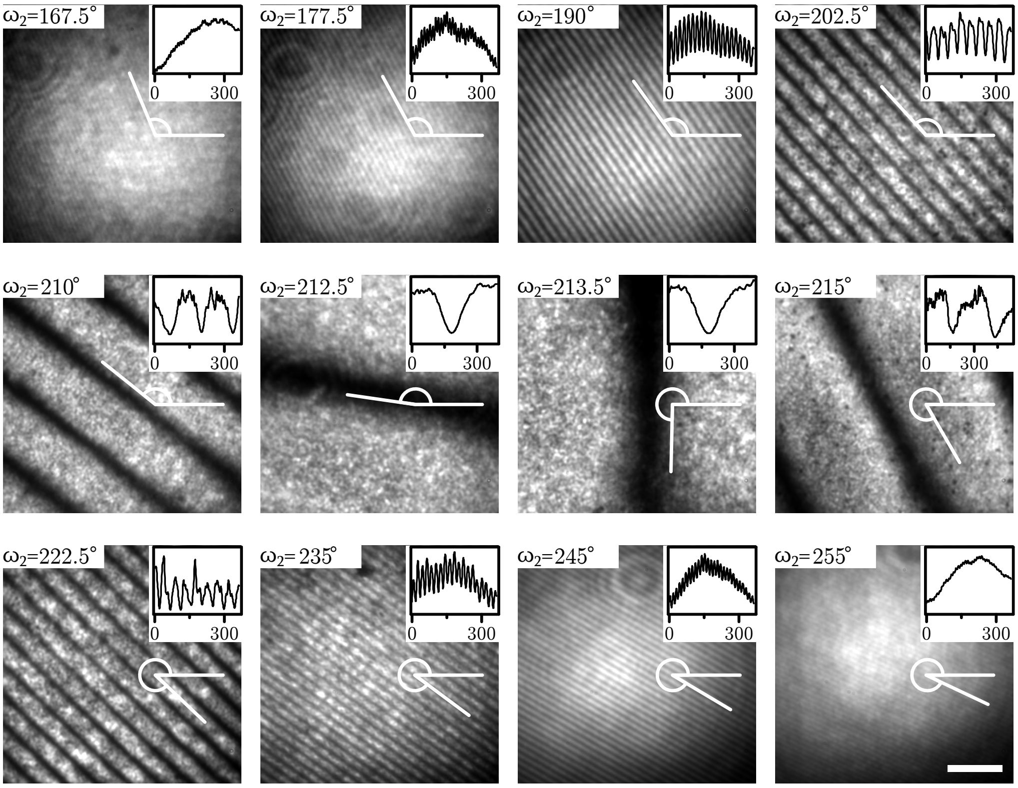

Figure 3.7: Averaged fluorescence intensity images of twelve fringe patterns in relation to the orientation of the second Wollaston prism (ω_2 given to the top left of each image). The white angular arms served as a measure for the angle orientation of the fringe pattern. Plot insets to the top right of each image represented profile plots from lines oriented perpendicular to the nodal lines of the interference pattern. Scalebar 5 µm.

2-2 and 1-1 did not hit the objective exactly collinear. This meant that even if both spots entered the objective at the same spot, their slight difference in propagation remained within the optics of the large magnification objective (60x), thus still causing an interference pattern. For this reason, an angle of $\beta = 180°$ was recorded at 213.5° of the second Wollaston prism.

The distance (d_{obj}) between spots 1-1 and 2-2 was experimentally measured at the back aperture by using a caliper. The results of d_{obj} were plotted in figure 3.8 B in dependency of the angle of the rotation mount of the second Wollaston prism (ω_2). Included in the plot were results from theoretical distance calculations by the Pythagorean theorem from the spot positions, as shown in equation 3.25. In the range from $\omega_2 = 168.5°$ to $\omega_2 = 213.5°$, the spot distance decreased almost linearly before it re-increased in the range from $\omega_2 = 213.5°$ to $\omega_2 = 258.5°$. Some experimental values around 213.5° are missing because it was not possible to distinguish the individual spots by eye. All in all, the overlay between experimental and theoretical values showed a good agreement. By plotting experimental results against the theoretical values and fitting a linear function to the thus obtained graph, a calibration factor of $d_{\text{obj}}/d_{\text{theo}} = 2.9$ mm/a.u. was obtained (fit shown in figure 6.1 in Appendix). Using this value, theoretical aspects of spot position and spot distance as

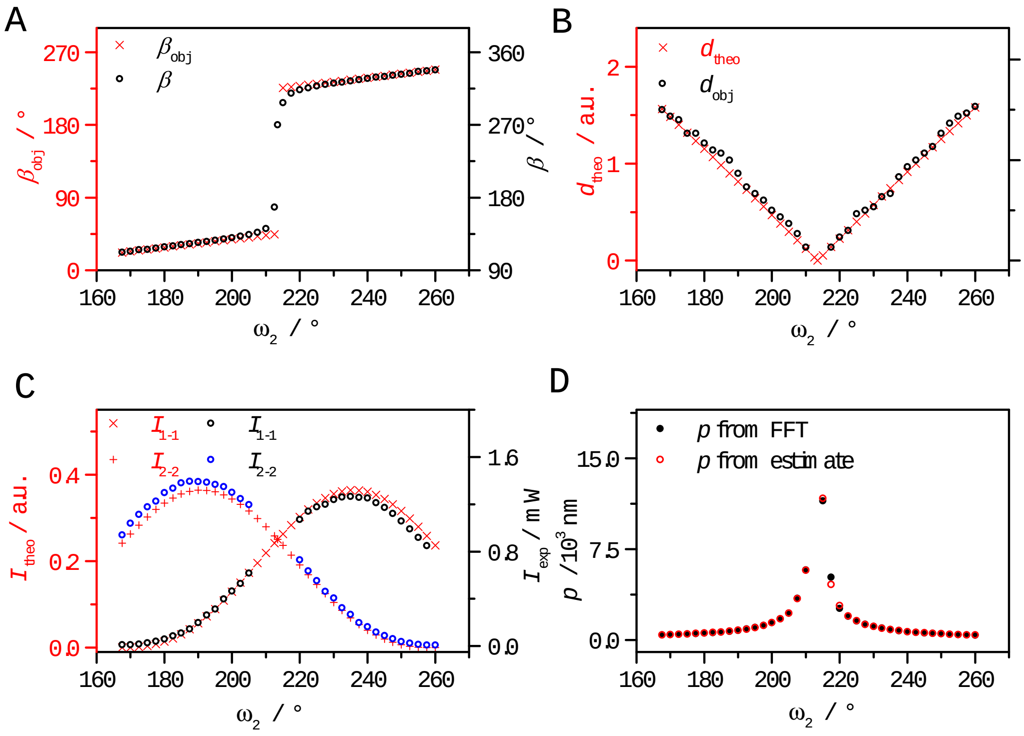

Figure 3.8: Plots of parameters that characterized the fringe pattern in relation to the angle of the second Wollaston angle (ω_2). A) Orientation of the fringe pattern lines (black, β) and orientation of spots at the back aperture (red, β_{obj}). B) Theoretical (red, d_{theo}) and experimental (black, d_{obj}) spot distances at back aperture of objective. C) Theoretical (red) and experimental (black/blue) spot intensities at back aperture of objective. D) Experimental fringe periodicity p evaluated from estimation (red) or FFT (black) in the interference pattern.

previously presented in the preceding sections could be extended from arbitrary units to proper, absolute units of length.

$$d_{\mathrm{theo}} = \sqrt{(X_{2\text{-}2} - X_{1\text{-}1})^2 + (Y_{2\text{-}2} - Y_{1\text{-}1})^2} \tag{3.25}$$

In the previous section, equations have been developed for describing the spot intensity at the back aperture in arbitrary units. In order to check the validity of the theoretical spot intensity calculations from equation 6.2, the calculated values were plotted in direct comparison to the experimental values as shown in figure 3.8 C. Herein, theoretical spot intensities in arbitrary units are depicted by red crosses while experimental data points are drawn in blue and black circles. Again, several experimental values were missing in the range from $\omega_2 = 207.5°$ to $\omega_2 = 217.5°$ due to the spots' close distance for which it was not possible to exclusively measure the spot intensity from one spot only. Both experimental curves matched the progression of the theoretical functions fairly well with respect to the position of extrema. Interestingly, experimental spot intensities for spot 2-2 slightly exceeded the theoretical expectations, whereas spot 1-1 underachieved. This discrepancy between the amplitudes was within 10% variation, when considering the maximum intensity values of the individual curves (1.266 mW/1.395 mW= 0.91). This order of magnitude for the beam's imperfection often occurred for set-ups using multiple optical elements. In many cases, a small error in the beginning was enhanced slightly by several objects rather than from one element alone. For this reason, it was refrained from finding and investigating the system's imperfection further. It should also be kept in mind that the fringe patterns shown in figure 3.7 were obtained by beam interference of beams whose spot intensities varied on much larger scales. Looking at the image in which the second Wollaston prism was set to 190°, the spots intensities differed from 1.392 mW to 0.198 mW for spots 2-2 and 1-1, respectively. Neglecting the spot's intensity discrepancy seemed reasonable.

The second, and more important parameter of interest was the distance between fringes, also called fringe periodicity p. For evaluating p from the fluorescence average data, two methods were tested in comparison. First, a simple estimation took place by counting the number of peaks per distance. This was achieved by defining a plot profile line perpendicular to the nodal lines of the interference pattern. The corresponding intensity plots are shown in the top right insets of the individual averaged intensity images in figure 3.7. The second method of evaluation relied on the same intensity profile plots. Instead of manually counting peaks, a Fourier transform was performed on the plot profile. The results of both are shown in figure 3.8 D in units of length. Herein, the values evaluated from FFT calculations (black circles) matched the results from simple estimation (red circles) quite well. For Wollaston angles of $\omega_2 = 212.5°$ and $\omega_2 = 213.5°$, in which only one fringe line was recorded by the field of view of the camera, neither analysis was possible. At first, in the range from $\omega_2 = 168.5°$ to $\omega_2 = 198.5°$, the fringe periodicity p enlarged slowly from about 400 nm to approximately 1 µm, almost in linear steps. Then, p increased rapidly from $\omega_2 = 201.5°$ until what appeared to be the pole at $\omega_2 = 213.5°$. This behavior was mirrored to the side of increasing angles for the second Wollaston prism. Within the first 15° after $\omega_2 = 213.5°$, the fringe periodicity decreased rapidly to 1/10 of the maximum recorded value, which was close to $p = 12$ µm. Since one frame comprised 512 x 512 pixels of the effective size of 42.5 nm each, the recorded image was approximately 21.8 µm wide. The resulting diagonal length of the image (30.8 µm) can be considered the absolute maximum distance covered within one image. In order to be able to identify individual fringes for either evaluation method, estimation or FFT, two complete fringes (with left and right end) needed to be recorded within one frame. Taking these thoughts into account, it was expected that under the current set-up configurations a maximum fringe periodicity of 20 µm would be analyzable.

So far, it became evident that the orientation of the fringe pattern (β) could be estimated from the position of the interfering spots at the back aperture of the objective. According

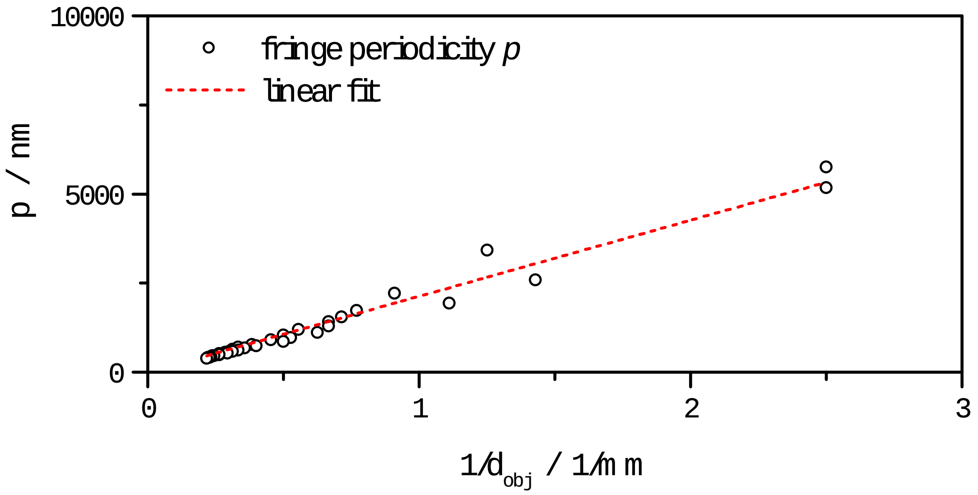

Figure 3.9: Plot of fringe periodicity p over the inverse of the spot distance ($1/d_{\mathrm{obj}}$). The slope of the linear fitting function (red dash) is (2132 ± 50) nm mm.

to equation 3.8, the fringe periodicity p should be directly related to the spot distance d_{obj}. As can be seen from figures 3.8 B and D, for decreasing spot distance d_{obj} on the back aperture, the fringe periodicity p of the interference pattern in the focal plane of the objective increases. In order to verify the theoretical functionality in equation 3.8, the values for p obtained from FFT were plotted over the inverted values for spot distance ($1/d_{\mathrm{obj}}$) in units of length. The final plot is shown in figure 3.9 and the results indicate that the fringe periodicity is linearly proportional to the inverse of the spot distance ($p \propto 1/d_{\mathrm{obj}}$). This result is quite important because it supports the validity of equation 3.8 which was based on Abbe's sine law ($\sin(\phi) \propto r_d$). In other words, the angle at which the interfering beams intersect (2ϕ) which determines the fringe periodicity p according to equation 3.7 is shown to be controllable by the off-axis distance r_d because Abbe's sine law accounts for this objective. As a consequence, the knowledge of the positions of the beams at the back aperture of the objective can be directly transfered into the prediction of the fringe pattern periodicity. In order to gain an understanding of the maximum and minimum fringe periodicity possible under the current set-up conditions, a linear fitting function was applied to the plot of p over $1/d_{\mathrm{obj}}$ whose slope was determined to be $m = (2132 \pm 50)$ nm·mm. Due to the fact that fringe periodicities above 20 µm would exceed the current field of view of the EMCCD camera, the limiting factor towards the maximum fringe distance is given by the camera and not by the spot distance d_{obj}. For this fringe periodicity, the spots at the back aperture would have to be no more than $d_{\mathrm{obj}} =$ 2132 nm·mm/20 000 nm $\approx$ 0.1 mm apart. Any spot distance below this value causes the fringe pattern to exceed the field of view.

Towards the lower range of fringe periodicity, the most obvious limit is the maximum spot distance achievable at the back aperture of the objective. The microscope objective used for fringe pattern characterization possessed a back aperture width of 10 mm. This would leave a minimum fringe periodicity of $p = 2132\,\text{nm}\cdot\text{mm}/10\,\text{mm} \approx 213.2\,\text{nm}$. However, several other aspects have to be taken into account that enlarge the latter number. First, both beams did not enter the objective coaxial due to the fact that Wollaston prisms introduced small beam deviation angles. Consequently, their propagation vectors tilted away from the microscope objective's axis. Light entering at the utmost outer rim of the back aperture of the objective that possessed a small angle pointing away from the objective's axis, would not be directed to the focal plane because of hitting the optics' holders within the objective. This leads to the assumption that the maximum effective spot distance is smaller than 10 mm. Secondly, the beam's entrance point referred to the center of the beam's cross section. However, the beam's diameter was not infinitely small but in order to provide a smooth and homogeneous interference pattern, the full cross section of the beam's diameter was required to reach the focal spot. Naturally, this could only be achieved if the beams entered the objective even further away from the outer rim of the back aperture of the objective. Thirdly, by increasing the off-axis distance r_d, the angle ϕ towards the objective's axis also increased. If ϕ exceeds a certain critical angle ϕ_c, the beam will not propagate to the focal plane since it is totally reflected at the glass-medium interface. The critical angle for total internal reflection (TIR) is given by equation 3.26.

$$\phi_c = \arcsin\left(\frac{n_2}{n_1}\right) \tag{3.26}$$

Herein, n_1 and n_2 are the refractive indices of the cover glass[d] and the medium outside the objective, respectively. If measurements had been conducted with a droplet of water on the sample surface, a critical angle of $\phi_c = \arcsin(n_2/n_1) = \arcsin(1.33/1.518) \approx 61.18°$ would have been obtained. This value is very close to the maximum angle possible (ϕ_{max}) given by the numerical aperture of the objective ($\phi_{max} = \arcsin(NA/n) = \arcsin(1.35/1.518) \approx 62.79°$). In cases in which the range is small at which TIR occurs ($\phi_{max} - \phi_c = \phi < 2°$), the objective is considered unsuitable for TIR microscopy.[127][128] Throughout this thesis however, no water droplet was used on the sample surface, thereby increasing the difference between the refractive indices of the media and reducing the critical angle massively ($\phi_c = \arcsin(n_2/n_1) = \arcsin(1/1.518) \approx 41.21°$). The available TIR range was greatly expanded ($\phi_{max} - \phi_c = \phi \approx 20°$) or in other words, the range for creating interference patterns without TIR decreased. For angles below the critical angle ($\phi < \phi_c$), the interference pattern would be created in the focal plane of the objective. For angles above the critical angle ($\phi > \phi_c$), it has been reported that an interference pattern can in general be created, resulting in a standing wave (SW) caused by TIR at

---

[d] The refraction at the objective/cover glass interface is neglected since their indices of refraction are very similar and a special oil of the same refractive index is used as contact medium.

the glass surface.[93][129][130] Objective-based SW-TIRF is known to cause several problems, like uneven illumination and additional interference fringes.[131][132] Several different solutions to the technical challenges had been reported[133] i. e. rapidly modulating the spot position at the back focal plane by rotating wedge-shaped glass elements,[134] by using acousto-optical deflectors[135] or by using tip-tilt scanning mirrors.[136] In this set-up configuration, TIR was simply avoided by supervising that the off-axis distance r_d never exceeded the critical angle. In order to calculate the critical distance $r_{d,c}$, Abbe's sine law was used which states that the objective's effective focal length f equals a constant quotient of r_d and $\sin(\phi)$ ($f = r_d / \sin(\phi)$). The critical distance $r_{d,c}$ was estimated to be $r_{d,c} = \sin(\phi_c) \cdot r_{\max} / \sin(\phi_{\max}) = \sin(\phi_c) \cdot r_{\max} / \mathrm{NA} \cdot n_{r,\mathrm{obj}} \approx 0.37\,\mathrm{cm}$ using $r_{\max} = 0.5\,\mathrm{cm}$, $\mathrm{NA} = 1.35$, $\phi_c = 41.21°$, and $n_{r,\mathrm{obj}} = 1.518$. As a consequence to avoiding TIR, the minimum fringe periodicity observable under current set-up configurations was also affected. A new calculation of the lower limit yields a fringe periodicity of $p = 2132\,\mathrm{nm{\cdot}mm}/(2 \cdot 3.7)\,\mathrm{mm} \approx 288.1\,\mathrm{nm}$. This value can be considered to be the effective bottom border of p for the given light source. Due to the fact that p is directly proportional to the wavelength of the light (λ), it is expected that smaller fringe periodicities should be achievable using other light sources.

3.3.4 Fringe pattern prediction for interference lithography

So far, empirical spot position, spot distance and fringe periodicity have been understood, described by equations, and related to one another. This chapter focuses on the use of the developed equations with respect to predicting certain scenarios. For instance, it was desirable to use spots that would interfere with equal amplitudes i. e. their measured intensities at the back focal plane of the objective would be the same. In order to mathematically predict the angles of rotation for both Wollaston prisms matching this criterion, the quotient of spot intensities $I_{2\text{-}2}$ and $I_{1\text{-}1}$ was required to equal one, as described by equation 3.27.

$$1 = \frac{I_{2\text{-}2}}{I_{1\text{-}1}} = \tan^2(\omega_1 - 44°) \cdot \tan^2(\omega_2 + 101.5°) \qquad (3.27)$$

Due to the fact that $I_{2\text{-}2}$ and $I_{1\text{-}1}$ were both products of cosine-squared functions depending on two variables, namely the angles of rotation of the Wollaston prisms, substituting variables and applying trigonometric relationships allowed simplifying the full expression to a simple product of squared tangent functions. The step-by-step derivation of equation 3.27 is listed in the Appendix in equation 6.3. Due to the fact that both variables appeared in separate arguments, equation 3.27 was rearranged to give the angle of the first Wollaston prism (ω_1) in dependency of the second mount's angle containing the second Wollaston prism. The final function is given in equation 3.28.

$$\begin{aligned} \omega_1 &= 180^\circ n \pm \frac{180^\circ}{\pi} \cdot \arctan\left(\cot(\omega_2 + 101.5^\circ)\right) + 44^\circ \\ \tan&\left(\omega_2 + 101.5^\circ\right) \neq 0;\ \sec\left(\omega_2 + 101.5^\circ\right) \neq 0;\ n \in \mathbb{Z} \end{aligned} \tag{3.28}$$

In order to verify the theoretical predictions, experimental values were recorded for a chosen area of interest. The second Wollaston prism was set to values between $\omega_2 = 185^\circ$ and $\omega_2 = 204^\circ$, the corresponding angles for the first Wollaston prism (ω_1) were calculated according to equation 3.28 and experimental intensity values were recorded at the back focal plane of the objective using a power meter. Spots 1-1 and 2-2 were measured individually by blocking the other beam. Additionally, the total intensity and the spot distance d_obj were recorded. Table 3.4 summarizes all important measurements.

Table 3.4: Experimental spot intensities at the back focal plane for combinations of ω_1 and ω_2 which are expected to yield equally intense spots. Experimental values were sampled over 10 s using a sampling rate of 5 values per second. n.m. not measured

ω_1	ω_2	$I_\text{1-1}$ / µW	$I_\text{2-2}$ / µW	I_total / µW	d_obj / mm
188.5°	204°	368±2	362±2	730±4	2.0
190.5°	202°	325±2	326±1	652±4	n.m.
192.5°	200°	288±1	285±2	570±4	2.4
196.5°	196°	204±1	203±1	406±2	3.4
197.5°	195°	182±1	182±1	365±2	n.m.
198.5°	194°	168±1	170±1	338±2	3.6
199.5°	193°	145±1	146±1	291±2	3.9
201°	191.5°	127.8±0.8	124.4±0.6	253±2	4.4
207°	185.5°	45.5±0.3	45.5±0.3	99± 1	5.4

As can be seen from the values in table 3.4, experimental intensity values corroborate the theoretical predictions and validate the applicability of equation 3.28. As a major advantage, equal intensity combinations can be theoretically calculated and from the known angles of rotation for both Wollaston prisms, it is possible to tune the fringe periodicity with underlying interference beams of equal intensity.

The gained knowledge was used to design a fringe pattern with a fringe periodicity of $p \approx 1\,\mu\text{m}$ which was used for experiments concerning interference lithography. As a self-built photoresist, a densely packed layer of fluorescent dyes on glass substrate was used. By increasing the intensity of the interfering beams, the interference pattern was imprinted into the photoresist since dyes that experience an intensity above a certain threshold irrevocably photo-bleach. Only fluorophores within or very close to the nodes of the interference pattern (zero intensity) remain intact and form a negative image of the fringe pattern. The focus of the last chapter of this thesis (Chapter 4) lies on investigating this negative image with respect to the node width by means of fluorescence modulation with alternating excitation with and without ExPAN. In order to characterize these node widths, individual lines needed to be cropped from the raw data for evaluation which is why the fringe periodicity was chosen to be $p \approx 1\,\mu\text{m}$. If p were chosen to be too small, characterization of individual lines would be massively hindered due to the fact that cropping the data would include fluorescence components from the adjacent lines. If the fringe periodicity were quite large, only a small number of lines would appear within the field of view. Since the region of effective ExPAN is limited to approximately $30\,\mu\text{m}^2$ (diameter $\sim 6\,\mu\text{m}$) only single lines would be accessible to evaluation which would require many more sample positions and measurement. Weighing both factors up against each other, a fringe periodicity of 1 µm would provide five lines in the effective ExPAN region per measurement while still providing sufficient distance towards adjacent lines. According to the results from section 3.3.3, the distance of the two interfering spots is then required to be approximately $d_{\text{obj}} = 2132\,\text{nm}\cdot\text{mm}/1000\,\text{nm} \approx 2.1\,\text{mm}$ at the back focal plane of the objective. In order to obtain spots of equal intensity at the back aperture of the objective at this distance, the settings were estimated from table 3.4. The first rotation mount was set to $\omega_1 = 189°$ while the second Wollaston prism in the other rotation mount was rotated to $\omega_2 = 203.5°$. With these parameters, the interference pattern in the focal plane of the objective was expected to show fringes with a spacing of about 1 µm. Using these settings, the interference pattern was bleached into the self-built photoresist according to the procedure described in the experimental section 3.2.4. In the last chapter of this thesis, this negative image is subject to further investigation using fluorescence modulation with and without ExPAN.

4 Line pattern characterization by fluorescence modulation

The final chapter of this thesis focuses on the characterization of the negative image obtained by interference lithography which was accomplished by bleaching the interference pattern into a layer of densely packed dyes (cf. Chapter 3). The negative image of the bleaching pattern consists of fluorescent dyes that survived the bleaching procedure. The remaining fluorophores are those which were located within or near the nodes of the fringe pattern thus forming lines of fluorescent dyes. These lines were subject to investigation by fluorescence modulation alternating between excitation with and without ExPAN. Basic concepts of fluorescence modulation with respect to enhanced photo-selection by ExPAN have been presented in Chapter 2, thus bringing all pieces of this thesis together in the current chapter. In the theoretical section, the optical resolution barrier in fluorescence microscopy is introduced along with several super-resolution techniques that break or circumvent this limit. Then, the mathematical fundamentals of solving so-called inverse problems by an alternating-variable-search method (AVM) with respect to single molecule localization are outlined. In the result section, special attention was given to the evaluation of the line width by means of localizing single molecules using AVM. First, an assessment of the distribution of single molecule localizations from averaged fluorescence data in the single molecule regime is given, thus providing information about the line widths from non-modulated fitting. Then, the alternating-variable-search method is extended to single molecule localization with modulated fluorescence data corroborating the applicability of AVM with modulation based data with respect to the line width investigation. Finally, AVM was applied to selected examples of lines at higher dye densities, thus providing a basic for the investigation to what extent fluorescence modulation can be used for resolution improving purposes.

4.1 Theoretical background

4.1.1 Super-resolution fluorescence microscopy

Ernst Abbe (1840-1905) published his contribution to the resolution limit of optical microscopes[71] in the late 19th century (cf. equation 2.17 in section 2.1.6). From then on, the distance d at which two point sources can still be resolved was quantified and has ruled fluorescence microscopy for many decades to follow. Since $\sin(\phi)$ does not exceed the value one and the refractive index of air can be assumed to have a value of one,[137] the lateral resolution limit of light can be approximated by half the wavelength of light used ($d \approx \lambda/2$). For the VIS spectrum of light (400-700 nm), the resolution limit ranges from 200 to 350 nm which unfortunately exceeds the range for studying biophysical processes at the molecular level of cells. Throughout the last three decades, the desire of understanding sub-diffractional processes translated into a large effort for breaking or circumventing the diffraction barrier that had ruled microscopic resolution for so long. The list of successful techniques is quite extensive and full of fancy acronyms as shown in table 4.1. The importance of fluorescence based super-resolution technologies was emphasized in 2014 when Eric Betzig, Stefan W. Hell, and William E. Moerner were jointly awarded the Nobel prize of chemistry "for the development of super-resolved fluorescence microscopy."[138] A full explanation of all techniques is beyond the scope of this thesis but a brief overview of three major categories is given.

Techniques like 4Pi, NSOM, I^{5}M, and SIM can be summarized into the first category which do not really break or circumvent the diffraction barrier, but rather push it to its very limits by modifying the propagation of light.[139] In 4Pi and I^{5}M for example, two opposing objectives are used in order to increase the collection efficiency and thereby increasing the axial resolution fivefold. However, lateral resolution improvement in this category is rather moderate and essentially limited so that it may at maximum be considered moderately resolution enhancing.

The remaining two categories are real super-resolution techniques successfully breaking and circumventing the diffraction limit of light down to a few nanometers. Both groups profit from exploiting the fluorescence properties of dyes and the manner in which the technique alters the fluorescence characteristics defines to which category it belongs. These techniques intervene in the dye's fluorescence behavior between a fluorescent bright state (ON-state) and the dark, non-fluorescent state (OFF-state). One group of techniques, including GSD, RESOLFT, SSIM, and STED, approaches the fluorescence manipulation from a deterministic perspective. STED uses a stimulated emission beam whose intensity profile is shaped as a doughnut and induces the de-excitation from the ON to the OFF-state. Fluorescence emission is consequently only admitted from the central region of the doughnut whose inner diameter (d_{STED}) is given by equation 4.1.

$$d_{\mathrm{STED}} \approx \frac{\lambda}{\mathrm{NA} \cdot \sqrt{1 + I_{\mathrm{se}}/I_s}} \tag{4.1}$$

Herein, I_{se} is the intensity of the stimulated emission laser beam and I_s the saturation (threshold) intensity which is a fluorophore specific characteristic. By increasing I_{se}, the

Table 4.1: Overview of super-resolution microscopy techniques.

Acronym	Super-resolution technique
4Pi	4Pi microscopy[140][141][142]
NSOM	Near-field Scanning Optical Microscope[143][144][145]
I^5M	I^5M microscopy[87][108][142]
SIM	Structured Illumination Microscopy[85][91][92]
GSD	Ground State Depletion[146][147][148]
RESOLFT	REversible Saturable Optical Linear Fluorescence Transition[149][150]
STED	STimulated Emission Depletion[41][42]
SPEM	Saturated Pattern Excitation Microscopy[107]
SSIM	Saturated Structured Illumination Microscopy[116]
SOFI	Super-resolution Optical Fluctuation Imaging[151][152]
NALMS	NAnometer-Localized Multiple Single-molecule fluorescence microscopy[153]
FIONA	Fluorescence Imaging with One-Nanometer Accuracy[20]
(d)STORM	(direct) STochastic Optical Reconstruction Microscopy[154][155][156]
PALM	PhotoActivated Localization Microscopy[157][158][159]
PAINT	Point Accumulation for Imaging in Nanoscale Topography[160]

inner doughnut diameter d_{STED} decreases thus strongly confining the area from which fluorescence is allowed. The final diameter can eventually be reduced to the size of the single fluorescence molecule. By scanning the de-excitation STED beam across the sample and knowing the spatial coordinates of its center, discerning point sources closer than the diffraction limit of light is realized and summarized into a super-resolution image thereof. Even though the need for scanning leads to larger image acquisition times, STED was shown to be suitable for parallelization by creating an array of multiple doughnuts[161][162][163][164] or by using arrays of lines by structured illumination.[107][116] Due to the fact that deterministic super-resolution techniques directly influence the system's PSF, these methods are often considered truely breaking the diffraction limit.

The other group of super-resolution providing imaging techniques relies on the localization of individual emitters and is regarded to address super-resolution from a stochastic perspective. As shown in section 2.1.6, the PSF represents the fluorescence response from a point source in a diffraction limited microscope system. If the system's PSF is known and knowledge exists that only one emitter contributed to it, it can be assumed that the point source is situated in the center of the distribution. The molecular position of the dye can be obtained fitting a Gaussian distribution function to the PSF. The localization precision $\sigma_{x,y}$ in two dimensions scales with the standard deviation of the peak function σ_{PSF} and is given in equation 4.2 as first derived by Thompson *et al.*[165]

$$\sigma_{x,y}^2 = \frac{\sigma_{\mathrm{PSF}}^2}{N_p} + \frac{a^2/12}{N_p} + \frac{8\pi\sigma_{\mathrm{PSF}}^4 b^2}{a^2 N_p^2} \tag{4.2}$$

Herein, a is the size of an image pixel, b is the background noise per pixel, and N_p the number of detected photons. The first term of equation 4.2 accounts for photon shot noise while the second term accounts for noise caused by the finite size of camera pixels. The last term further introduces the contributions of background noise. In cases, in which the background contributions can be neglected, the localization precision is assumed to scale linearly with the standard deviation of the PSF distribution and with the inverse square root of the total number of detected photons[166] as summarized in equation 4.3.

$$\sigma_{x,y} \geq \frac{\sigma_{\mathrm{PSF}}}{\sqrt{N_p}} \tag{4.3}$$

A point emission source of a wavelength of 500 nm approximately shows a standard deviation of the PSF of around 200 nm. A localization precision of better than 10 nm is mathematically already achieved if detecting more than 400 photons which is readily achieved using regular fluorescent dyes.[167] Since individual dyes can be localized with a precision down to a few nanometers,[20] the subsequent localization of emitters can provide super-resolution. As a prerequisite for this purpose, the number of molecules in the ON-state needs to be reduced so that only a small portion of the molecules emits. If the ON-fraction becomes small enough, it is statistically probable that each fluorescence spot is the result from a single dye and that multiple dyes do not overlap.

The super-resolution techniques STORM and PALM control the ON-fraction by using special fluorophores which can be photo-activated or photo-switched. PALM relies on photo-activatable (PA) molecules like PA-GFP (green fluorescent protein). Herein, the sample is simultaneously illuminated with two wavelengths of light. One laser is used to activate a small portion of PA-GFP while the second laser excites activated PA-GFP to the fluorescent state. The fluorescence spot centers can be localized before PA-GFP irreversibly photo-bleaches to a dark state. The cycle of activation, localization and bleaching is repeated several times until a sufficient number of molecules have been localized. All localizations are then transfered into the super-resolution image.

In contrast to PALM whose PA dyes photo-bleach irreversibly, STORM uses photo-switchable dyes like Cy5. Herein, all fluorophores are transfered to a dark state by a strong red laser pulse. Then, a green laser pulse switches only a small fraction of dyes into an active state. Upon illumination with the red pulse again, only the active fluorophores emit before they return to the dark state. The emitted photons are used to localize the molecules and repetition of the switching cycle allows the reconstruction of the overall super-resolution image from all individual localizations.

Both mentioned statistic readout methods provided remarkable resolution enhancements compared to the diffraction limit of light in their initial publications. STORM resolved fluorescent dyes attached to double stranded DNA which were separated by approximately 40 nm and confirmed a single molecule localization precision of 8 nm for a cyanine dye.[154] These promising techniques soon addressed their limiting factor, namely dye photo-physics and many publications followed extending the field of photo-activatable and photo-switchable dyes to fluorescence proteins.[24][168][169][170]

4.1.2 Inverse problems and least squares minimization

In the course of this thesis, fluorescence data sets were recorded that can be regarded as a direct consequence of certain parameters, for example the number of molecules N emitting photons at defined positions x,y. Many more parameters influence the data set, which makes it difficult or impossible to trace back the molecule's positions from the fluorescence data for example. In mathematical terms, the recorded data D can be described by a theoretical model function M that relates physical parameters p to D[171] as described by equation 4.4.

$$M(p) = D \tag{4.4}$$

Looking at equation 4.4, three different kinds of mathematical problems can be distinguished. First, in cases in which the parameters p are known and used to compute $M(p)$, mathematicians speak of forward problems. Second, a model identification problem arises when D and p are known and used to find and define the model function M. Third, by trying to find a set of parameters p for which the model function $M(p)$ resembles the measured data D best, the algorithm solves so-called inverse problems. The latter category suits the problems discussed throughout the following section. Herein, the fluorescence data sets resemble the measured data D while the parameters can be regarded as a finite set of many parameters, which is expressed as an n element vector $\vec{p}$. This leads to a new description of equation 4.4 as seen in equation 4.5.

$$M(\vec{p}) = \vec{D} \tag{4.5}$$

These mathematical problems are classified as parameter estimation problems or discrete inverse problems and differ by the number of parameters. In the course of this thesis, the goal was to find a set of parameters $\vec{p}$ which describes the measured fluorescence data $\vec{D}$ best. However, a perfect solution to $M(\vec{p}) = \vec{D}$ cannot be found in real systems due to e. g. noise or effects that are not included in the model function M. In order to get as close as possible to the correct solution several techniques can be applied, for example maximum likelihood estimation[172][173] or least squares minimization.[174][175][176]

$$F(\vec{D},\vec{p}) = \sum_i (\vec{D}_i - M_i(\vec{p}))^2 \tag{4.6}$$

The least squares functional $F(\vec{D},\vec{p})$ which corresponds to the sum of the squared differences between the data $\vec{D}$ and the model function value $M(\vec{p})$ is shown in equation 4.6. Minimization of the least squares functional can be regarded as a fitting procedure in which the best set of parameter $\vec{p}$ is found for which the solution to the model function $M(\vec{p})$ is closest to the data set $\vec{D}$. In cases in which the analytical solution to the functional minimization is too complicated, iterative algorithms provide aid in finding points of convergence. The best solution is expected to be found in the global minimum, unfortunately, convergence in local minimum triggers the optimization procedure to end, even though this might not be the best solution yet. Which minimum will be found strongly depends on the point from which the optimization procedure is started.[171] Special global optimization methods that avoid convergence to a local minimum have been developed in the past decades, e. g. stochastic methods.[177] Unfortunately, some of these methods allow only a small number of variables in order to reduce the computational cost of the optimization procedure. Due to these drawbacks, global optimization methods were not applied in the course of this thesis. Instead, an attempt is made to avoid local minimum convergence by appropriately choosing starting parameters (which are already close to the global minimum) in combination with applying an alternating-variable search method (AVM) for functional minimization. In the following section 4.1.3, the fundamental theory is outlined in mathematical terms whereas sections 4.3.3 and 4.3.4 focus on the practical application of the alternating-variable search method to modulation based fluorescence data.

4.1.3 Alternating-variable search method (AVM)

As previously outlined, the set of parameters $\vec{p}$ that best describes the data set $\vec{D}$ is obtained by minimizing the least squares functional in equation 4.6. There are generally two classes of existing solution methods: the direct search methods and the gradient-based methods.[178] The latter use approximated gradients of the model function $M(\vec{p})$ in order to define a search direction. This requires differentiable functions and even then the exact gradient may be very difficult to estimate. Direct search methods do not rely on gradient estimates in order to evaluate the search direction. Instead, direct comparisons of function values for altered parameters define the search direction. The direct search method used throughout this thesis is a modified alternating-variable-search algorithm (AVM) according to Korel.[11] AVM is capable of minimizing the value of a function, in this case the least squares functional, with respect to each variable or parameter in turn. From a set of reasonable starting parameters $\vec{p}_0$, the first parameter is individually increased and decreased by a value s, while the other input variables are held constant. The functional is calculated and compared to the initial input. If the function value increases, the process is considered a failure and no change to the parameter is applied. If the function value decreases, the process is regarded as a successful change. In other words, the subsequent decrease in the functional leads to a permanent change of the parameter by the step size s in the corresponding direction $p_n \leftarrow p_{n-1} \pm s$. The new parameter p_n is now regarded as the new starting point and the iteration process is repeated for a certain number of iterations. Then, the second, third, fourth, ... parameter are optimized in the same exploratory manner until one optimization cycle is fulfilled. It is noteworthy that each parameter is assigned an individual step size s in the beginning of the optimization procedure. Depending on the nature of the parameter, this step-size value can be decreased during optimization. More details regarding parameters and step-size are given in the corresponding sections 4.3.3 and 4.3.4 in which the mathematical terms of the AVM algorithm are related to the practical parameters of fluorescence data. The optimization procedure continuously cycles around the input parameters until no further optimization direction for any of the parameter can be identified. If the input parameters have been chosen in a reasonable way, the functional should be reasonably close to a minimum in the end of the iterative procedure.

It has been reported in literature that the alternating-variable search strategy is considered to be a simple heuristic method[178] due to simple calculations.[179] Its efficiency and small storage requirements led to a wide range of applications, especially in the field of practical engineering.[180]

4.2 Experimental section - Material and methods

The following experimental section will provide a detailed description of the wide-field fluorescence microscope set-up using alternating excitation with and without ExPAN. This set-up was already in existence[8] and was solely used for recording fluorescence data from the lines of fluorescent dyes obtained after the photo-bleaching process explained in section 3.2.4. A detailed description of the measuring procedure is given.

4.2.1 Set-up details

A schematic design of the set-up for alternating ExPAN and no ExPAN excitation experiments is shown in figure 4.1. Light from a CW diode laser (568 nm, Sapphire) passed a pair of lenses (L1: AC127-025-A-ML, f = 25 mm, Thorlabs, L2: AC254-100-A-ML, f = 100 mm, Thorlabs) that expanded the beam to a diameter of approximately 10 mm. The beam was reflected by a mirror and passed a polarization filter and an electronically controlled beam shutter before it entered the polarizing beam splitter (PBS: PBS121, 420-680 nm, Thorlabs). The combination of a polarization filter and polarizing beam splitter allowed a continuous adjustment of the excitation light power. In exactly the same way as in section 2.2.1, the polarizing beam splitter was used on the one hand to couple the excitation light beam with the de-excitation light beam and on the other hand to improve the quality of the linear polarizations of both beams. The de-excitation light was generated in a Ti:Sa laser (Mira 900-F, Coherent) which was pumped by a frequency doubled neodymium vanadate laser (Verdi 18, Coherent). The Ti:Sa was operated in CW mode and emitted light with a wavelength of 708 nm. The beam was expanded by a pair of lenses (L3: AC127-025-B-ML, f = 025 mm, Thorlabs, L4: AC254-050-B-ML, f = 050 mm, Thorlabs) and passed an electronically controlled beam shutter before it was coupled into the beam splitter. The excitation and de-excitation light possessed perpendicular polarization planes with respect to one another and passed two identical achromatic quarter wave plates (QWP1, QWP2, AQWP05M-600, Thorlabs) which were used instead of a single half wave plate in order to rotate the polarization plane of the beams. The first quarter wave plate was mounted into a continuous rotation mount and adjusted in a way that the wave plate's principal plane was aligned at 45° with respect to the excitation and the de-excitation light's input polarization planes each. In other words, since the input polarization planes are perpendicular to one another, the wave plate's principal plane had to be fixed along the corresponding bisecting line. In this configuration only, the input beams' linear polarizations were retarded by a quarter wavelength along the wave plate's slow axis, thus resulting in circular polarized output beams. The second quarter wave plate was mounted onto a chopper wheel and attached to a ball bearing as described in section 2.2.1. An electric motor controlled by an OCS was likewise used to constantly rotate the second quarter wave plate. The interaction of circularly polarized with a quarter wave plate yielded linearly polarized light whereby the orientation of the polarization vector was determined by the orientation of the second quarter wave plate. Thus, constant rotation of the second quarter wave plate yielded constant rotation of the polarization planes of both beams. A pair of mirrors, an achromatic lens (L5: AC254-150-A-ML, f=150 mm, Thorlabs) and a dichroic mirror (D: XF2045, Omega Optical) were used to direct the beams to the back focal plane of the microscope objective (UPLSApo 100XO, 100x, NA = 1.4, oil immersion Olympus) which was mounted in an inverted microscope body (IX 50, Olympus). In order to increase the local power density of the stimulated emission beam within the sample, lens five was used to diminish the effective area of illumination of the ExPAN beam. The sample was placed in a sample chamber on a motorized stage (Scan IM, Märzhäuser Wetzlar) that allowed sample scanning in the two lateral dimensions *x* and y. Fluorescence light was collected by the same objective and passed the dichroic mirror and a tube lens. A deflecting prism was used to reflect the fluorescence light into a light-proof detection unit in which it passed a filter (F: band pass filter, 620/60 ET, AHF). A pair of lenses (L6: AC254-150-A-ML, f=150 mm, Thorlabs, L7: AC254-100-A-ML, f=100 mm, Thorlabs) was used to further enlarge and direct the image onto an EMCCD camera (iXon 897, Andor). As a result, the final image magnification was increased from 100-fold to 320-fold.

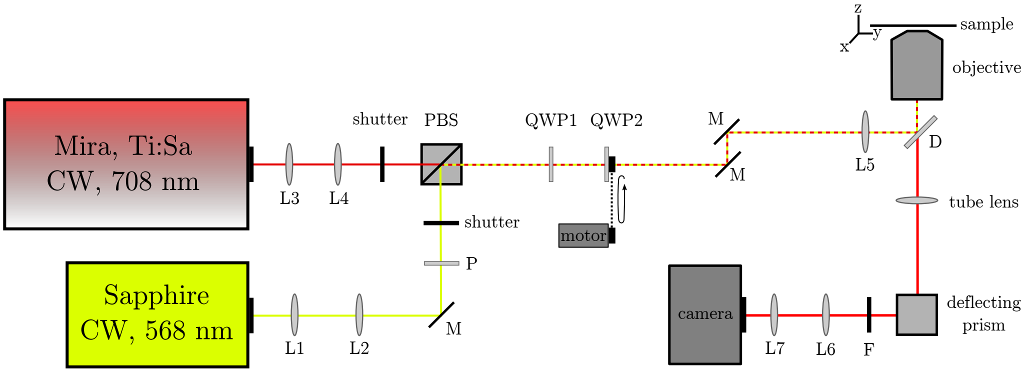

Figure 4.1: Schematic design of the ExPAN set-up for measurements of the fringe patterned samples showing set-up components and beam paths of the excitation beam (568 nm), the stimulated emission beam (708 nm) and the emission light beam (650 nm). Optical parts are labelled as follows: D dichroic mirror, F filter, L lens, M mirror, P polarization filter, PBS polarizing beam splitter, QWP quarter wave plate.

4.2.2 EMCCD camera calibration

The calibration procedure of the line pattern measurement set-up using alternating excitation with and without ExPAN was executed in the same manner as described in section 2.2.2. In principle, the technical features of this EMCCD camera were the same. Slight changes in the detection unit result in a differing magnification. The calibration

Table 4.2: Summary of the repetitive mode control settings of the measurement cycle using alternating excitation with and without ExPAN in combination with and without modulation.

Mode:	no modulation	dark	modulation	modulation with ExPAN	modulation	dark
frame range:	1-80	81-160	161-240	241-320	321-400	401-480
excitation beam:	568 nm	block	568 nm	568 nm	568 nm	block
stimulated emission beam:	block	block	block	708 nm	block	block
chopper rotation:	off		on	on	on	

yielded an effective pixel size of $(50.0 \pm 0.1)\,\mathrm{x}\,(50.0 \pm 0.1)\,\mathrm{nm}^2$, resulting in an overall magnification factor of (320 ± 1).

4.2.3 Measurement procedure

The fringe patterned sample was removed from the interference lithography set-up and inserted into the motorized stage sample holder from the measuring set-up in section 4.2.1. The free µManager software[73] was used to control the EMCCD camera. For measuring different sample positions, changing settings were applied which were summarized in table 4.3. In contrast to the ExPAN set-up using pulsed excitation light from section 2.2.1 and the interference lithography set-up from section 3.2.1, the ExPAN set-up using CW laser light as the excitation source generated the excitation light's polarization modulation by using two equivalent quarter wave plates instead of a single half wave plate. As previously described, one full rotation of the polarization orientation of light (180°) corresponded to 90° rotation of the half wave plate i. e. a factor of two had to be kept in mind constantly. Using a quarter wave plate however, the rotation angle ratio between the polarization's orientation and the quarter wave plate was one, thus requiring a different factor for the OCS. In order to record more data points per period, one full rotation of the polarization orientation of light (180°) was mapped to 20 frames. Along with the same explanation as in section 2.2.3, 20 frames per period were achieved by multiplying the external trigger signal (imaging speed: 30 frames per second) with a fixed factor of 75/30[a].

---

[a] The imaging speed equaled 30 frames per second (30 Hz). Desiring one full rotation of the polarization orientation of light (180°) per 20 frames meant that the 1.5 full rotations (1.5x180° = 270°) per 30 frames i. e. per second were required. 1.5 full rotations of the polarization orientation of light (270°) corresponded to 270° rotation of the quarter wave plate i. e. chopper blade per second. The chopper blade used contained 100 holes, so 270° rotation per second meant 75 chops per second (75 Hz). The internal multiplication factor was a direct consequence of this consideration (75 Hz/30 Hz = 75/30).

In contrast to the ExPAN set-up using pulsed excitation light from section 2.2.1, the ExPAN set-up using CW laser light as the excitation source was additionally equipped with two electronically controllable beam shutters. Using Matlab, both shutters which were positioned in different beam paths (see figure 4.1) were separately controlled in combination with triggering the start and stop mode of the OCS. On the one hand, this configuration enabled repeatedly opening and closing the stimulated emission beam path thereby allowing the sample illumination to alternate between excitation with and without ExPAN, which will be referred to as *modulation with ExPAN* and *modulation* mode, respectively. On the other hand, controlling the start and stop mode of the OCS system permitted switching between constant rotation mode and no rotation mode of the quarter wave plate. Without rotating, the excitation light's polarization orientation remained fixed i. e. the modulation of the fluorescence was suppressed. Initially, a small time delay between the trigger signal stopping the rotation and the subsequent halt of the quarter wave plate was witnessed. In order to spare the sample from unnecessary illumination, both beam shutters were therefore closed (*dark* mode) while changing from modulation mode (excitation without ExPAN) to *no modulation* mode (no wave plate rotation) or vice versa. The final control over the four italicized modes and their synchronization to the camera frame rate was accomplished by Matlab. One full measurement cycle consisted of 480 frames divided into 80 frames for six consecutive modes, being first: no modulation, second: dark, third: modulation, fourth: modulation with ExPAN, fifth: modulation, and sixth: dark. In table 4.2, one full measurement cycle with all corresponding modes is shown, summarizing the settings for the OCS chopper rotation system and the beam shutters.

During the measurements, the complete cycle was repeated up to 7.5 times and synchronized to the camera frame rate. The settings for camera exposure time, camera EMG and excitation power of the 568 nm wide-field illumination light were varied for different measurements and sample positions. A summary of the settings is presented in table 4.3. The excitation power of the 568 nm wide-field illumination light was measured directly in front of the microscope objective i. e. before entering it. Upon increasing the

Table 4.3: Summary of measurement parameters of the fringe patterned samples. Exposure time and EMG refer to EMCCD camera settings whereas the excitation power (568 nm) listed was measured before entering the microscope objective.

measurement's number	exposure time	EMG	excitation power (568 nm)	frames recorded
1	33 ms	500	1.0 mW	3600
2, 3	33 ms	500	2.3 mW	3600
4, 5	66 ms	200	2.3 mW	3600

exposure time of the camera for measurement numbers four and five, the EMG value was scaled down in order to avoid overcharging the camera. The measurement's number will be used as a guide to identify the experimental heritage of the evaluated data in the results section. Throughout all measurements, the stimulated emission's beam illuminated a circular area of about 30 μm^2 when unblocked, resulting in a de-excitation power density of approximately 2.5 MW/cm^2.

4.3 Results and discussion

4.3.1 Common data processing steps

In order to be able to evaluate and characterize the individual line widths, several data processing steps prior to evaluation were applied. All data processing steps were conducted by Fiji,[126] an open source program with standard settings unless otherwise mentioned. First, since the recorded raw data videos consisted of lines of a certain angle of orientation which was impractical for evaluation, the first processing step encompassed data rotation for the entire video by an angle δ. In order to apply the standard rotation tool in Fiji with bilinear interpolation, the best angle of rotation needed to be evaluated such that the final data lines were oriented horizontally. As a matter of fact, different sample positions appeared to require slightly differing δ which was probably a direct consequence of translating the sample in-between measurements. Therefore, the δ needed to be evaluated for all measurements independently. If thinking about traffic, it is commonly known that the shortest way of crossing the street is by going exactly perpendicular with respect to the course of the street. In terms of fluorescence lines, any *way across the street* can now be regarded as full width at half maximum (FWHM) across the line. If the fluorescence line were to be crossed diagonally, a large FWHM value would be obtained. If the fluorescence line were to be crossed perpendicular instead, the resulting FWHM value would be minimized. So, by rotating the line incrementally around the expected angle and evaluating the angle dependent FWHM value across the fluorescence lines, the minimum FWHM value (*shortest way*) satisfied the best angle of rotation. For each measurement (see table 4.3), at least 15 lines were evaluated and averaged per angle of rotation. Plotting the mean FWHM value over the rotation angles δ allowed fitting a second order

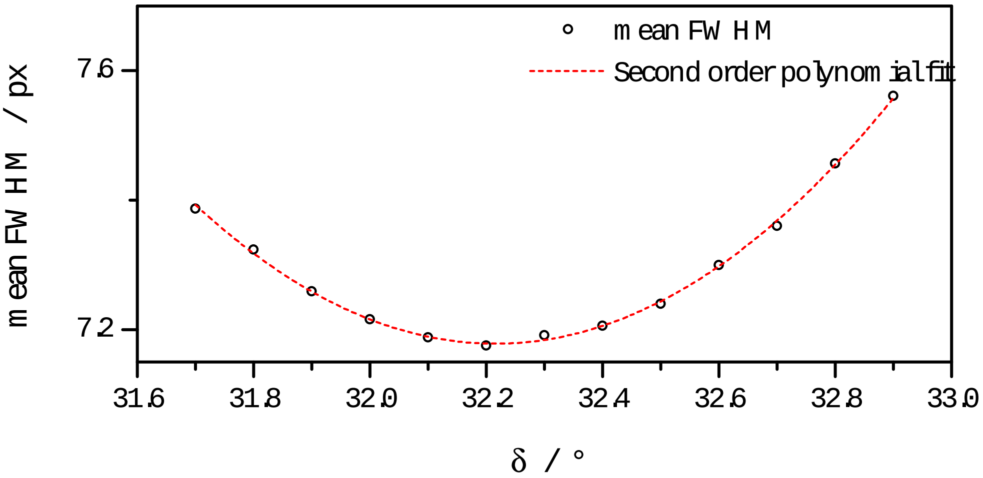

Figure 4.2: Angle dependent plot of averaged line widths (mean FWHM) in order to find the optimum angle for the data rotation.

polynomial function $y(x)$ to the data points as can be seen in figure 4.2. The minimum point of the fitting function is expected to show the optimum δ and can be evaluated by zeroizing the derivative function of the second order polynomial ($\mathrm{d}y/\mathrm{d}x = 0$). In this manner, the optimum rotation angles were evaluated for all different sample positions and are summarized in table 6.1 in the Appendix.

After data rotation, the region of interest i. e. the line of interest was cropped from the video. Usually, the length of the crop in x-direction differed from region to region, whereas the length in y-direction was kept constant at 11 pixels. Those data crops consisting of single fluorescence lines were the basis for creating time i. e. phase-dependent fluorescence carpets. By using Fiji's data binning tool, the fluorescence intensity within one individual image frame was averaged in y-direction. Repeating this procedure for all following frames and stacking all y-bins to one single image resulted in a new image which will be referred to as fluorescence carpet. A visualization of the data processing steps is given in figure 4.3. One common additional processing tool was oversampling which meant that pixels were divided into subpixels in the given direction without interpolation. For example, when referring to oversampling three-fold in x-direction, 1 pixel was divided into three pixels with equal intensity in x-direction. By avoiding interpolation, the data was not changed but more data points were generated which facilitated fitting procedures as described later on.

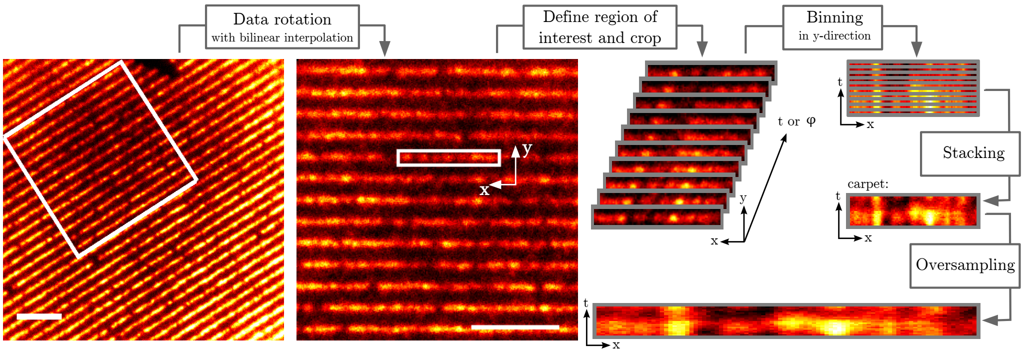

Figure 4.3: Overview of common data processing steps in Fiji.[126] Scale bar equals 4 µm.

4.3.2 Line distance characterization

The first cause of interest with respect to the line characterization was the line distance. Based on the results of Chapter 3, the fringe pattern was intended to show a distance of approximately 1 µm. In order to evaluate the line distance, a profile plot perpendicular to the fluorescence lines was extracted from the rotated intensity image in figure 4.3. The intensity plot covers 13 peaks which are shown in figure 4.4. A cumulative Gaussian fitting function gave access to the centers of the individual lines. By calculating the difference between two successive peak centers and averaging all thus obtained values, an

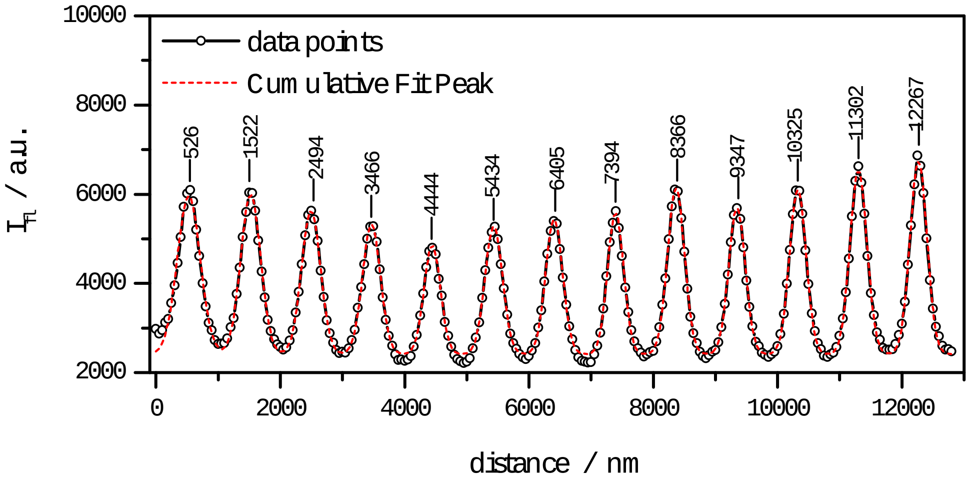

Figure 4.4: Line distance characterization by fitting cumulative Gaussian functions to the profile plot across the fluorescence lines.

average line distance of (978 ± 3) nm was found. Even though this value lies below the expected and initially intended line distance, it proved sufficient for further evaluation in which individual lines are cropped from the data. In order to investigate single lines of fluorescence dyes, it had to be ensured that the fluorescence contribution from the line below or above does not influence the results substantially. As a mathematical measure that this was indeed not the case for the given lines, the standard deviation of the individual Gaussian distribution functions was averaged to be $\sigma = (143 \pm 5)$ nm. It is commonly known that the contribution three times the standard deviation away from the center of the peak (3σ) dropped to approximately 1 per mille. The peak centers in this example possess a distance of approximately 6.8 σ from center to center and a distance of 3.4 σ from center to minimum. Therefore, the contributions feature such small numbers that they can be neglected or in other words, they are not expected to cause any influence on the further data evaluation.

4.3.3 Non-modulated single molecule fitting using AVM

In section 4.1.3, the theoretical and mathematical background of the alternating-variable search method was outlined. This section will focus on the explicit application of AVM to single molecule fitting for non-modulated fluorescence data. Herein, the task of the algorithm is to fit the positions x_i and y_i of a certain number of single fluorescence molecules N_i with a brightness b_i to the recorded data. The variables x_i, y_i, N_i, and b_i resemble the set of parameters $\vec{p}$ spoken of in the theoretical section which are iteratively changed in order to minimize the least squares functional between the fluorescence data image $\vec{D}$ and the model image $M(\vec{p})$. The input data set $\vec{D}$ is a fluorescence intensity image stack of the length of one signal modulation period. It was obtained by cropping 80 frames from the rotated raw data and calculating a phase averaged stack thereof. The final length was 20 frames (= one full signal period) and for non-modulated fitting, the algorithm calculated the average fluorescence intensity image thereof. Before $\vec{D}$ was used for least squares minimization, the algorithm divided each pixel into nine sub-pixels without value interpolation, i. e. oversampling in both directions x and y was applied. Last, an input offset was subtracted from all pixels, so that the final input data set $\vec{D}$ used for AVM can be summarized as an offset-corrected oversampled fluorescence intensity image average.

The initial model image was produced by mathematically convolving the initially guessed spatial x_0 and y_0 positions with the point spread function (PSF) assuming a starting brightness b_0. This meant that the algorithm needed to be equipped with the PSF, with a position list of the single molecules, and remaining parameters, like brightness and step sizes s. Concerning the first, the PSF was calculated from experimental and technical data using the Richards and Wolf[181] PSF generation implementation in Fiji.[126] In order to guess the initial single molecule's positions, the averaged fluorescence intensity image was calculated and point ROIs were placed by hand in the center of the fluorescence spots. Then, the point ROIs were transferred into an empty image which possessed the size of the oversampled data set $\vec{D}$. The algorithm is capable of extracting the x_0 and y_0 positions from the point ROI image. Last, all molecules were equipped with the same starting brightness b_0 parameter. Then, the algorithm iteratively optimized the variables brightness b, position x, and position y for initially given step sizes s for each parameter for a given number of iterations. The step sizes were chosen to remain constant at one for the parameters position x ($s_x = 1$) and position y ($s_y = 1$). This guaranteed that the algorithm would look for an optimization step in adjacent pixels without decreasing the step size which meant, that it would not optimize for half pixel sized steps. On the other hand, the step size for brightness s_b was allowed to divide its value by a factor of two each time no decrease in the functional could be obtained. Therefore, a relatively large initial step size ($s_b = 100$), which was more than 10% of the total brightness value, was chosen as starting step size. For the first few iterations, the change of brightness b_i occurred rapidly so that all molecules that initially possessed the same starting brightness b_0 would quickly diverge to their individual brightness values. Thereafter, the lack of optimization potential with this large parameter forces the step size to be decreased. Choosing a large step size at the beginning of the optimization can be regarded as counter-acting the incorrect assumption of equal brightness. After 50 iteration steps, the final result parameter x_{final}, y_{final}, and b_{final} were exported as text files and were carefully filtered according to certain criteria which are explained in the following paragraph.

All single molecule localization techniques require some kind of sorting mechanism that exclude certain events from their final localization list. Some techniques confirm that the bleaching step occurs within certain boundaries.[158] Other techniques apply a brightness window that exclude signals above or below an expected brightness value.[154] In the course of this section, three criteria were applied in order to evaluate the single molecule's localizations. First, all localizations were removed that were too close to other localizations or too close to the image border, i. e. closer than the Abbe limit.[71] This was an attempt to avoid signals that may hide underneath two overlapping signals. Second, fluorescence peaks were excluded if they were too bright because excessively large intensity may be a consequence from two fluorophores at exactly the same position. This criterion was mathematically enforced by a percentage value. The molecule's brightness was averaged for all molecules within the sample excerpt excluding those that did not meet criterion one. Then, the upper border was calculated by adding the difference between minimum and median brightness to the median brightness ($b_{\text{median}} + (b_{\text{median}} - b_{\text{min}})$). If the molecule's brightness parameter exceeded this upper border value, it was excluded from further evaluation. The last class of molecules that were removed for further evaluation were localizations that were obviously mislocated. In total, 10 fluorescence lines from different sample positions were evaluated and a summary of the rotation angle and the starting parameters that served as the AVM input is given in table 6.2 in the appendix. From the total number of 126 single molecule fittings, 24 localizations (19%) were discarded because of being too close to other localization or to the border. 26 molecules (21%) showed a final brightness above the calculated upper limit and were also removed from the evaluation. A small number of five localizations (4%) were excluded due to the last criterion. The remaining localizations that have passed all criteria tests represent single molecule localizations. The evaluated centers of the fluorescence peaks were superimposed on the averaged fluorescence intensity image and are shown in figure 4.5. To the right of each individual line, a histogram assesses the y-positions of the final localization. The number of molecules N is given for all lines separately along with the standard deviation σ that was calculated from the distribution of single molecule localizations in y-direction. Between four and eleven final single fluorescence spots were localized which

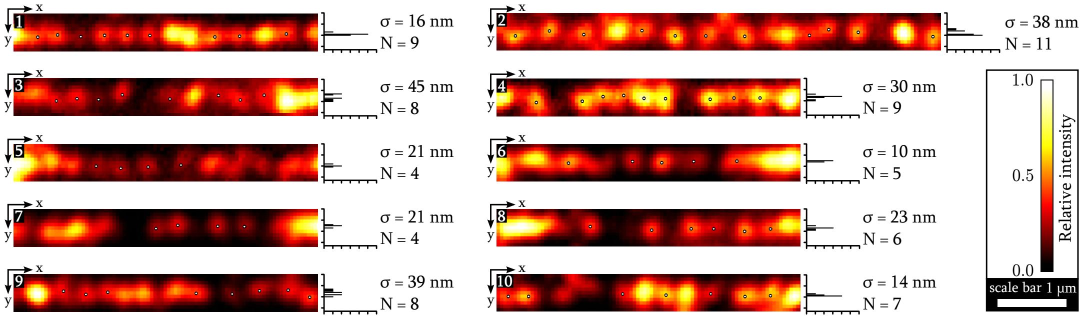

Figure 4.5: Fluorescence intensity images averaged over 80 individual frames with superimposed single molecule localizations in x and y-direction from AVM optimization for non-modulated data. Histograms show the dye distribution in y-direction for N molecules with the corresponding standard deviation σ.

showed a distribution in y-direction ranging from $\sigma = 10\,\text{nm}$ to $\sigma = 45\,\text{nm}$. Even though these values insinuate subdiffractional distribution, it is best to handle this result with care. A single localization can be considered as finding the true origin of the fluorescence signal i. e. the center of the fluorophore. The alternating-variable search algorithm pushes the optimization only in integer pixel sized step which means that the final position output is given by one pixel of (16.7[b] x 16.7) nm^2. It is then assumed that the dye lies within this pixel but it remains unknown whether it truly lies within the center or rather at the borders. As a consequence, standard deviation statistic on only a small number of molecules per fluorescence line is prone to misjudge the true dye distribution.

Increasing the statistics and fitting a distribution function to more data points certainly improves the reliability of the evaluation. The most straight-forward way of doing so would be to elongate the data excerpts for evaluation. However, this proved to be quite unfortunate and unsuccessful due to several reasons. On the one hand, the computation time increased very much which was not critical but impractical. More importantly, the second problem was due to the nature of the sample preparation and the measuring procedure. The bleaching pattern was applied to a very dense layer of fluorescence dyes which were probably even stacked to multi-layers. During the measurements with alternating excitation with and without ExPAN, the fluorescence lines needed to be bleached down to the single molecule level. The initially stacked layer height and the subsequent bleaching to the single molecule level were processes which could not be controlled perfectly. As a result, the lines did not jointly reach the required single molecule level but rather piece after piece. Therefore, only small crops could be successfully used for line evaluation.

Instead, another way of increasing the statistics was enforced by combining the individual histograms into a cumulative distribution. In order to bring all ten of them together correctly, a reference line referring to the true zero needed to be defined for the distributions. It seemed inappropriate to use the distribution itself because the data suggested that the true zero need not lie within the values (see data points for line 7, $N = 4$, $\sigma = 21$ in figure 4.5). Herein, the four localizations lie nicely in the centers of the fluorescence spots, the spots themselves, however, seem slightly shifted upwards with respect to the connecting line between the large intensity spots to the left and right. Due to this reason, it was refrained from defining the true zero from the distribution values only. Instead, the zero value was evaluated by finding the center of the averaged fluorescence intensity from the input image across the line. In order to do so, the fluorescence intensity was binned in x-direction for the entire data crop. A Gaussian distribution function was fitted to the intensity distribution and the center of the Gaussian function was considered to be the true zero. This procedure was repeated for all ten data crops and the thus obtained center value was used for overlapping the individual y-histograms. The final result

---

[b] One pixel of (50 x 50) nm^2 is oversampled by a factor of three, thus $50/3 \approx 16.7$.

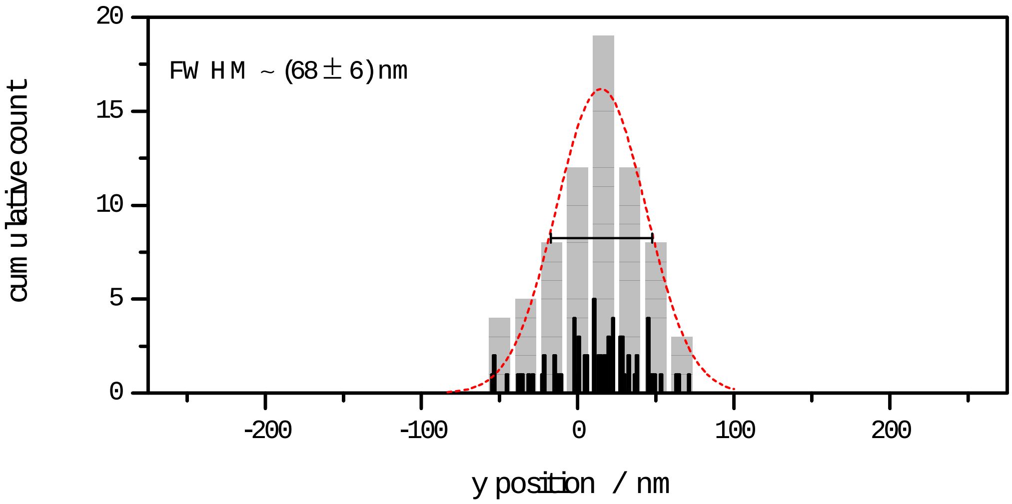

Figure 4.6: Overall position histogram assessing the y-distribution of 71 single molecule localizations within fluorescence lines obtained after AVM optimization from non-modulated data. Black bars equal the separate histograms from the individual lines in figure 4.5. Gray bars represent the cumulative count thereof with the corresponding Gaussian fitting function (red dashed curve).

for a total number of 71 molecules is shown in figure 4.6. The cumulative count (gray bars) represents the addition of the individual histogram counts (black bars). The Gaussian fitting function used to approximate the distribution in dependency of the y-position possesses a FWHM value of (68 ± 6) nm or in other words a standard deviation value of $\sigma \approx (29 \pm 3)$ nm. The evaluated line width demonstrates its sub-diffractional dimension with respect to the single molecule's emission wavelength. By using the experimental value of the wavelength at which maximum fluorescence was detected ($\lambda_{\mathrm{fl}} = 624\,\mathrm{nm}$) and a NA value of 1.4, the diffraction limit can be calculated according to equation 2.17 to be approximately 222 nm.

4.3.4 Modulated single molecule fitting using AVM

So far, it has been demonstrated that the alternating-variable search algorithm can be used for single molecule localization in spatial dimensions (x, y) using averaged fluorescence data. However, the recorded fluorescence data was measured with alternating excitation with and without ExPAN while constantly rotating the light's polarization. Therefore, the data contained a third dimension t in which the modulation of the single molecule's fluorescence signal can be observed. In the previous section, this temporal dimension was omitted by averaging the fluorescence data over a certain period of time. This section will now focus on the applicability of the alternating-variable search algorithm to single molecule localization including the temporal dimension. The goal of AVM remains to minimize the least squares functional $F(\vec{D}, \vec{p})$. In fact, both algorithms were fed with the same input data set which was obtained by cropping 80 frames from the rotated raw data and calculating a phase averaged stack thereof with a final length of 20 frames. But instead of calculating a two-dimensional averaged fluorescence intensity image, as done for the non-modulated AVM optimization, the data set $\vec{D}$ remained in its three-dimensional state composed of exactly one modulation period. This can be either regular modulation data described by a simple squared cosine function (cf. equation 2.6) or ExPAN based imaging data. The mathematical model describing modulated signals using ExPAN has been explained in detail in the theoretical section 2.1.4 for which the fundamental ExPAN function was derived (cf. equation 2.13). Before $\vec{D}$ was used for least squares minimization, the algorithm applied oversampling in x and y-direction to the data set (OS = 3). Then, an offset value was subtracted from all pixels which was chosen to be 10% larger than the overall minimum pixel value with the input data stack. The final input data set $\vec{D}$ can be regarded as an offset-corrected oversampled fluorescence intensity data stack.

In addition to the parameters x_i, y_i, and b_i, each molecule N_i is characterized by the phase φ_i and the ExPAN factor $f_{s,i}$. Herein, the phase φ can be regarded as the time at which the signal maximum appears within the temporal stack. It is given in radial units assuming that one full modulation period of 20 frames is equal to one radial round (2π). The ExPAN factor $f_{s,i}$ describes to what extent the regular fluorescence modulation peak width is narrowed. A factor of zero would mean no ExPAN modulation, factors ranging from two to eleven would indicate ExPAN signals as expected from Chapter 2. The goal of the algorithm remained the minimization of the least squares functional between $\vec{D}$ and the model stack $M(\vec{p})$. Similar to the previous non-modulated case, the initial model stack $M(\vec{p})$ was calculated by mathematically convolving initially guessed coordinates by the point spread function (PSF) assuming a starting brightness b_0 and an ExPAN factor $f_{s,0}$. Concerning the latter, whether or not the ExPAN factor was fitted, depended on the type of data. In case of ExPAN based data, the starting parameter was set to six, in case of regular modulation based data, the starting parameter was fixed at zero which simplified the ExPAN function to a simple cosine-squared expression. Due to the fact that the starting brightness parameter had proved not to be very critical for the evaluations with the non-modulated lines, it was simply set to 800 for all lines. The PSF calculated from the Richards[181] and Wolf PSF generation implementation in Fiji[126] for non-modulated AVM could also be used for the evaluation of the modulation based data. Concerning the last missing piece, the initial model stack, a small work-around was required in order to avoid creating the model stack in three dimensions by hand. Instead, only the initial parameters x_0 and φ_0 were determined and given by hand from phase dependent projections of the in y-direction binned fluorescence data. In order to do so, the fluorescence carpet was created from the 20 input frames, thus transforming the (x,y,φ)-stack into an (x,φ)-image. Similar to the procedure before, point ROIs were placed by hand into the carpet image and were subsequently transferred into an empty image. It possessed in x-direction the size of the oversampled data set $\vec{D}$ and in the remaining direction the length of the stack i. e. 20 frames. The algorithm extracted the x_0 and φ_0 values from the point ROI image and completed this two-dimensional data guess with the third dimension y_0 which was at first taken to be in the center of the image excerpt.

In contrast to the non-modulated fitting procedure, the parameter optimization for modulated data occurred in two steps. First, only the variables brightness b_0 and ExPAN factor $f_{s,0}$ were optimized while the initial position and phase of the molecules remained constant. In mathematical terms, this was achieved by setting the step sizes for the first round of iterations to zero ($s_x = 0$, $s_y = 0$, $s_\varphi = 0$) while b_0 was alternated by $s_b = 100$ and $f_{s,0}$ by $s_f = 9$ in case of ExPAN based data (otherwise s_f also equals zero). The goal of the first round of optimization was to obtain better starting parameters for the subsequent iterations of all variables simultaneously. In the second round of optimization, all parameters were addressed jointly. The step sizes for the position optimization in x and y-direction were set to the same values as previously used for the non-modulated evaluation, $s_x = 1$ and $s_y = 1$. The initial phase step size $s_\varphi = 0.5$ was given in radial units and was allowed to divide itself by a factor of two if the preceding iteration step did not lead to a minimization of the functional. The decrease in step size also applied to s_b for brightness and s_f for ExPAN factor, but not for s_x and s_y for position. After two rounds of 50 iterations each, the results were summarized in an output text file containing all final parameters x_{final}, y_{final}, φ_{final}, b_{final}, and f_{final}.

Similar to the non-modulated data evaluation procedure, certain criteria were required that excluded localizations from the final results list. Due to the underlying modulation nature of the data stack, localizations were sorted according to their distance to the stack border on the one hand, and according to their modulation signal on the other hand. Concerning the first, all localizations were removed that were too close to the image border. This was an attempt to avoid signals which were partially cut off by the chosen crop region. In contrast to the non-modulated distance criterion, molecules that were localized closer to each other than the Abbe-limit[71] were not excluded generally. Due to the modulation nature of the signals, which causes molecules of different orientation to appear at different times within the modulation stack, it was checked in the carpet-based phase dependent localization result whether the signals were correctly separated by phase. If this was the case, molecule localizations closer than the Abbe limit in x,y-direction remained in the final results list. If the phase-dependent localization did not allow a clear separation of the signals, both were removed nonetheless. In those cases, the true origin of the observed fluorescence signal might yet be a result from a single, very bright molecule. Concerning the second criterion, all localizations were superimposed to the fluorescence carpets which show the localization in x and φ dimensions. One modulation period required a

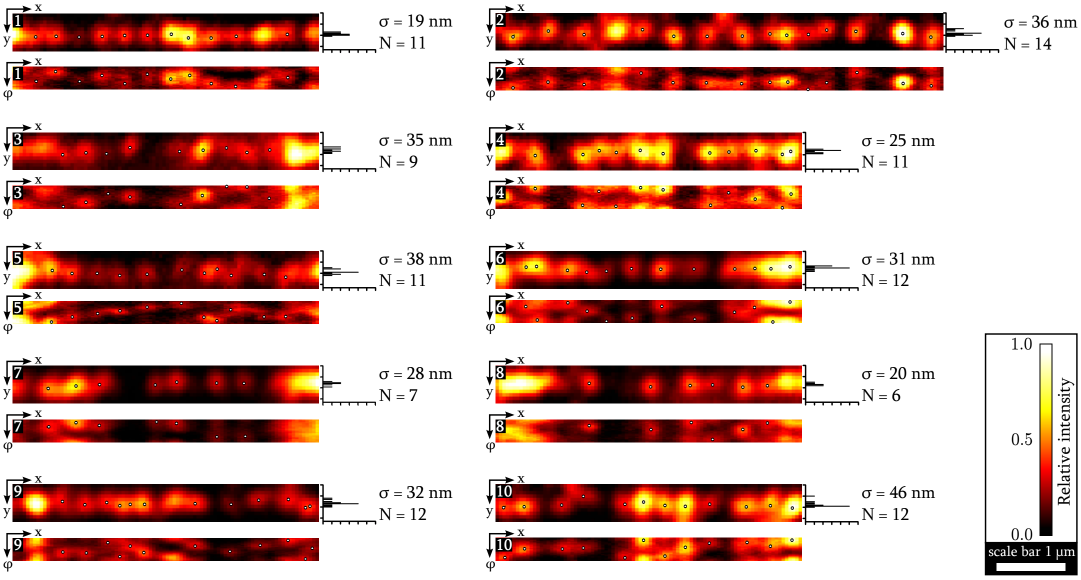

Figure 4.7: Fluorescence intensity images averaged over 80 individual frames with superimposed single molecule localizations in x and y direction from AVM optimization for modulated data with and without ExPAN. Histograms show the dye distribution in y-direction for N molecules with the corresponding standard deviation σ.

single molecule to show a continuous change from large fluorescence contribution to an emitting minimum. A lack of minimum fluorescence in the signal trace in φ-direction of the fluorescence carpets might indicate a contribution from another dye. In those cases, in order to ensure that only single molecule events make the final results list, the localizations were removed.

From a total number of 145 guessed single molecules distributed within 10 lines of fluorescence dyes, 21 localizations (15%) were discarded for being too close to the border. The initially guessed number of molecules was increased with respect to the non-modulated data because more molecules became visible in the fluorescence carpet. Some especially bright spots proved to be the results from more than one single molecule. This was one of the reasons why the brightness parameter served as a result filtering mechanism for the non-modulated data. Back to the results list for modulated data, 19 molecules (13%) were removed from the evaluation because their phase dependent separation did either not suffice to unambiguously explain the sub-diffractional distance to one another in x and y-direction or did not show an intensity minimum. After filtering the data according to the two criteria presented here, the final centers of 105 fluorescence peaks in x- and y-direction were superimposed on the averaged fluorescence intensity image and are shown in figure 4.7. Underneath each average image in distance dimensions for x and y, the fluorescence carpet with the superimposed localizations in the distance-time domain (x, φ) is given. The carpets nicely show that many molecules appeared at different times which means that the orientation distribution among the fluorescence line was quite heterogeneous. Additionally, the difference between regular modulation and ExPAN based modulation became quite apparent. Line number 5 represents a data excerpt from the very center of ExPAN illumination while ExPAN was being applied. Each of the located fluorescence spots was substantially narrowed in the temporal dimension thereby facilitating the recognition of two molecules with different phases. The molecule pair to the right of line number 9 is a powerful example for this case. In the corresponding carpet, the two rightmost fluorescence spots appear almost at opposite phases with one molecule peaking in frame 9 and the other molecule peaking in frame 18. This shift in phase sufficed in order for the algorithm to optimize the x and y-positions to be $N_1(258/20)$ and $N_2(261/19)$ in units of oversampled pixels[c]. A center-to-center distance of approximately $3.16\,\text{px}_{\text{OS}} \approx 53\,\text{nm}$ was calculated for this special pair of single molecules which is substantially below the diffraction limit of light. The evaluated distance demonstrates that the resolution limit can be overcome by introducing the temporal domain and exploiting the additional information from the modulation with and without ExPAN.

To the right of the average images, a histogram assesses the y-positions of the final localizations. Between 6 and 14 single fluorescence spots were localized within the lines, presenting a distribution in y-direction ranging from $\sigma = 25\,\text{nm}$ to $\sigma = 46\,\text{nm}$. Even though the values differ from the ones observed for the non-modulated distributions, an impression arises that the values for the modulated version tend to be slightly larger. In order to verify this impression, the individual histograms were transferred into a single distribution by correcting for the true zero of the individual fluorescence lines just as previously described. Fortunately, the zero-values as used for the non-modulated evaluation could be applied to the modulation based examination since both methods relied on the same crop from the raw data. As a brief reminder, the true center of each line was found by fitting a Gaussian distribution to the in x-direction binned fluorescence profile of the line. The final histogram showing all y-position from the 105 remaining localizations is presented in figure 4.8. Both histograms from non-modulated AVM and from modulated AVM have in common, that their y-distribution is slightly shifted to the right. This might indicate that the chosen method for bringing the individual histograms together is disadvantageous. The possibility exists that the desired true center of the line is not given correctly by the fluorescence intensity profile plot through the line. Assuming that regions of very bright intensity result from a very high density of fluorescence dyes, it cannot be ruled out that a stacked pile of dyes bends to one side, which would influence the evaluation of the true center negatively. The shift to the right is smaller than the size of one oversampled pixel i. e. smaller than 16.7 nm. For five out of ten lines or in other words for 53 out of 105 localizations, the evaluated zero value caused the individual histogram to be shifted to the right with respect to the center of the individual histogram. As an alternative to the zero value from the averaged fluorescence intensity, one could also calculate

---

[c] Oversampled pixels posses the size of $(16.7 \text{ x } 16.7\,\text{nm})^2$.

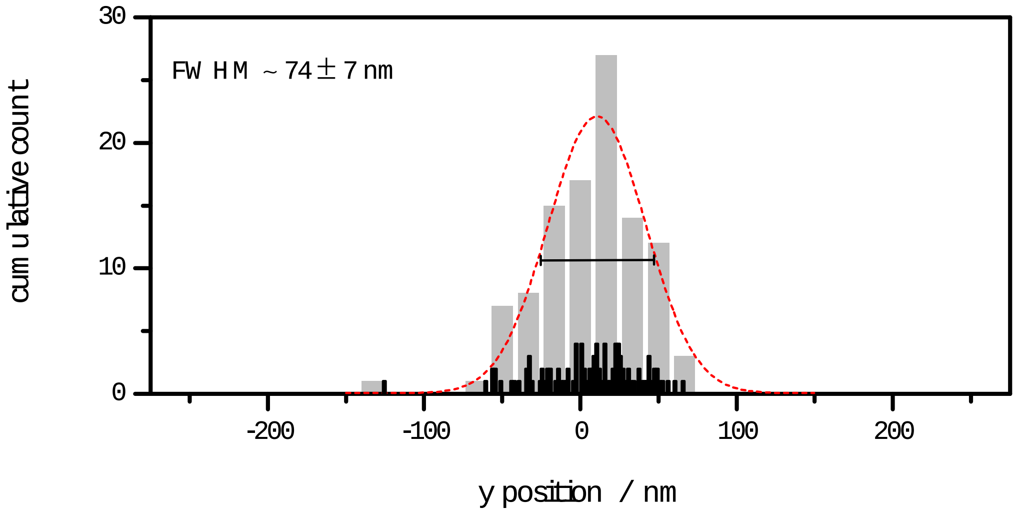

Figure 4.8: Overall position histogram assessing the *y*-distribution of 105 single molecule localizations within fluorescence lines obtained after AVM optimization from modulated data. Black bars equal the separate histograms from the individual lines in figure 4.7. Gray bars represent the cumulative count thereof with the corresponding Gaussian fitting function (red dashed curve).

the average value of the localization positions and use this value as zeroing method. By shifting the individual histograms exactly by the average *y*-position, the final distribution is expected to be smallest. As previously explained however, taking a zeroing value from within the distribution itself seemed inappropriate because of the possibility that the final distribution is intrinsically narrowed. All in all, even though the fluorescence intensity might not yield the perfectly true zero position of the line, this method does not narrow the distribution artificially which is the reason why it remained the method of choice.

The distribution for the modulated AVM evaluation for 105 molecules is slightly broader than the distribution for the non-modulated AVM evaluation for 71 molecules. However, the histogram statistics for the latter of FWHM $\approx (68 \pm 6)$ nm do not substantially differ from the statistics for the modulated case in which the FWHM was evaluated to be approximately (74 ± 7) nm. The results were on the same order of magnitude and provide evidence that the width of the fluorescence lines created by interference lithography were on sub-diffractional scales. One could argue that both histograms do not rely on the same number of molecules which cannot be compared directly, which is true for the evaluation so far. In an attempt to address this minor problem, the initial localization output list from the AVM optimization procedure of the modulation data with and without ExPAN was looked at from another perspective. Without looking at any further criteria, the results list was examined with respect to the localized molecules for the non-modulated procedure. As one can already tell from the superimposed localization spots on the averaged fluorescence intensity images by eye, all molecules obtained for the non-modulated AVM (cf. figure 4.5) have also been found in the modulated AVM evaluation (cf. figure 4.7). This means that the modulation based data evaluation provides more data points than with regular single molecule localization only, while maintaining the quality of the statistical assessment of the line width. Nonetheless, by removing all molecules from the list that have been added on the basis of the modulation information, the final localization list was restrained to include only those localizations that had been evaluated for the non-modulated data only. The final histogram of 71 localizations is shown in figure 4.9. Again, the distribution looks quite similar to the previous cases and again reveals a sub-diffraction line width. The value for the FWHM, being approximately (63 ± 7) nm, is only infinitesimally smaller than for the non-modulated case (68 ± 6) nm. The major conclusion that can be drawn from these evaluations is that the dye distribution within the fluorescence lines possesses sub-diffractional dimensions. This means that interference lithography applied on a fluorescent photoresist can be used to create structures of sub-diffractional dimensions.

It was shown that the evaluation of the negative image can be conducted from a pure single molecule approach by localizing individual molecules in x and y-dimensions. The method at hand comprised optimization of an inverse problem by minimizing a least squares functional using an alternating-variable search method. The evaluation was extended to the temporal domain by introducing the single molecule fluorescence modulation principle with and without ExPAN. The data excerpts so far were chosen to be as sparse as possible with a very low density of fluorescence molecules in order to guarantee single molecule events to occur. Some selected examples have already provided insight into the separation capability when using temporal fluorescence modulation. The following section will take a closer look at these capabilities and will explore the benefits and boundaries from

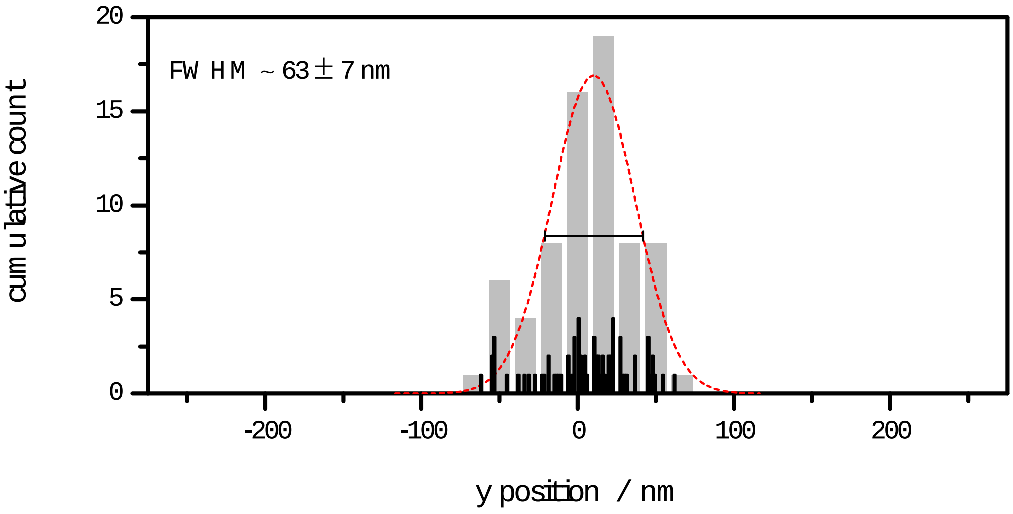

Figure 4.9: Overall position histogram after AVM optimization from modulated data assessing the y-distribution of the same 71 single molecule localizations as obtained after AVM optimization from non-modulated data.

applying ExPAN to the fluorescence lines at higher dye densities.

4.3.5 Line width characterization at higher densities

In the selected examples so far, the lines have been illuminated according to the measurement scheme shown in table 4.2 using alternating excitation with and without modulation in combination with and without ExPAN. In fact, this allowed additional, controllable bleaching until single molecule density was achieved. From this low density regime, the lines widths have been shown to possess sub-diffractional dimensions in y-direction. The distribution of the y-positions was shown to be quite narrow which makes the fluorescence lines appear as a pearl necklace composed of single fluorescent spots. Herein, the dyes extend in x-direction with arbitrary distance to one another with only a small deviation in y. This special line-up made the sample perfectly suitable for a study of the separability of molecule pairs which possess a distance below the diffraction limit of light.

As already mentioned, the measurement pattern switched between modulation and no modulation mode and excitation with and without ExPAN. Figure 4.10 presents a fluorescence carpet (x, t) from a chosen line of dyes under the influence of the measurement cycle. Herein, black passages correspond to times in which an electronically controlled beam shutter hindered the sample from illumination at times when the rotation system was being turned on or off. The dark zones separate blocks of excitation without modulation from passages with modulation in which a highly repetitive fluorescence pattern became apparent. In the non-modulation block, fluorescence intensity showed almost a constant level throughout the entire passage. The white region of interest (ROI) highlights an exemplary trace which is shown below the carpet. The effect that ExPAN forces upon the fluorescence signal of a single dye can be clearly identified around 20 s. The width of the fluorescence peaks is substantially narrowed compared to regular modulation which means that photo-selection is more restricted using ExPAN. Due to precisely this feature, it was expected that ExPAN should be capable of distinguishing more single molecules than it is already possible with regular modulation. The separability of single molecule pairs by regular modulation depends on the distance between the emitters and the difference in orientation i. e. the angle between their transition dipole moments. With decreasing distance and decreasing orientation difference the separation becomes increasingly hindered.

In order to further investigate the optical separability of single molecule signals using ExPAN, several carpets from various lines of the negative image were investigated. The examples presented in figure 4.11 demonstrate a successive increase in performance. The data crops show three consecutive sections in which the ExPAN excitation part in the middle is preceded and followed by regular modulation blocks. The ExPAN section lasts from

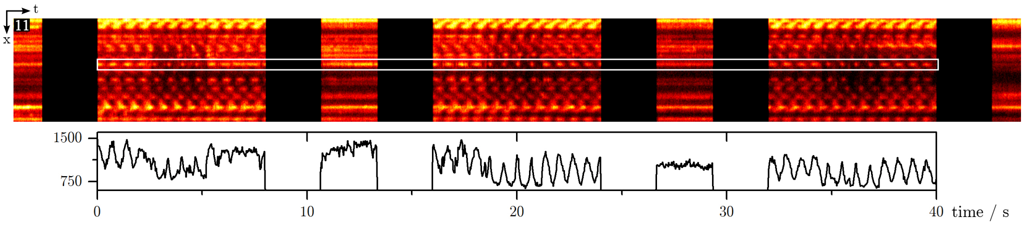

Figure 4.10: Fluorescence carpet (x,t) with corresponding intensity trace.

frame 78 to 157 or in other words from time 2.6 s to 5.23 s. The first carpet from line 12 reveals a modulation structure in the ExPAN section with very defined and narrow peaks when looking at the time trace. The fluorescence intensity peak maxima are highlighted in different colors and were assigned their corresponding frame number. The blue sequence of frames 82, 103, 122, and 143 and the orange sequence of frames 92, 112, 131, and 151 nicely corroborate the desired modulation frequency which was expected to be 20 frames per period. By calculating the difference between the frames from two consecutive signals (orange minus blue), the average frame distance was estimated to be (9 ± 1) frames which corresponds to a difference in orientation of approximately $(81 \pm 9)°$. Even though the shift in x-direction of the signal is not calculated mathematically, by looking at the fluorescence spots in the carpet it appears as if they vary at maximum by one to two pixels in x. In either case, this matches sub-diffractional dimensions with one pixel being 50 nm in size.

The next two examples, line 13 and 14, show single molecule pairs with decreasing differences in orientation. From the blue and orange peaks in line 13, the average frame distance was estimated to be (8 ± 1) frames which corresponds to a difference in orientation of approximately $(72 \pm 9)°$. From the blue and orange peaks in line 14, an average frame distance of (3 ± 1) frames and a difference in orientation of approximately $(27 \pm 9)°$ were obtained. The latter example represents the technical limit of this thesis with respect to the optical separability of single molecule pairs on the basis of temporal separation without mathematical fitting. In order to distinguish two peaks from one another in the temporal dimension, the peaks have to be separated by at least one intensity minimum either identifiable by eye or within the intensity trace. This fluorescence microscopy set-up controlled the rotation speed of the polarized light by the camera which was set to imaging with 20 frames per modulation period. In other words, one full modulation period of 180° is divided into 20 pieces which means that each frame records an angle range of 9°. Therefore, if one intensity minimum frame is required in-between two maximums, the smallest difference of orientation that is accessible with this set-up remains 18°. However, special care is required when interpreting signal minimums since the fluorescence data is noisy and minimums frequently appear without meaning anything. In those cases, the repetitive feature of the modulation is beneficial because it facilitates identifying true

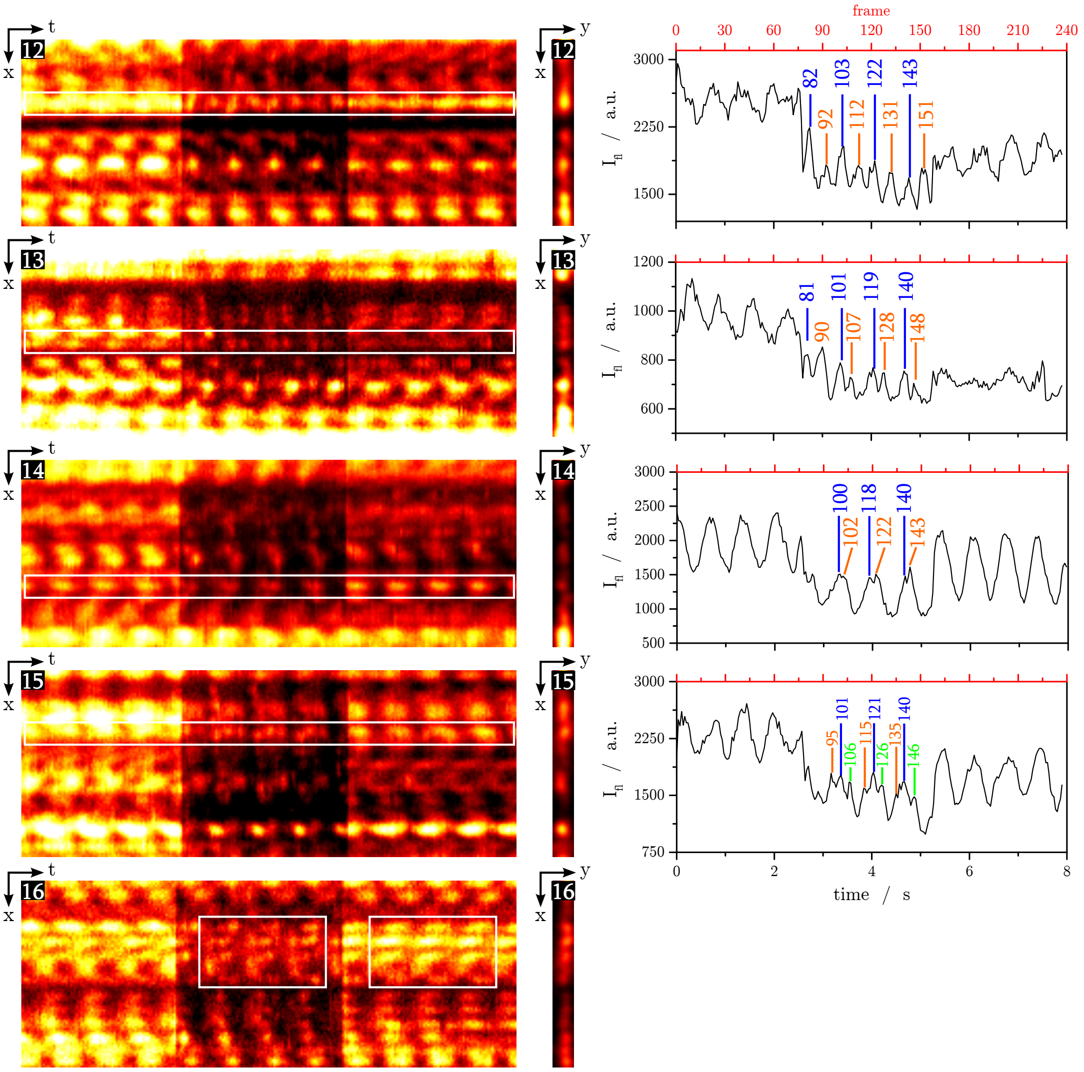

Figure 4.11: Qualitative single molecule separation from fluorescence carpets (x,t) and corresponding intensity traces using ExPAN. Peak maxima belonging to the same molecule are highlighted in equal colors. Fluorescence images (x,y) averaged over 80 individual frames from the ExPAN region.

peak patterns. In contrast to noise, true modulation features repeat themselves as long as the dyes do not suffer from photo-bleaching or entering dark states.

The second last fluorescence carpet from line 15 is a prominent example for the capability of ExPAN modulation. The white ROI clearly identifies three consecutive fluorescence spots in the ExPAN region. In the fluorescence trace, the different peak maxima were assigned three different colors, orange, blue, and light green. Even in this trace, all sequences of frames (orange: 95, 115, and 135; blue: 101, 121, and 140; light green: 106, 126, and 146), nicely corroborate the desired modulation frequency of 20 frames per period. The difference in orientation from the average frame distance was calculated as previously done. The results can be summarized as follows: the orange peaks are followed by the blue peaks with a distance of (6 ± 1) frames which are themselves followed by the light green peaks after (5 ± 1) frames. This means that the orientation difference between the first two dyes can be approximated to be (51 ± 9)° while the second and third molecules differ in orientation by (48 ± 9)°. Accordingly, the overall orientation difference from the first to the third molecule is (99 ± 9)°. Due to the fact that this angle is larger than 90° is can also be assumed that the difference is rather (81 ± 9)° which would have been the case for the calculation if the third molecule was assumed to be followed by the first. No matter how the relative angle differences are expressed in the end, this example shows that ExPAN can be used to distinguish three single molecules which are in very close proximity to one another.

So far, all examples of single molecule pairs or trios in this section have been separated according to their phase information. In order to assess, if the distance between the molecules is on sub-diffractional dimensions, a qualitative look at the fluorescence intensity average images in figure 4.11 of the lines was taken. By looking at the averaged fluorescence spots from which the fluorescence traces had been taken, it could be investigated for all examples if the signal average was broadened in x- or y-direction. As long as the spots would not show substantial peak broadening in either direction, it can be assumed that the molecules are located on sub-diffractional scales with respect to one another. All examples presented here did not show peak broadening in either direction which allows the assumption that all single molecule pairs and trios were located on sub-diffractional scales.

In sections 4.3.3 and 4.3.4, the line widths have been shown to provide a FWHM value of approximately 70 nm in y-direction at the single molecule level. The question arises whether the sub-diffractional dimension still accounts for line widths if the dye density is slightly increased. It is expected that the dimension remains the same for higher dye densities and in order to provide evidence for this assumption, a quantitative assessment of the single molecule positions can be obtained by mathematical means. A very straightforward and simple Gaussian fitting was applied to the trio from line 15 in figure 4.11. A region of 10 by 10 pixels including those three molecules from within the ExPAN section was cropped from the raw data. From this excerpt two fluorescence carpets were calculated. The first one was derived by binning in y-direction which leaves the final carpet to be in dimensions of x and φ. The second carpet was obtained by binning in x-direction so that the final carpet shows y and φ. A fluorescence intensity image averaged over 60 frames and the corresponding carpets are shown in figure 4.12. Due to the fact that the fluorescence spots were sufficiently separated in the temporal domain, rectangular ROIs were defined around the individual spots. By plotting the intensity distribution in x- or y-direction and subsequent fitting of a Gaussian function, the positions of the single molecules were obtained. Because each molecule was imaged three consecutive times, three pairs of localizations were obtained. For the first molecule for example, the posi-

Table 4.4: Single molecule localization summary from Gaussian fitting of three molecules each localized in three consecutive periods. x and y position values are given in units of pixel (1 pixel = 50 nm). SE means standard error.

molecule	localization	$x\,/\,\mathrm{px}$	$\mathrm{SE}_x\,/\,\mathrm{px}$	$y\,/\,\mathrm{px}$	$\mathrm{SE}_y\,/\,\mathrm{px}$
1	1	3.8	0.5	5.22	0.05
1	2	3.3	0.2	5.08	0.03
1	3	2.9	0.1	5.04	0.03
2	1	5.4	0.2	5.26	0.02
2	2	5.10	0.07	5.50	0.04
2	3	5.24	0.06	5.38	0.05
3	1	4.89	0.05	4.93	0.05
3	2	4.8	0.2	4.82	0.03
3	3	4.6	0.1	4.70	0.06

tions were obtained to be $x = (3.8 \pm 0.5)\,\mathrm{px}$ and $y = (5.22 \pm 0.05)\,\mathrm{px}$. A summary of all Gaussian fitting results is given in table 4.4. What can be learned from these values is that the previous assumption that the shift in x-direction would not exceed one pixel is confirmed. Additionally, the evaluation of the y-position provided results with much smaller error values than for the x-position. The standard deviation calculated from the y-positions was obtained to be $\sigma_y = 0.3\,\mathrm{px}$ which equals a value of $\sigma_y = 15\,\mathrm{nm}$ when taking the pixel size into account. A standard deviation value of 15 nm corresponds to a FWHM value of 35 nm and nicely supports the sub-diffractional dimension even at slightly higher dye densities.

A more sophisticated method for exploring the y-distribution of the dyes has already been reported in this thesis. By using the alternating-variable search method (AVM) for modulated fluorescence data, the positions x and y for a certain number of emitters N are optimized by taking the molecule's brightness b, the molecule's phase φ, and the molecule's ExPAN factor f_s into account. A detailed description of the principles of AVM have been given in section 4.1.3 while section 4.3.4 focused on the explicit application of AVM to modulated fluorescence data. The algorithm was not yet designed to evaluate more than one signal period, therefore, the data set of the three molecule example was split into three consecutive parts which were evaluated individually and which contained one signal triplet each. The PSF according to Richards[181] and Wolf from former evaluations was used. The initial molecule guess list was created in the same manner as previously described and the same list was used for all three evaluations. The initial starting parameters were set as follows: brightness $b_0 = 700$ and ExPAN factor $f_{s,0} = 6$ with the step sizes $s_x = s_y = 1$, $s_b = 100$, $s_\varphi = 0.5$, and $s_f = 9$. In the first round of 50 iterations, the variables x_0, y_0, and φ_0 were kept constant while only optimizing b_0 and $f_{s,0}$. In the second round of 50 iterations, all parameters were optimized simultaneously. The three final results lists were combined to a single file and the x_{final}, y_{final}, and φ_{final} values were superimposed on the corresponding fluorescence carpets, as shown in figure 4.12. The spot centers which have been drawn on the intensity image averaged over all three periods (x,y-image) were obtained by calculating the average position in x- and y-direction from the three localizations of the molecule from different periods. To the right of the y-φ-carpet, a histogram shows the distribution of the y-position of the nine localizations. Herein, a standard deviation value of $\sigma \approx 17$ nm corresponding to a FWHM value of approximately 40 nm is reported. Both methods provide evidence that the line widths remain on sub-diffractional scales when dye density was increased.

A different representation of the phase-based carpet data is shown to the right of figure 4.12. Herein, a color-code was applied as depicted by the color-scale bar. The phase scale was assigned to be composed of three colors, namely blue, green, and red. This color-coded representation emphasized the phase-based separability of the underlying three molecule example especially in the carpet images. Superimposing the AVM optimization results of the single molecules onto the carpet images allows the conclusion that the localization results are in good agreement with the position data (x, y) as well as the phase data (φ). The molecule colored in blue appears to be leftmost in the y-binned fluorescence carpet (x, φ) while the molecule colored in green is localized to the right. In the x-binned fluorescence carpet, the molecule in green colors seems to be slightly shifted downwards with respect to the blue and red center. In an attempt to trace back the phase information in the average intensity image (x, y), the phase coordinate in the x,y image was calculated by Fourier transformation. Herein, the fluorescence spot reveals three phase domains with blue to the left and green to the right encircling the red spot when looking in x-direction. The y-position of the green spot appears to be shifted slightly downwards

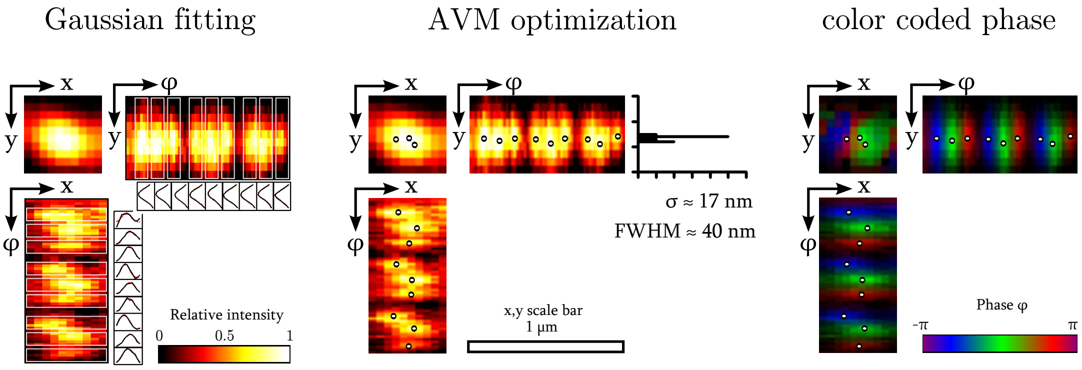

Figure 4.12: Fluorescence intensity images averaged over 60 frames (x, y) and corresponding fluorescence carpets for x-binned data (y, φ) and for y-binned data (x, φ). To the left, Gaussian fitting of the white rectangular ROIs is shown. In the center, AVM optimization results of the single molecule localizations are superimposed on the images. The histogram assesses the y-position distribution. To the right, the color-coded representation of the phase data is shown.

which is in very good agreement with the observations from the carpets. By calculating the average x- and y-positions for the leftmost molecule (blue) and the rightmost spot (green), the distance can be calculated using the Pythagorean theorem. In units of pixels, a distance of (1.9 ± 0.3) px was obtained which equals (95 ± 15) nm. The distance calculations from green to red and from blue to red resulted in values of (35 ± 10) nm and (75 ± 15) nm, respectively. This example nicely demonstrates the additional information that is contained and introduced to the fluorescence data by polarization modulation in combination with one way of extracting the information by the AVM optimization algorithm.

The underlying excerpt was of course very promising since the phase separation was clearly visible in advance of the evaluation and since the trio of molecules was quite isolated from surrounding dyes. However, this can be considered a quite unique dye combination with respect to the position and the phase. In most cases, the dye distribution along the fluorescence line cannot be expected to be equally orderly, as the fluorescence line 16 in figure 4.11 reveals. The rectangular white ROI in the ExPAN section highlights a region in which the repetitive pattern is visible by eye. Unfortunately, the distribution of dyes along the fluorescence line (in x-direction) in combination with the different phases hinders the evaluation by simple time traces. For this example, it was simply not possible to find a rectangular ROI which enclosed a separated set of dyes because each attempted ROI included further fluorescence contribution from the left or right. In other words, this example did not provide the possibility to draw conclusions from the phase information without looking at the position information at the same time. Due to these reasons, the only possible way to evaluate this excerpt was by means of simultaneous treatment of position and phase which was provided by the AVM optimization algorithm.

For line number 16 in figure 4.11, the AVM algorithm was equipped with the PSF according to Richards[181] and Wolf, a data crop of 20 frames (1 modulation period) from the ExPAN region, a molecule guess list of 10 estimated molecules, and the starting parameters brightness $b_0 = 200$, and ExPAN factor $f_{s,0} = 6$ with the step sizes $s_x = s_y = 1$, $s_b = 100$, $s_\varphi = 0.5$, and $s_f = 9$. Again, two rounds of 50 iterations each were performed, in which first only b_0 and $f_{s,0}$ were optimized, followed by round two in which, all parameters were optimized simultaneously. The final results list was saved and used to superimpose the x_{final}, y_{final}, and φ_{final} values onto the corresponding fluorescence carpet and intensity average image, as shown in figure 4.13. To the left, the ExPAN based fluorescence intensity image (x, y) averaged over 20 frames and its corresponding carpet image (x, φ) binned in y-direction are shown. The histogram assesses the y-distribution of the localized spots. For a number of 10 molecules, a standard deviation of $\sigma = 40$ nm corresponding to a FWHM value of 95 nm was calculated. This value is far below the diffraction limit of light which supports the previously stated results of creating line widths

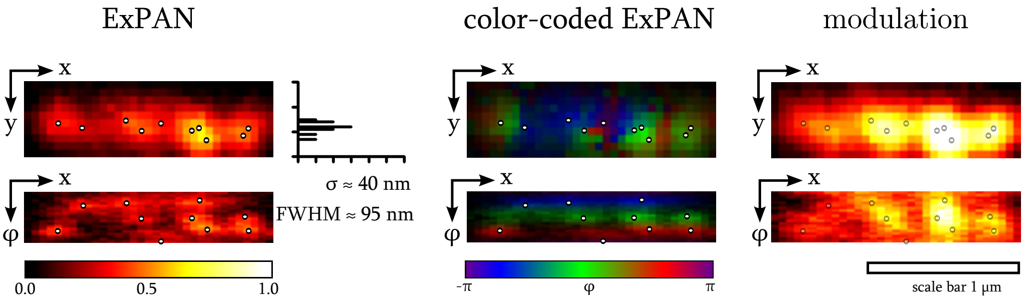

Figure 4.13: AVM optimization results from ExPAN section on line 16 (white ROI in figure 4.11). Dots evaluated from the ExPAN section are superimposed to the left on the ExPAN based x, y fluorescence intensity image averaged over 20 frames and corresponding fluorescence carpets (x, φ), to the center on the the color-coded representation of the phase data, and to the right on the regular modulation based x, y fluorescence intensity image averaged over 20 frames following the ExPAN section and corresponding fluorescence carpet (x, φ).

with sub-diffractional dimensions by interference lithography. The current results were obtained for increased dye densities or in other words at earlier stages of the measuring cycles. Consequently, it is likely that the line widths possess sub-diffractional dimensions all along and do not exclusively occur at single molecule dye densities. The localized centers of the fluorescence dyes seemed to suit the average image (x, y) as well as the phase carpet (x, φ) quite well for the evaluated ExPAN regime. The dye density obviously exceeded the temporal separability available by regular modulation, as shown to the right in figure 4.13. The superimposed dots were not obtained by AVM evaluation since it was not possible to identify a proper molecule guess. The dots shown here are the same ones obtained from the ExPAN section. It seems as if the x, y image from regular modulation is simply more intense that the the x, y image from ExPAN. In fact, the intensity image averaged over 20 frames from the regular modulation section was cropped from the block following the ExPAN section. It can be assumed that the same number of molecules was actively emitting fluorescence. However, without ExPAN more photons are emitted as fluorescence which is why the x, y-images from regular modulation usually appeared brighter than throughout the preceding ExPAN section. The eight rightmost dots are definitely not distinguishable in the regular modulation section. The two leftmost localization points are an example in which two individual signals can also be distinguished in the phase dependent projection of regular modulation data. Herein, the phase difference is approximately 90° at a distance of approximately 200 nm. The color-coded representation of the ExPAN data in the middle of figure 4.13 again separated the phase information by the aid of three colors, blue, red, and green. Due to the fact that the phase distribution is not homogeneous, some dots appear in the center of colored spots while other dots appear in-between colors. In this example, it is helpful to take the two preceding signal periods into account. Figure 4.14 shows the fluorescence carpets of the intensity image and the color-coded image. To the bottom, the localization results from the period from which the data was derived were superimposed on the carpet. The transparent dots on the two preceding periods can be used as a guide to the eye for recognizing the repetitive pattern of the ExPAN modulation.

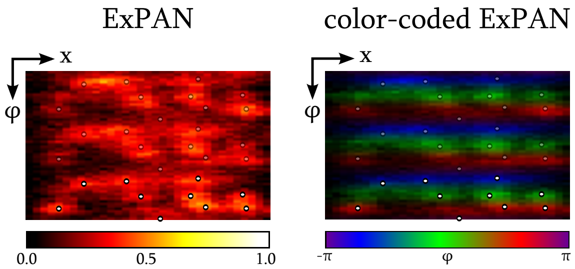

Figure 4.14: AVM optimization results evaluated from the ExPAN section are superimposed to the left on the ExPAN based fluorescence carpet (x, φ) and to the right on the the color-coded representation of the phase data. Evaluated dots from the bottom ExPAN period are superimposed as transparent dots to the two preceding periods.

All in all, the evaluation of the negative image by means of single molecule localization using an AVM algorithm strongly indicated that the interference lithography set-up was capable of creating patterns in fluorescent sample on sub-diffractional dimensions. The lines have been shown to stem from single fluorescent dyes whose distributions were smaller than the diffraction limit of light, for small dye densities in the single molecule regime as well as for higher densities. In the future, this fluorescence lithography set-up might be extended to multi-beam interference creating even more complex patterns in fluorescent samples. It is imaginable that the interference lithography set-up may be tuned to minimum fringe periodicity p with a light source of very small wavelengths, thus resulting in negative images of fluorescent lines whose distance is below the diffraction limit of light with respect to the fluorescence emission wavelength of the dye used. These kind of patterns could potentially be used as fluorescence calibration standards for determining the resolving capacity of the fluorescence microscope.

5 Summary

In the course of this thesis, a novel approach for creating a regular and well-defined interference pattern in the focal plane of a fluorescence microscope was presented. This set-up was used as an interference lithography set-up in which a structured illumination pattern was bleached into a fluorescent photoresist. The structured illumination pattern was created by two-beam interference in the focal plane of a self-built epi-fluorescence configured microscope. Herein, beam separation in the excitation path was accomplished by two Wollaston prisms each installed into a rotation mount. One part of this thesis focused on the thorough characterization of the interference pattern with respect to the orientation of the Wollaston prisms. The most interesting and important aspects ahead of the microscope's objective (beam distance at the back focal plane (d_{obj}), beam intensity (I), and polarization orientation (θ)) were related to the most interesting and important aspects from imaging the interference pattern (fringe periodicity (p), fringe orientation (β)). It was found that the fringe line orientation β was a direct consequence of the spot position (X/Y) at the back focal plane of the microscope's objective. Additionally, it was shown that the fringe periodicity p was linearly proportional to the inverse of the spot distance at the back aperture of the objective d_{obj}. All information was used to derive mathematical equations that described the dependency of the named aspects with respect to the orientation of the Wollaston prisms. In this manner, the resulting fringe pattern could be predicted from knowing the settings of the prisms. Since a slight change of one Wollaston prism resulted in simultaneous changes of all aspects, the equations proved especially helpful in finding the correct angles of rotation of the Wollaston prisms (ω_1, ω_2) for a desired pattern structure. The use of two Wollaston prisms proved to be quite advantageous since the change of position and distance of the spots on the back focal plane did not require new beam alignment. Consequently, the fringe pattern observed in the sample plane was easily tunable. All in all, the knowledge gained from the mathematical equations facilitated designing a specific line pattern with desired characteristics for interference lithography.

By means of interference lithography, a fringe pattern was bleached into a self-built fluorescent photoresist. Fluorescent dyes which were located within or close to the nodes of the interference pattern remained intact thus creating a negative imprint of the pattern within the photoresist. The negative image consisted of defined lines of fluorescent dyes that had survived the bleaching procedure. A second part of this thesis focused on the characterization of the negative image with special emphasis on the line widths of the nodes. The lines were characterized by single molecule localization using an alternating variable search method (AVM) based optimization algorithm. Briefly, the algorithm iteratively searched for the best set of parameters $\vec{p}$ for which a given model function $M(\vec{p})$ approximated the recorded data $\vec{D}$ best. In mathematical terms, this was done by minimizing the least squares functional between the model function and the recorded data. Two different types of recorded fluorescence data were used, namely non-modulated and modulated fluorescence data. The principle of fluorescence modulation was introduced in the first part of this thesis. By constantly turning the polarization plane of the linearly polarized excitation light, the fluorescence signal from an individual emitter was modulated in the temporal domain.[8] The photo-selection of regular modulation was described by a squared cosine function and was shown to be substantially narrowed by applying a second de-excitation beam whose polarization plane was oriented perpendicular with respect to the excitation light's polarization vector. The effect named excitation polarization angle narrowing (ExPAN)[10][8] was shown to increase the photo-selectivity of excitation. In this thesis, ExPAN was demonstrated using CW de-excitation (715 nm) and pulsed excitation (568 nm).

The fluorescence data for the AVM algorithm for the evaluation of the node width of the negative image was recorded by using fluorescence modulation with and without ExPAN. AVM results on individual lines provided evidence that the centers of the individually localized dyes were distributed on sub-diffractional dimensions for non-modulated data as well as for modulated fluorescence. The FWHM values of each distribution ($\sim$ 70 nm) were much smaller than the diffraction limit of light with respect to the emission maximum wavelength of 624 nm of the dye used (ATTO 590). It was shown that the temporal domain allowed the distinction of individual molecule pairs or trios which were located in close proximity to one another. Due to the fact that ExPAN increased the photo-selection of excitation, the temporal separability with ExPAN was enhanced with respect to regular modulation.

6 Appendix

Theoretical spot positions after two consecutive Wollaston prisms:

In section 3.3.1, equations have been derived for describing the spot position of the separated beam after single Wollaston prisms. In the following section 3.3.2, these finding have been merged into a theoretical description of the position of one of the four spots of the separated beams after two consecutive Wollaston prisms ($X_{1\text{-}1}/Y_{1\text{-}1}$). A complete list of the theoretical description of all spot positions after two consecutive Wollaston prisms is given here:

$$\begin{aligned}
X_{1\text{-}1} &= \cos(\omega_1 - 44^\circ) + \cos(\omega_2 + 101.5^\circ) \\
Y_{1\text{-}1} &= \sin(\omega_1 - 44^\circ) + \sin(\omega_2 + 101.5^\circ) \\
X_{1\text{-}2} &= \cos(\omega_1 - 44^\circ) + \cos(\omega_2 + 281.5^\circ) \\
Y_{1\text{-}2} &= \sin(\omega_1 - 44^\circ) + \sin(\omega_2 + 281.5^\circ) \\
X_{2\text{-}1} &= \cos(\omega_1 + 136^\circ) + \cos(\omega_2 + 101.5^\circ) \\
Y_{2\text{-}1} &= \sin(\omega_1 + 136^\circ) + \sin(\omega_2 + 101.5^\circ) \\
X_{2\text{-}2} &= \cos(\omega_1 + 136^\circ) + \cos(\omega_2 + 281.5^\circ) \\
Y_{2\text{-}2} &= \sin(\omega_1 + 136^\circ) + \sin(\omega_2 + 281.5^\circ)
\end{aligned} \tag{6.1}$$

Theoretical spot intensities at the back aperture of the objective:

In section 3.3.1, equations have been derived for describing the spot intensities of the separated beam after single Wollaston prisms. In the following section 3.3.2, these finding have been merged into a theoretical description of the spot intensity of one of the four spots of the separated beams at the back aperture of the objective i. e. after two consecutive Wollaston prisms and a polarizing beam splitter ($I_{1\text{-}1}$). A complete list of the theoretical description of all spot intensities at the back aperture is given here:

$$\begin{aligned}
I_{1\text{-}1} &= I_0 \cdot \cos^2(\omega_1 - 44^\circ) \cdot \cos^2(\omega_2 + 101.5^\circ - \theta_1(\omega_1)) \cdot \cos^2(\theta_{1\text{-}1}(\omega_2)) \\
I_{1\text{-}2} &= I_0 \cdot \cos^2(\omega_1 - 44^\circ) \cdot \cos^2(\omega_2 + 191.5^\circ - \theta_1(\omega_1)) \cdot \cos^2(\theta_{1\text{-}2}(\omega_2)) \\
I_{2\text{-}1} &= I_0 \cdot \cos^2(\omega_1 + 46^\circ) \cdot \cos^2(\omega_2 + 101.5^\circ - \theta_2(\omega_1)) \cdot \cos^2(\theta_{2\text{-}1}(\omega_2)) \\
I_{2\text{-}2} &= I_0 \cdot \cos^2(\omega_1 + 46^\circ) \cdot \cos^2(\omega_2 + 191.5^\circ - \theta_2(\omega_1)) \cdot \cos^2(\theta_{2\text{-}2}(\omega_2))
\end{aligned} \tag{6.2}$$

Calibration of experimental spot distance values with theoretical values:

In order to relate the theoretical spot distance values obtained by equation 3.25 to the experimental values d_{obj}, a linear fitting function is used:

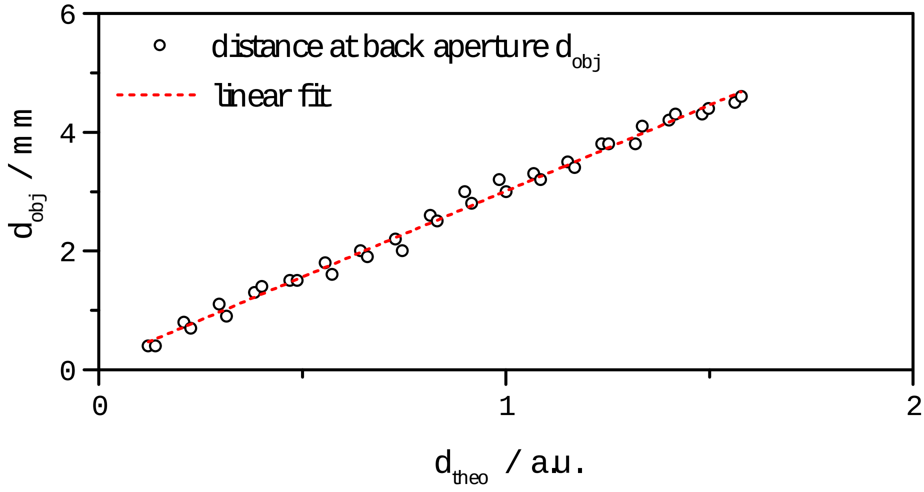

Figure 6.1: Plot of spot distance at objective d_{obj} over theoretical spot distance d_{theo}. The slope of the linear fitting function is (2.9 ± 0.1)mm/a.u..

Full step-by-step derivation of equation 3.27:

Starting point is the expression for $I_{1\text{-}1}$ in equation 3.22 and $I_{2\text{-}2}$ in equation 6.2. Herein, $\theta_1(\omega_1)$ and $\theta_2(\omega_1)$ are replaced by inserting equation 3.14 and $\theta_{1\text{-}1}(\omega_2)$ and $\theta_{2\text{-}2}(\omega_2)$ are replaced by equation 3.20.

$$
\begin{aligned}
1 = \frac{I_{2\text{-}2}}{I_{1\text{-}1}} &= \frac{I_0}{I_0} \cdot \frac{\cos^2(\omega_1 + 46^\circ)}{\cos^2(\omega_1 - 44^\circ)} \cdot \frac{\cos^2(\omega_2 - \omega_1 + 145.5^\circ)}{\cos^2(\omega_2 - \omega_1 + 145.5^\circ)} \\
&\cdot \frac{\cos^2(\omega_2 + 191.5^\circ)}{\cos^2(\omega_2 + 101.5^\circ)} \\
&\text{substition } x = \omega_1 - 44^\circ \text{ und } y = \omega_2 + 101.5^\circ \\
&= \frac{\cos^2(x + \pi/2)}{\cos^2(x)} \cdot \frac{\cos^2(y + \pi/2)}{\cos^2(y)} \\
&= \frac{\sin^2(x)}{\cos^2(x)} \cdot \frac{\sin^2(y)}{\cos^2(y)} \\
&= \tan^2(x) \cdot \tan^2(y) \\
&= \tan^2(\omega_1 - 44^\circ) \cdot \tan^2(\omega_2 + 101.5^\circ)
\end{aligned} \tag{6.3}
$$

Overview of data processing parameters for each evaluated line:

Table 6.1: The evaluated line number is related to the measurement number (cf. Table 4.3), the degree of rotation δ applied to the raw data, and the crop size.

line number	measurement number	δ	crop size
1	1	32.36°	90 x 11
2	1	32.36°	132 x 11
3	2	32.21°	90 x 11
4	2	32.21°	90 x 11
5	3	32.40°	90 x 11
6	4	32.39°	90 x 11
7	5	32.25°	90 x 11
8	5	32.25°	90 x 11
9	5	32.25°	90 x 11
10	5	32.25°	90 x 11
11	3	32.40°	90 x 11
12	5	32.25°	90 x 11
13	5	32.25°	90 x 11
14	5	32.25°	90 x 11
15	4	32.39°	10 x 10
16	3	32.40°	90 x 10

Overview of important parameters for AVM data evaluation:

Table 6.2: AVM parameters for non-modulated and modulated data evaluation for a total number of molecules N_{total} using an offset and initially given parameters for brightness b_0 and ExPAN factor $f_{s,0}$. N_{final} represents the final number of molecules that passed all selection criteria as described in sections 4.3.3 and 4.3.4.

	non-modulated AVM				modulated AVM				
line number	offset	b_0	N_{total}	N_{final}	offset	b_0	$f_{s,0}$	N_{total}	N_{final}
1	262	900	14	9	392	800	0	15	11
2	168	1000	16	11	332	800	0	17	14
3	291	900	13	8	481	800	0	14	9
4	203	1000	11	9	384	800	6	12	11
5	170	230	13	4	217	800	6	18	11
6	574	1700	13	5	787	800	0	15	12
7	328	900	11	4	456	800	0	15	7
8	434	1100	11	6	579	800	0	13	6
9	278	950	13	8	423	800	6	17	12
10	175	900	11	7	291	800	0	12	12
15	-	-	-	-	1100	700	6	3	3
16	-	-	-	-	330	200	6	10	10

7 Bibliography

[1] E. Hecht. "Optik." Fourth edition, Oldenbourg, München, **2002**.

[2] M. Young. "Optics and lasers: including fibers and optical waveguides." Fifth completely rev. and enl. edition, Springer, Berlin, **2000**.

[3] A. Lasagni, C. Holzapfel, F. Mücklich. "Periodic pattern formation of intermetallic phases with long range order by laser interference metallurgy." *Advanced Engineering Materials* **7** (6) 487-492, **2005**.

[4] A. Lasagni *et al.* "Periodic surface structuring of metals by laser interference metallurgy as a new fabrication method of textured solar selective absorbers." *Advanced Engineering Materials* **8** (6) 580-584, **2006**.

[5] A. Lasagni *et al.* "Laser interference metallurgy: A new method for periodic surface microstructure design on multilayered metallic thin films." *Applied Surface Science* **253** (19) 8070-8074, **2007**.

[6] S. Fujita *et al.* "Periodical nanostructure fabrication using electron interference fringes produced by scanning interference electron microscope." *Applied Physics Letters* **66** (20) 2754-2756, **1995**.

[7] K. Ogai *et al.* "Nanofabrication of grating and dot patterns by electron holographic lithography." *Applied Physics Letters* **66** (12) 1560-1562, **1995**.

[8] N. Hafi *et al.* "Fluorescence nanoscopy by polarization modulation and polarization angle narrowing" *Nature Methods* **11** (5) 579-584, **2014**.

[9] N. Hafi *et al.* Reply to "Polarization modulation adds little additional information to super-resolution fluorescence microscopy" *Nature Methods* **13** (1) 8-9, **2016**.

[10] M. Grunwald. "Molekulare Orientierung als Kontrastmechanismus in der Fluoreszenzmikroskopie und konfokale Multidetektor-Scanning-Mikroskopie." Dissertation, Göttingen, Georg-August Universität, **2015**.

[11] B. Korel. "Automated software test data generation." *IEEE Transactions on Software Engineering* **16** (8) 870-879, **1990**.

[12] S. Andersson-Engels *et al.* "In vivo fluorescence imaging for tissue diagnostics." *Physics in Medicine and Biology* **42** (5) 815-824, **2013**.

[13] M. Monici. "Cell and tissue autofluorescence research and diagnostic applications." *Biotechnology Annual Review* **11** 227-256, **2005**.

[14] C.-S. Chin *et al.* "Nonhybrid, finished microbial genome assemblies from long-read SMRT sequencing data." *Nature Methods* **10** (6) 563-569, **2013**.

[15] A. H. M. van Vliet. "Next generation sequencing of microbial transcriptomes: challenges and opportunities." *FEMS Microbiology Letters* **302** (1) 1-7, **2010**.

[16] J. F. Thompson, K. E. Steinmann. "Single molecule sequencing with a HeliScope genetic analysis system." Current Protocols in Molecular Biology, John Wiley & Sons, **2010**.

[17] H. S. Rye *et al.* "Fluorometric assay using dimeric dyes for double- and single-stranded DNA and RNA with picogram sensitivity." *Analytical Biochemistry* **208** (1) 144-150, **1993**.

[18] B. Huang, H. Babcock, X. Zhuang. "Breaking the diffraction barrier: Super-resolution imaging of cells." *Cell* **143** (7) 1047-1058, **2010**.

[19] J. R. Lakowicz. "Principles in fluorescence spectroscopy." Springer, New York, **2006**.

[20] A. Yildiz *et al.* "Myosin V walks hand-over-hand: Single fluorophore imaging with 1.5 nm localization." *Science* **300** (5628) 2061-2065, **2003**.

[21] O. Shimomura, F. H. Johnson, Y. Saiga. "Extraction, purification, and properties of aequorin, a bioluminescent protein from the luminous hydromedusan, Aequorea." *Journal of Cellular and Comparative Physiology* **59** (3) 223-239 **1962**.

[22] M. Ormö *et al.* "Crystal Structure of the *Aequorea victoria* Green Fuorescent Protein." *Science* **273**, 1392-1395 **1996**.

[23] D. C. Prasher *et al.* "Primary structure of the *Aequorea victoria* green-fluorescent protein." *Gene* **111** (2) 229-233 **1992**.

[24] G.-J. Kremers *et al.* "Fluorescence proteins at a glance." *Journal of Cell Science* **124** (2) 157-160 **2010**.

[25] N. C. Shaner *et al.* "Improved monomeric red, orange and yellow fluorescent proteins derived from Discosoma sp. red fluorescent protein." *Nature Biotechnology* **22** (12) 1567-1572 **2004**.

[26] M. Chalfie *et al.* "Green Fluorescent protein as a marker for gene expression." *Science* **263**, 802-805 **1994**.

[27] J. Lippincott-Schwartz. "Development and use of fluorescent protein markers in living cells." *Science* **300** (5616) 87-91 **2003**.

[28] "The Nobel Prize in Chemistry 2008". Nobelprize.org. Nobel Media AB 2014. <http://www.nobelprize.org/nobel_prizes/chemistry/laureates/2008/> Web. 6 Jan 2017.

[29] P. J. Walla. "Modern Biophysical Chemistry: Detection and analysis of biomolecules." Second Edition, Wiley-VCH, Weinheim, **2014**.

[30] A. Wehling, P. J. Walla. "A two-photon excitatin study on the role of carotenod dark states in the regulatin of plant photosynthesis." *Photosynthesis Research* **90** (2) 101-110, **2006**.

[31] S. Bode *et al.* "On the regulation of photosynthesis by excitonic interactions between carotenoids and chlorophylls." *Proceedings of the National Academy of Sciences* **106** (30) 12311-12316, **2009**.

[32] C. P. Holleboom *et al.* "Carotenoid-chlorophyll coupling and fluorescence quenching correlate with protein packing density in grana-thylakoids." *Journal of Physical Chemistry B* **117** (38) 11022-11030, **2013**.

[33] O. Laporte, W. F. Meggers. "Some rules of spectral structure." *Journal of the Optical Society of America* **11** (5) 459-463, **1925**.

[34] A. Jablonski. "Über den Mechanismus der Photolumineszens von Farbstoffphosphoren." *Zeitschrift für Physik* **94** (1) 38-46, **1935**.

[35] P. Atkins, J. de Paula. "Physical Chemistry." Ninth edition, Oxford University Press, Oxford, New York, **2010**.

[36] H. Haken, H. C. Wolf. "Molekülphysik und Quantenchemie: Einführung in die experimentellen und theoretischen Grundlagen." Fünfte Auflage, Springer, Berlin, **2006**.

[37] B. Valeur, M. N. Berberan-Santos. "Molecular fluorescence: Principles and applications." Second Edition, Wiley-VCH, Weinheim, **2012**.

[38] A. Einstein. "Zur Quantentheorie der Strahlung." *Physikalische Zeitschrift* **18** 121-128, **1917**.

[39] T. H. Maiman. "Stimulated optical radiation in ruby." *Nature* **187** (4736) 493-494, **1960**.

[40] A. L. Schawlow, C. H. Townes. "Infrared and optical masers." *Physical Reviews* **112** (6) 1940-1949, **1958**.

[41] S. W. Hell, J. Wichmann. "Breaking the diffraction resolution limit by stimulated emission: stimulated-emission-depletion fluorescence microscopy." *Optics Letters* **19** (11) 780-782, **1994**.

[42] T. A. Klar *et al.* "Fluorescence microscopy with diffration resolution barrier broken by stimulated emission." *Proceedings of the National Academy of Sciences* **97** (15) 8206-8210, **2000**.

[43] A. C. Albrecht. "Polarizations and assignments of transitions: The method of photoselection." *Journal of Molecular Spectroscopy* **6**, 84-108, **1961**.

[44] F. Güttler *et al.* "Single molecule spectroscopy: fluorescence excitation spectra with polarized light." *Journal of Luminescence* **56** (1-6) 29-38, **1993**.

[45] T. Ha *et al.* "Single molecule dynamics studied by polarization modulation." *Physical Review Letters* **77** (19) 3979-3982, **1996**.

[46] F. Bestvater *et al.* "Two-photon fluorescence absorption and emission spectra of dyes relevant for cell imaging." *Journal of Microscopy* **208** (2) 108-115, **2002**.

[47] R. Y. Tsien, L. Ernst, A. Waggoner. "Fluorophores for confocal microscopy: Photophysics and Photochemistry." in: J. B. Pawley (ed.). "Handbook of biological confocal microscopy." Third Edition, Springer, New York, **2006**.

[48] M. Sauer, J. Hofkens, J. Enderlein. "Handbook of fluorescence spectroscopy and imaging." Wiley-VCH, Weinheim, **2011**.

[49] F. L. Arbeloa, V. M. Martínez. "Orientation of absorbed dyes in the interlayer space of clays. 2 Fluorescence polarization of rhodamine 6G in laponite films." *Chemistry of Materials* **18** (6) 1407-1416, **2006**.

[50] A. Chmyrov *et al.* "Characterization of new fluorescent labels for ultra-high resolution microscopy." *Photochemical and Photobiological Sciences* **7** (11) 1378-1385, **2008**.

[51] "ATTO-TEC GmbH webpage" Fluorescent labels and dyes. <https://www.atto-tec.com/attotecshop/product_info.php?info=p105_atto-590.html> (28 Jan 2017).

[52] A. Mokhir *et al.* "Fluorescent sensor for Cu2+ with a tunable emission wavelength." *Inorganic Chemistry* **44** (16) 5661-5666, **2005**.

[53] U. Bhattacharjee *et al.* "Tryptophan and ATTO 590: Mutual fluorescence quenching and exciplex formation." *Journal of Physical Chemistry B* **118** (29) 8471-8477, **2014**.

[54] M. Heilemann *et al.* "Super-resolution imaging with small organic fluorophores." *Angewandte Chemie International Edition* **48** (37) 6903-6908, **2009**.

[55] V. Chirmanov *et al.* "Distance-dependent energy transfer between Ga_2O_3 nanocrystal defect states and conjugated organic fluorophores in hybrid white-light-emitting nanophosphors." *Journal of Physical Chemistry C* **119** (10) 5687-5696, **2015**.

[56] J. C. White, L. Stryer. "Photostability studies of phycobiliprotein fluorescent labels." *Analytical Biochemistry* **161** (2) 442-452, **1986**.

[57] T. J. Gould, V. V. Verkhusha, S. T. Hess. "Imaging biological structures with fluorescence photoactivation localization microscopy." *Nature Protocols* **4** (3) 291-308, **2009**.

[58] E. Betzig, R. J. Chichester. "Single molecules observed by near-field scanning optical microscopy." *Science* **262** (5138) 1422-1425, **1993**.

[59] A. V. Agronskaia, L. Tertoolen, H. C. Gerritsen. "High frame rate fluorescence lifetime imaging." *Journal of Physics D: Applied Physics* **36** (14) 1655-1662, **2003**.

[60] C. R. J. Sheppard, D. M. Shotton. "Confocal laser scanning microscopy." BIOS Scientific Publishers, Oxford, **1997**.

[61] N. C. Shaner, G. H. Patterson, M. W. Davidson. "Advances in fluorescent protein technology." *Journal of Cell Science* **120** (24) 4247-4260, **2007**.

[62] G. B. Airy. "On the diffraction of an object-glass with circular aperture." *Transactions of the Cambridge Philosophical Society* **5** (3) 283-291, **1835**.

[63] E. Kreyszig. "Advanced engineering mathematics." Tenth edition, John Wiley & Sons, New York, **2011**.

[64] Lord Rayleigh. "Investigation in optics, with special reference to the spectroscope." *Philosophical Magazine and Journal of Science*, Fifth series **8** (49) 261-274, **1879**.

[65] A. S. Backer *et al.* "A bisected pupil for studying single-molecule orientational dynamics and its application to three-dimensional super-resolution microscopy." *Applied Physics Letters* **104** (19) 193701, **2014**.

[66] G. D. Marshall *et al.* "Coherence properties of a single dipole emitter in diamond." *New Journal of Physics* **13** (5) 055016, **2011**.

[67] D. Patra, I. Gregor, J. Enderlein. "Image analysis of defocused single-molecule images for three-dimensional molecule orientation studies." *The Journal of Physical Chemistry A* **108** (33) 6836-6841, **2004**.

[68] D. Baddeley, M. B. Cannell, C. Soeller. "Three-dimensional sub-100 nm super-resolution imaging of biological samples using a phase ramp in the objective pupil." *Nano Research* **4** (6) 589-598, **2011**.

[69] S. Jia, J. C. Vaughan, X. Zhuang. "Isotropic three-dimensional super-resolution imaging with a self-bending point spread function." *Nature Photonics* **8** (4) 302-306, **2014**.

[70] S. R. P. Pavani *et al.* "Three-dimensional, single-molecule fluorescence imaging beyond the diffraction limit by using a double-helix point spread function." *Proceedings of the National Academy of Sciences* **106** (9) 2995-2999, **2009**.

[71] E. Abbe. "Beiträge zur Theorie des Mikroskops und der mikroskopischen Wahrnehmung." *Archiv für mikroskopische Anatomie* **9** (1) 413-418, **1873**.

[72] J. H. Burge, C. Zhao, M. B. Dubin. "Use of the Abbe sine condition to quantify alignment aberrations in optical imaging systems." *International Optical Design Conference and Optical Fabrication and Testing*, Optical Society of America, **2010**.

[73] A. Edelstein *et al.* "Computer Control of Microscopes Using µManager." *Current Protocols in Molecular Biology*. **2010**. 92:14.20:14.20.1-14.20.17.

[74] H. Kautsky. "Quenching of luminescence by oxygen." *Transactions of the Faraday Society* **35**, 216-219, **1939**.

[75] K. D. Weston *et al.* "Room-temperature fluorescence characteristics of single dye molecules adsorbed on a glass surface." *Journal of Chemical Physics* **109** (17) 7474-7485, **1998**.

[76] T. Basche, S. Kummer, C. Brauchle. "Direct spectroscopic observation of quantum jumps of a single molecule." *Nature* **373** (6510) 132-134, **1995**.

[77] J. Bernard *et al.* "Photon bunching in the fluorescence from single molecules: A probe for intersystem crossing." *Journal of Chemical Physics* **98** (2) 850-859, **1993**.

[78] B. A. Smith, H. M. McConnell. "Determination of molecular motion in membranes using periodic pattern photobleaching." *Proceedings of the National Academy of Sciences* **75** (6) 2759-2763, **1978**.

[79] D. Axelrod *et al.* "Mobility measurement by analysis of fluorescence photobleaching recovery kinetics." *Biophysical Journal* **16** (9) 1055-1069, **1976**.

[80] R. Peters *et al.* "A microfluorimetric study of translational diffusion in erythrocyte membranes." *Biochimica et Biophysica Acta* **367** (3) 282-294, **1974**.

[81] K. Jacobson *et al.* "Measurement of the lateral mobility of cell surface components in single living cells by fluorescence recovery after photobleaching." *Journal of Supramolecular Structure* **5** (4) 565-576, **1976**.

[82] J. Davoust, P. F. Devaux, L. Leger. "Fringe pattern photobleaching, a new method for the measurement of transport coefficients of biological macromolecules." *The EMBO Journal* **1** (10) 1233-1238, **1982**.

[83] R. M. Weis *et al.* "Stimulation of fluorescence in a small contact region between rat basophil leukemia cells and planar lipid membrane targets by coherent evanescent radiation." *Journal of Biological Chemistry* **257** (11) 6440-6445, **1982**.

[84] H. M. Munnelly *et al.* "Interferometric fringe fluorescence photobleaching recovery interrogates entire cell surfaces." *Biophysical Journal* **75** (2) 1131-1138, **1998**.

[85] B. Bailey *et al.* "Enhancement of axial resolution in fluorescence microscopy by standing-wave excitation." *Nature* **366** (6450) 44-48 **1993**.

[86] S. Hell, E. H. K. Stelzer. "Fundamental improvement of resolution with a 4Pi-confocal fluorescence microscope using two-photon excitation." *Optics Communications* **93** (5) 277-282 **1992**.

[87] M. G. L. Gustafsson, D. A. Agard, J. W. Sedat. "Sevenfold improvement of axial resolution in 3D wide-field microscopy using two objective lenses." *SPIE Pro-*

ceedings **2412**, Three-Dimensional Microscopy: Image Acquisition and Processing II, 147-156 **1995**.

[88] M. G. L. Gustafsson. "Extended resolution fluorescence microscopy." *Current Opinion in Structural Biology* **9** (5) 627-628 **1999**.

[89] M. A. A. Neil, R. Juškaitis, T. Wilson . "Method of obtaining optical sectioning by using structured light in a conventional microscope." *Optics Letters* **22** (24) 1905-1907 **1997**.

[90] R. Heintzmann, C. G. Cremer. "I5M: 3D widefield light microscopy with better than 100 nm axial resolution." *SPIE Proceedings* **3568**, Optical Biopsies and Microscopic Techniques III, 185-196 **1999**.

[91] M. G. L. Gustafsson. "Surpassing the lateral resolution limit by a factor of two using structured illumination microscopy." *Journal of Microscopy* **198** (2) 82-87 **2000**.

[92] J. T. Frohn, H. F. Knapp, A. Stemmer. "True optical resolution beyond the Rayleigh limit achieved by standing wave illumination." *Proceedings of the National Academy of Sciences* **97** (13) 7232-7236 **2000**.

[93] E. Chung, D. Kim, P. T. So. "Extended resolution wide-field optical imaging: objective-launched standing-wave total internal reflection fluorescence microscopy." *Optics Letters* **31** (7) 945-947, **2006**.

[94] J. T. Frohn, H. F. Knapp, A. Stemmer. "Three-dimensional resolution enhancement in fluorescence microscopy by harmonic excitation." *Optics Letters* **26** (11) 828-830 **2001**.

[95] L. Shao *et al*. "I5S: Wide-field light microscopy with 100-nm-scale resolution in three dimensions." *Biophysical Journal* **94** (12) 4971-4983 **2008**.

[96] H. Verveer, V. Verbeek, J. van Vliet. "Theory of confocal fluorescence imaging in the programmable array microscope (PAM)." *Journal of Microscopy* **189** (3) 192-198 **1998**.

[97] J. Bewersdorf, R. Pick, S. W. Hell. "Multifocal multiphoton microscopy." *Optics Letters* **23** (9) 655-657 **1998**.

[98] A. Egner, S. W. Hell. "Time multiplexing and parallelization in mulitfocal multiphoton microscopy." *Journal of the Optical Society of America A* **17** (7) 1192-1201 **2000**.

[99] M. Minsky. "Microscopy apparatus." *US Patent* 3013467 A, **1961**.

[100] D. Dan *et al*. "DMD-based LED-illumination super-resolution and optical sectioning microscopy." *Scientific Reports* **3**, 1116-1112 **2013**.

[101] D. Xu *et al.* "Fast optical sectioning obtained by structured illumination microscopy using a digital mirror device." *Journal of Biomedical Optics* **18** (6) 060503 **2013**.

[102] J. Qian *et al.* "Full-color structured illumination optical sectioning microscopy." *Scientific Reports* **5**, (6) 14513-14522 **2015**.

[103] R. Fiolka *et al.* "Time-lapse two-color 3D imaging of live cells with doubled resolution using structured illumination." *Proceedings of the National Academy of Sciences* **109** (14) 5311-5315 **2012**.

[104] R. Förster *et al.* "Simple structured illumination microscope setup with high acquisition speed by using a spatial light modulator." *Optics Express* **22** (17) 20663-20677 **2014**.

[105] B. C. Chen *et al.* "Lattice light-sheet microscopy: Imaging molecules to embryos at high spatiotemporal resolution." *Science* **346** (6208) 1257998 **2014**.

[106] P. Křížek, I. Raška, G. M. Hagen. "Flexible structured illumination microscope with a programmable illumination array." *Optics Express* **20** (22) 24585-24599 **2012**.

[107] R. Heintzmann, T. M. Jovin, C. Cremer. "Saturated patterned excitation microscopy: a concept for optical resolution improvement." *Journal of the Optical Society of America A* **19** (8) 1599-1609 **2002**.

[108] M. G. L. Gustafsson, D. A. Agard, J. W. Sedat. "I5M: 3D widefield light microscopy with better than 100 nm axial resolution." *Journal of Microscopy* **195** (1) 10-16 **1999**.

[109] F. Lanni, D. L. Taylor, A. S. Waggoner. "Standing wave luminescence microscopy." *US Patent* 4621911 A, **1986**.

[110] F. Lanni, D. L. Taylor, B. Bailey. "Field synthesis and optical sectioning for standing wave microscopy." *US Patent* 5394268 A, **1995**.

[111] A. V. Failla *et al.* "Nanosizing of fluorescent objects by spatially modulated illumination microscopy." *Applied Optics* **41** (34) 7275-7283 **2002**.

[112] A. Neumann, Y. Kuznetsova, S. R. J. Brueck. "Structured illumination for the extension of imaging interferometric microscopy." *Optics Express* **16** (10) 6785-6793 **2008**.

[113] E. Engel *et al.* "Creating $\lambda/3$ focal holes with a Mach-Zehnder interferometer." *Applied Physics B* **77** (1) 11-17 **2003**.

[114] S. K. Davis, J. Christopher. "Using two-photon standing waves and patterned photobleaching to measure diffusion from nanometers to microns in biological systems." *Review of Scientific Instruments* **73** (5) 2128-2135 **2002**.

[115] R. Heintzmann *et al.* "Structured illumination methods." in: J. B. Pawley (ed.). "Handbook of biological confocal microscopy." Third Edition, Springer, New York, **2006**.

[116] M. G. L. Gustafsson. "Nonlinear structured-illumination microscopy: Wide-field fluorescence imaging with theoretically unlimited resolution." *Proceedings of the National Academy of Sciences of the United States of America* **102** (37) 13081-13086 **2005**.

[117] A. R. Harvey, D. W. Fletcher-Holmes. "Birefringent Fourier-transform imaging spectrometer." *Optics Express* **12** (22) 5368-5374 **2004**.

[118] H. Choi *et al.* "Depth resolved hyperspectral imaging spectrometer based on structured light illumination and Fourier transform interferometry." *Biomedical Optics Express* **5** (10) 3494-3507 **2014**.

[119] O. Nairz, M. Arndt, A. Zeilinger. "Quantum interference experiments with large molecules." *American Journal of Physics* **71** (4) 319-325 **2003**.

[120] J. E. Greivenkamp. "Chapter 2: Interference." in: M. Bass, E. W. van Stryland, D. R. Williams, W. L. Wolfe. "Handbook of Optics: Fundamentals, Techniques, and Design." Second Edition, McGraw-Hill, New York, **1995**.

[121] G. M. Burrow, T. K. Gaylord. "Multi-beam interference advances and applications: Nano-electronics, photonic crystals, metamaterials, subwavelength structures, optical trapping, and biomedical structures." *Micromachines* **2** (2) 221-257 **2011**.

[122] M. Gu, P. C. Ke, X. S. Gan. "Trapping force by a high numerical-aperture microscope objective obeying the sine condition." *Review of Scientific Instruments* **68** (10) 3666-3668 **1997**.

[123] S.-U. Hwang, Y.-Gu. Lee. "Simulation of an oil immersion objective lens: A simplified ray-optics model considering Abbe's sine condition." *Optics Express* **16** (26) 21170-21183 **2008**.

[124] L. Bergmann, C. Schaefer. "Lehrbuch der Experimentalphysik Bd.3: Optik: Wellen- und Teilchenoptik." 10. Auflage, de Gruyter, Berlin, **2004**.

[125] M. Born, E. Wolf. "Principles of Optics: Electromagnetic Theory of Propagation, Interference and Diffraction of Light." Seventh extended edition, Cambridge University Press, Cambridge, **1999**.

[126] J. Schindelin *et al.* "Fiji: an open-source platform for biological-image analysis." *Nature Methods* **9** (7) 676-682, **2012**.

[127] D. Axelrod, T. P. Burghardt, N. L. Thompson. "Total internal reflection fluorescence." *Annual Review of Biophysics and Bioengineering* **13** (1) 247-268, **1984**.

[128] C. Axelrod. "Total internal reflection fluorescence microscopy in cell biology." *Traffic* **2** (11) 764-774, **2001**.

[129] G. E. Cragg, P. T. C. So. "Lateral resolution enhancement with standing evanescent waves." *Optics Letters* **25** (1) 46-48, **2000**.

[130] P. T. C. So, H.-S. Kwon, C. Y. Dong. "Resolution enhancement in standing-wave total internal reflection microscopy: a point-spread-function engineering approach." *Journal of the Optical Society of America A* **18** (11) 2833-2845, **2001**.

[131] A. Rohrbach. "Observing secretory granules with a multiangle evanescent wave microscope." *Biophysical Journal* **78** (5) 2641-2654, **2000**.

[132] A. L. Mattheyses, D. Axelrod. "Direct measurement of the evanescent field profile produced by objective-based total internal reflection fluorescence." *Journal of Biomedical Optics* **11** (1) 014006, **2006**.

[133] D. S. Johnson, J. K. Jaiswal, S. Simon. "Total internal reflection fluorescence (TIRF) microscopy illuminator for improved imaging of cell surface events." Current Protocols in Cytometry, John Wiley & Sons, Inc., 2012.

[134] A. L. Mattheyses, K. Shaw, D. Axelrod. "Effective elimination of laser interference fringing in fluorescence microscopy by spinning azimuthal incidence angle." *Microscopy Research and Technique* **69** (8) 642-647, **2006**.

[135] M. van't Hoff, V. de Sars, M. Oheim. "A programmable light engine for quantitative single molecule TIRF and HILO imaging." *Optics Express* **16** (22) 18495-18504, **2008**.

[136] R. Fiolka *et al.* "Even illumination in total internal reflection fluorescence microscopy using laser light." *Microscopy Research and Technique* **71** (1) 45-50, **2008**.

[137] P. E. Ciddor. "Refractive index of air: new equations for the visible and near infrared." *Applied Optics* **35** (9) 1566-1573 **1996**.

[138] "The Nobel Prize in Chemistry 2014". Nobelprize.org. Nobel Media AB 2014. <http://www.nobelprize.org/nobel_prizes/chemistry/laureates/2014/> Web. 3 Jan 2017.

[139] C. Eggeling *et al.* "Lens-based fluorescence nanoscopy." *Quarterly Reviews of Biophysics* **48** (2) 178-243 **2015**.

[140] S. Hell, E. H. K. Stelzer. "Properties of a 4Pi confocal fluorescence microscope." *Journal of the Optical Society of America A* **9** (12) 2159-2166 **1992**.

[141] S. W. Hell *et al.* "Confocal microscopy with and increased detection aperture: type-B 4Pi confocal micrsocopy." *Optics Letters* **19** (3) 222-224 **1994**.

[142] J. Bewersdorf, R. Schmidt, S. W. Hell. "Comparison of I5M and 4Pi-microscopy." *Journal of Microscopy* **222** (2) 105-117 **2006**.

[143] E. A. Ash, G. Nicholls. "Super-resolution aperture scanning microscope." *Nature* **237** (5357) 510-512 **1972**.

[144] E. Betzig *et al.* "Near field scanning optical microscopy (NSOM): Development and biophysical applications." *Biophysical Journal* **49** (1) 269-279 **1986**.

[145] B. I. de Bakker *et al.* "Nanometer-scale organization of the alpha subunits of the receptors for IL2 and IL15 in human T lymphoma cells." *Journal of Cell Science* **121** (5) 627-633 **2008**.

[146] S. W. Hell, M. Kroug. "Ground-state-depletion fluorescence microscopy: A concept for breaking the diffraction resolution limit." *Applied Physics B* **60** (5) 495-497 **1995**.

[147] S. Bretschneider, C. Eggeling, S. W. Hell. "Breaking the diffraction barrier in fluorescence microscopy by optical shelving." *Physical Review Letters* **98** (21) 218103 **2007**.

[148] J. Fölling *et al.* "Fluorescence nanoscopy by ground-state depletion and single-molecule return." *Nature Methods* **5** (211) 943-945 **2008**.

[149] S. W. Hell, M. Dyba, S. Jakobs. "Concepts for nanoscale resolution in fluorescence microscopy." *Current Opinion in Neurobiology* **14** (5) 599-609 **2004**.

[150] U. Böhm, S. W. Hell, R. Schmidt. "4Pi-RESOLFT nanoscopy." *Nature Communications* **7**, 10504 **2016**.

[151] T. Dertinger *et al.* "Fast, background-free, §D super-resolution optical fluctuation imaging (SOFI)." *Proceedings of the National Academy of Sciences* **106** (52) 22287-22292, **2009**.

[152] S. Geissbuehler, C. Dellagiacoma, T. Lasser. "Comparison between SOFI and STORM." *Biomedical Optics Express* **2** (3) 408-420, **2011**.

[153] X. Qu. "Nanometer-localized multiple single-molecule fluorescence microscopy." *Proceedings of the National Academy of Sciences* **101** (31) 11298-11303, **2004**.

[154] M. J. Rust, M. Bates, X. Zhuang. "Sub-diffraction-limit imaging by stochastic optical reconstruction microscopy (STORM)." *Nature Methods* **3** (10) 793-795, **2006**.

[155] B. Bates, B. Huang, X. Zhuang. "Super-resolution microscopy by nanoscale localization of photo-switchable fluorescent probes." *Current Opinion in Chemical Biology* **12** (5) 505-514, **2008**.

[156] S. van de Linde *et al.* "Direct stochastic optical reconstruction microscopy with standard fluorescent probes." *Nature Protocols* **6** (7) 991-1009, **2011**.

[157] K. Xu, G. Zhong, X. Zhuang. "Actin, spectrin, and associated proteins form a periodic cytoskeletal structure in axons." *Science* **339** (6118) 452-456, **2013**.

[158] E. Betzig *et al.* "Imaging intracellular fluorescent proteins at nanometer resolution." *Science* **313** (5793) 1642-1645, **2006**.

[159] S. T. Hess, T. P. K. Girirajan, M. D. Mason. "Ultra-high resolution imaging by fluorescence photoactivation localization microscopy." *Biophysical Journal* **91** (11) 4258-4272, **2006**.

[160] A. Sharonov, R. M. Hochstrasser. "Wide-field subdiffraction imaging by accumulated binding of diffusing probes." *Proceedings of the National Academy of Sciences* **103** (50) 18911-18916, **2006**.

[161] J. Keller, A. Schönle, S. W. Hell. "Efficient fluorescence inhibition patterns for RESOLFT microscopy." *Optics Express* **15** (6) 3361-3371, **2007**.

[162] P. Bingen *et al.* "Parallelized STED fluorescence nanoscopy." *Optics Express* **19** (24) 23716-23726, **2011**.

[163] F. Bergermann *et al.* "2000-fold parallelized dual-color STED fluorescence nanoscopy." *Optics Express* **23** (1) 211-223, **2015**.

[164] A. Chmyrov *et al.* "Nanoscopy with more than 100 000 'doughnuts'." *Nature Methods* **10** (8) 737-742, **2013**.

[165] R. E. Thompson, D. R. Larson, W. W. Webb. "Precise nanometer localization analysis for individual fluorescent probes." *Biophysical Journal* **82** (5) 2775-2783, **2002**.

[166] H. Deschout *et al.* "Precisely and accurately localizing single emitters in fluorescence microscopy." *Nature Methods* **11** (3) 253-266, **2013**.

[167] M. Bates *et al.* "Multicolor super-resolution imaging with photo-switchable fluorescent probes." *Science* **317** (5845) 1749-1753, **2007**.

[168] M. Fernandez-Suarez, A. Y. Ting. "Fluorescent probes for super-resolution imaging in living cells." *Nature Reviews Molecular Cell Biology* **9** (12) 929-943, **2009**.

[169] T. Brakemann *et al.* "A reversibly photoswitchable GFP-like protein with fluorescence excitation decoupled from switching." *Nature Biotechnology* **29** (10) 942-950, **2011**.

[170] D. M. Shcherbakova *et al.* "Photocontrollable fluorescent proteins for superresolution imaging." *Annual Reviews of Biophysics* **43**, 303-329, **2014**.

[171] R. C. Aster, B. Borchers, C. H. Thurber. "Parameter estimation and inverse Problems." Second Edition, Elsevier Inc., Academic Press, Boston **2013**.

[172] R. A. Fisher. "On the mathematical foundations of theoretical statistics." *Philosophical Transactions of the Royal Society of London. Series A* **222** 309-368, **1922**.

[173] A. Hald. "On the history of maximum likelihood in relation to inverse probability and least squares." *Statistical Science* **14** (2) 214-222, **1999**.

[174] A. M. Stigler. "Gauss and the invention of least squares." *The Annals of Statistics* **9** (3) 465-474, **1981**.

[175] A.-M. Legendre. "Nouvelles méthodes pour la détermination des orbites des comètes." F. Didot, Paris **1805**.

[176] C. F. Gauss. "Theoria motus corporum coelestium in sectionibus conicis solem ambientium." Perthes, Hamburg **1809**. Translation reprinted as "Theory of the motion of the heavenly bodies moving about the sun in conic sections." Little, Brown and Company, Boston **1857**.

[177] C. G. E. Boender, H. E. Romeijn. "Stochastic methods." in R. Horst (Eds.), P. M. Pardalos (Eds.). "Handbook of global optimization." Springer, Dordrecht, 829-869 **1995**.

[178] S.-P. Chen. "An alternating variable method with varying replications for simulation response optimization." *Computers & Mathematics with Applications* **48** (5) 769-778, **2004**.

[179] R. Hooke, T. A. Jeeves. "Direct search of numerical and statistical problems." *Journal of Association Computer Machinery* **8** (2) 212-229, **1961**.

[180] G. V. Reklaitis, A. Ravindran, L. M. Ragsdell. "Engineering optimization: Methods and applications." John Wiley & Sons, London **1983**.

[181] B. Richards, E. Wolf. "Electromagnetic diffraction in optical systems. II. Structure of the image field in an aplanatic system." *Proceedings of the Royal Society A* **253** (1274) 358-379, **1959**.

List of abbreviations

abs	Absorption
AVM	Alternating-variable search method
CW	Continuous wave
EMCCD	Electron-multiplying charge-coupled device
EMG	Electron multiplying gain
ExPAN	Excitation polarization angle narrowing
FFT	Fast Fourier transform
fl	Fluorescence
fpp	Frames per period
FWHM	Full width at half maximum
IC	Internal conversion
IR	Infrared
ISC	Intersystem crossing
LBO	Lithium triborate
NA	Numerical aperture
obj	Objective
OPE	One photon excitation
OPO	Optical parametric oscillator
OS	Oversampling
PSF	Point-spread-function
ROI	Region of interest
SE	Standard error
se	Stimulated emission
SNR	Signal-to-noise ratio
theo	Theoretical
TIR	Total internal reflection
TPE	Two photon excitation
UV	Ultra violet
VIS	Visible

List of mathematical symbols

Latin alphabet

a	Size of an image pixel
$\vec{A}$	Amplitude vector of linearly polarized light
b	Background noise per pixel
b_i	Brightness parameter in AVM
$\vec{B}$	Magnetic field component
c	Speed of light, $c = 2.998 \cdot 10^8$ m/s[35]
d	Resolution limit of light
d_{obj}	Distance of the interfering spots at back focal plane of objective
d_{STED}	Inner diameter of STED doughnut
D	Diameter of circular aperture
$\vec{D}$	Recorded data set
e	Elementary charge, $e = 1.602 \cdot 10^{\text{-}19}$ C[35]
E	Energy
$\vec{E}$	Electric field vector of electromagnetic wave
f	Focal length of lens
f_s	ExPAN factor
$f_{s,i}$	ExPAN factor parameter in AVM
$F(\vec{D},\vec{p})$	Least squares functional
h	Planck constant, $h = 6.626 \cdot 10^{-34}$ J s[35]
I	Intensity of light
I_s	Threshold intensity of saturation
I_n	Intensity of separated beams after a single Wollaston prism
$I_{n\text{-}m}$	Intensity of separated beams after two stacked Wollaston prisms
J_p	Photon flux intensity
k	Magnitude of $\vec{k}$
k_n	Rate constant for transition n
$\vec{k}$	Wave vector of light
L	Distance from circular aperture to diffraction pattern

$M(\vec{p})$	Model function depending on $\vec{p}$
n_r	Index of refraction
N_1	Population of first electronically excited state
N_A	Avogadro's constant, $N_A = 6.022 \cdot 10^{23}\mathrm{mol}^{-1}$[35]
N_i	Number of molecules
N_p	Number of detected photons
NA	Numerical aperture
p	Fringe periodicity of interference pattern of two intersecting plane waves
$\vec{p}$	Set of parameters for a model function M
P_n	Probability of transition
r	Radius of circular aperture
r_d	Distance from center of lens
$\vec{r}$	Three-dimensional coordinate
s_i	Initial step size in AVM optimization for parameter i
S_0	Electronic singlet ground state
S_1	First electronically excited singlet state
t	Time
T	Electronic triplet state
v	Vibrational quantum number
x_i	Position parameter x in AVM
X_n	Cartesian x coordinate of separated beams after a single Wollaston prism
$X_{n\text{-}m}$	Cartesian x coordinate of separated beams after two stacked Wollaston prisms
y_i	Position parameter y for AVM
Y_n	Cartesian y coordinate of separated beams after a single Wollaston prism
$Y_{n\text{-}m}$	Cartesian y coordinate of separated beams after two stacked Wollaston prisms

Greek alphabet

α	Angle between $\vec{E}$ and $\vec{\mu}$
β	Angle of orientation of fringe pattern lines
β_{obj}	Orientation of interfering spots at back focal plane of the objective
γ	Half angle of cone
δ	Optimum rotation angle for data processing
ε	Decadic molar extinction coefficient

θ_n	Polarization light's orientation in angular coordinates of separated beams after a single Wollaston prism
$\theta_{n\text{-}m}$	Polarization light's orientation in angular coordinates of separated beams after two stacked Wollaston prisms
λ	Wavelength of light
λ_{fl}	Wavelength of fluorescence emission maximum
$\vec{\mu}$	Transition dipole moment
ν	Frequency of light
σ	Standard deviation
σ_{abs}	Optical cross-section per molecule for absorption
τ_{fl}	Fluorescence lifetime
υ	Phase velocity
ϕ	Angle between propagation direction of light and reference axis
ϕ_c	Critical angle
Φ_{fl}	Fluorescence quantum yield
φ	Phase of fluorescence modulation trace
Ψ	Electronic wave function
ω	Angular frequency
ω_1, ω_2	Angle of rotation of Wollaston containing mount

List of figures

List of tables

Danksagung

"The first step towards getting somewhere is to decide
that you are not going to stay where you are."

>Chauncey Depew<

Mein Dank gilt meinem Mentor, der mich über viele Jahre mit interessanten Forschungsprojekten versorgt hat, der mich meinen Drang zur Lehre hat ausüben lassen und der dafür gesorgt hat, dass wir Pokal nach Pokal nach Pokal abgeräumt haben.

Ich möchte mich bei Christof Maul bedanken, dafür, dass du eine besondere Vertrauensperson für mich bist, immer ein offenes Ohr hast und mich manchmal in der Spur gehalten hast. Ich hätte mir keine würdigere Person für die Zweitkorrektur vorstellen können, denn diese Arbeit gäbe es nicht ohne dich.

Ein herzliches Dankeschön geht an Prof. Dr. Engelhardt, der sich bereit erklärt hat den Prüfungskommissionsvorsitz zu übernehmen und sich die Zeit nimmt für diese Arbeit.

Ich möchte meinen Kollegen Mattias Grunwald und Nour Hafi danken, für all das, was ihr mir beigebracht habt.

Mein Dank gilt Andreas Albrecht, für deine mathematischen Beiträge zum AVM Algorithmus und dein aufmerksames Korrekturlesen.

Ich sage Danke an Dominik Pfennig für dein besonders kritisches Korrekturlesen, dessen Präzision kaum zu überbieten ist.

Meiner restlichen Arbeitsgruppe, Christoph Holleboom, Alexander Pieper, Daniel Gacek, spreche ich meinen Dank aus für viele tolle Momente, zu denen selten die Forschung gehörte, aber fast immer der Fußball! Es lebe E=PC^2.

Ich danke dem Fonds der chemischen Industrie für die jahrelange finanzielle Unterstützung.

Bürokratische Papierkämpfe kann immer noch Julia Lüttich am besten gewinnen. Vielen Dank für deine Unterstützung.

Mein Dank gilt der Abteilung Werkstatt, Thorsten Himstedt und Alexander Pablocki,

ohne deren Bauteile auf Maß einfach gar nichts ginge.

Ich möchte auch den Mensa- und Kuchentrupp nicht außen vor lassen, die den Arbeitsplatz zu einem angenehmen Umfeld haben werden lassen, mancher Tag war mehr Pause als Arbeit...

Ich danke Inga Schack für viele schöne Stunden im Praktikum, bei dem Frühstücken zur schönsten Nebensächlichkeit der Welt wird. Danke für das weltbeste Orangenmarmeladenrezept.

Ein warmes Dankeschön geht an alle weiteren Mitarbeitenden des Instituts für Physikalische und Theoretische Chemie, die täglich so Vieles leisten und wirklich ein neues Gebäude mehr als verdient haben.

Ich wäre nicht die, die ich bin, ohne Familie. Ich möchte euch alle knuddeln und Danke sagen für eure Unterstützung, für eure Kritik, für eure offene Tür, für euer Dasein für mich. Joop, Esther, Sanne, Mara. Ich hab euch lieb.

Auch auf meine Schwiegerfamilie kann ich mich immer verlassen. Reinhard, Ina, Steffen, Sabrina, Milena, Mika. Ich drücke euch ganz fest.

Meine Freunde bereichern mein Leben und ich möchte sie nicht missen. Schön, dass ich immer noch fragen kann: Wann wollen wir zusammen spielen?

Auch diese Danksagungsliste findet irgendwann ein Ende aber es gibt noch ein Dankeschön für die wichtigste Person von allen. Kristof, ich danke dir, dass wir diese Reise des Lebens gemeinsam bestreiten und dass du mir jeden Tag neue Energie gibst zu Strahlen. Du bist an meiner Seite nicht mehr wegzudenken. Bodos Liebeslied spricht mir aus der Seele: rákastan sínuá.

Lebenslauf

Persönliche Daten

Laura Shirin Jess, geb. van den Heuvel
Katharinenstr. 4
38106 Braunschweig
Email: l.jess@online.de
12 April 1988 in Heerhugowaard, Niederlande

Bildungsgang

seit 09/2012	**Promotionsstudium** Chemie
10/2010 - 08/2012	**Master of Science** (Note 1,0) Chemiestudium an der TU Braunschweig
10/2007 - 09/2010	**Bachelor of Science** (Note 1,2) Chemiestudium an der TU Braunschweig
06/2007	**Abitur** (Note 1,3) Theodor-Heuss-Gymnasium in Wolfenbüttel

Publikationen

A N. Hafi, M. Grunwald, **L. S. van den Heuvel**, T. Aspelmeier, J. H. Chen, M. Zagrebelsky, O. M. Schütte, C. Steinem, M. Korte, A. Munk, P. J. Walla. "Fluorescence nanoscopy by polarization modulation and polarization angle narrowing." *Nature Methods* **11** (5) 579-584 (**2014**).

B N. Hafi, M. Grunwald, **L. S. van den Heuvel**, T. Aspelmeier, J. H. Chen, M. Zagrebelsky, O. M. Schütte, C. Steinem, M. Korte, A. Munk, P. J. Walla. Reply to "Polarization modulation adds little additional information to superresolution fluorescence microscopy." *Nature Methods* **13** (1) 7-9 (**2016**).

Tagungsbeiträge

A **L. S. Jess**, D. Pfennig, M. Grunwald, A. Albrecht, N. Hafi, P. J. Walla. "Obtaining resolution enhanced fluorescence images and 3D orientation information of single molecules by polarization modulation." Vortrag PHYS-490, Single-molecule Fluorescence Imaging (#208). International Chemical Congress of Pacific Basin Societies [Pacifichem 2015], Honolulu, Hawaii, USA (2015).

Posterbeiträge

A **L. S. Jess**, D. Pfennig, M. Grunwald, A. Albrecht, N. Hafi, P. J. Walla. "Obtaining resolution enhanced fluorescence images and 3D orientation information of single molecules by polarization modulation." Poster 195, Single-molecule Fluorescence Imaging (#208). International Chemical Congress of Pacific Basin Societies [Pacifichem 2015], Honolulu, Hawaii, USA (2015).

B **L. S. Jess**, D. Pfennig, N. Hafi, M. Grunwald, P. J. Walla. "Super resolution by polarization demodulation (SPoD) and excitation polarization angle narrowing (ExPAN)." Poster 39. Pico Quant: 20th International workshop on single molecule spectroscopy and ultrasensitive analysis in the life sciences, Berlin (2014).

C **L. S. Jess**, N. Hafi, M. Grunwald, P. J. Walla. "Super resolution by polarization demodulation (SPoD) and excitation polarization angle narrowing (ExPAN)." Poster 75. Gordon Research Conference, Single molecule approaches to biology, Lucca (Barga), Italy (2014).

D **L. S. Jess**, P. J. Walla. "Nanoscopy by fluorescence polarization." Poster 18. 5. Braunschweiger Jungchemikertagung, Braunschweig (2014).

Preise/Auszeichnungen

07/2013 - 06/2015	**Chemiefonds-Stipendium** der Stiftung Stipendien-Fonds des Verbandes der Chemischen Industrie
07/2014	**Poster Competition Award** bei der Gordon Research Conference (Single Molecule Approaches to Biology)
01/2013	**Preis für einen herausragenden Master-Abschluss** vom Förderverein der Freunde des Instituts für Organische Chemie der TU Braunschweig
12/2012	**Braunschweiger Bürgerpreis** von der Stiftung Braunschweiger Bürgerpreis für herausragende studentische Leistungen und besonderes Engagement
10/2011 - 09/2012	**Leistungsstipendium** der TU Braunschweig
02/2011	**Preis für einen herausragenden Bachelor-Abschluss** vom Förderverein der Freunde des Instituts für Organische Chemie der TU Braunschweig
10/2010 - 09/2011	**Stipendium** für erbrachte Leistungen im Bachelorstudium der TU Braunschweig
10/2008 - 09/2009	**Stipendium** für erbrachte Leistungen im Bachelorstudium der TU Braunschweig
11/2008	**U23-Ehrenamtspreis** vom Niedersächsischen Fußballverband e.V. für Jugendtrainer und -betreuer